

Dynamic ice-structure interaction for jacket substructures

MSc Thesis Offshore & Dredging Engineering

J. Hoek

Delft University of Technology

Dynamic ice-structure interaction for jacket substructures

MSc Thesis Offshore & Dredging Engineering

To obtain the degree of Master of Science
in Offshore & Dredging Engineering at the
Delft University of Technology

Jeffrey Hoek

Student number: 4347196

Project duration: Feb. - Dec., 2021

Supervisors:	Dr. ir. H. Hendrikse	Delft University of Technology
	Ir. J. Speet	Siemens Gamesa Renewable Energy
	Ir. T.C. Hammer	Siemens Gamesa Renewable Energy

Graduation committee	Ir. A.C.M van der Stap	Delft University of Technology, Chairman
	Dr. ir. H. Hendrikse	Delft University of Technology



Cover photo: Wikingen wind farm located offshore Germany in the Baltic Sea
(<https://cdn.offshorewind.biz/wp-content/uploads/sites/2/2017/07/29114318/30-wikingen-turbines-in-place.jpg>)

Abstract

With a growing global demand of clean renewable energy, offshore wind activities will extend to more harsh environments, including sub-arctic areas like the Baltic Sea. Sea ice can occur here which needs to be taken into consideration in the design of substructures, i.e. jacket substructures, of offshore wind turbines. Several ice mitigating measures exist for jacket substructures, of which one is disregarding braces crossing the waterline. In this way, ice cannot induce loads to the relatively slender braces in the jacket. However, disregarding these braces has disadvantages in terms of structural integrity in comparison to a jacket including these braces.

In Part I of this thesis, two types of jackets, one without (Type 1) and one with (Type 2) waterline crossing braces, are implemented in a numerical model and subjected to ice loading in order to conclude whether the use of a Type 1 jacket design can be justified or whether a Type 2 jacket design is also suitable in sub-arctic areas.

Since over the past years the modelling techniques regarding ice-structure interaction have been updated and improved significantly, assessing the loads at the jacket braces can be done more accurately, allowing to give a more thorough conclusion on whether to use braces crossing the waterline on jackets in sub-arctic areas. As a result, a design including these braces could become feasible, whereas in the past it would be disregarded.

Two types of ice failure are considered in this research, being ice bending failure and ice crushing failure. First, a model is developed to quantify the ice actions occurring at a jacket substructure as function of the approach angle of the ice direction relative to the structure and as function of an introduced 'threshold angle'. It was found that ice failing in bending is equally significantly present as ice failing in crushing. Subsequently, numerical models are introduced that describe the failure behaviour of bending and crushing ice and the force that both ice failure types will induce to the structure. The structure is represented by a 5 [MW] offshore reference turbine supported by a jacket substructure. Using these models, dynamic simulations are performed in order to investigate the local susceptibility to ice-induced vibrations (IIV), as well as assessing the Ultimate Limit State (ULS) load at the braces. As a result, local brace IIV regimes could be recognised, however sustained frequency lock-in could not be observed. Furthermore, it was found that a Type 2 jacket could be suitable to use in sub-arctic areas considering the ULS load effects due to ice loading, but care should be taken for the ULS brace load, as that is of great importance for the design.

In Part II of this thesis, it is assessed whether coupled dynamic ice-structure interaction can be modelled using a dynamic substructuring modelling technique, also known as Craig-Bampton method, since it is industry practice to use such a method when jackets are involved. This method is based on a model order reduction of the full finite element model representing the structure, resulting in improved computational time and allowing assembly of multiple (reduced) substructures. The method is successfully implemented allowing to solve coupled ice-structure interaction problems and a framework to do so is provided. It is shown that excluding the loaded degrees of freedom (DoFs) in the jacket from the reduction leads to more accurate results and is considered convenient since few DoFs are loaded by ice, maintaining the effectiveness of the reduction method. As a result, IIV can be investigated using this reduction method, however challenges related to the accumulation of numerical accuracy errors arise with truncation of more higher frequency modes and require further development to be resolved.

Table of contents

Nomenclature	xi
Acknowledgements	xv
I Ice load applied to jacket substructures	1
1 Introduction	3
1-1 Baltic Sea	3
1-2 Substructure designs	4
1-3 Ice-structure interaction	7
1-4 Thesis objective	8
1-4-1 Dynamic substructuring	8
1-5 Thesis outline	9
1-5-1 Part I	9
1-5-2 Part II	9
2 Ice mechanics	11
2-1 Ice bending failure	12
2-1-1 Euler-Bernoulli beam theory to model bending ice	13
2-2 Ice crushing failure	16
2-2-1 Modelling crushing failure	16
2-2-2 Ice induced vibrations	19
3 Ice action on a jacket substructure	21
3-1 Threshold angle	21
3-2 Shielding	23
3-3 Jamming	24
3-4 Quantification of interaction	24
4 Forces induced by failing ice	29
4-1 Solve ice bending failure equations	29
4-2 Force induced by ice bending failure	34
4-3 Force induced by ice crushing failure	36
4-3-1 OC4 model	36
4-3-2 Modal analysis	37

5	Ice models applied to the structure	41
5-1	Global motion analyses	41
5-2	Local motion analyses - Ice bending failure	44
5-3	Local motion analyses - Ice crushing failure	47
5-3-1	Case studies.	51
5-4	Base shear	53
5-5	ULS brace load	54
II	Dynamic substructuring in modelling ice-structure interaction	57
6	Dynamic substructuring	59
6-1	The Craig-Bampton method.	60
6-2	Assembly of (super)elements.	62
6-2-1	Primal assembly	63
6-2-2	Dual assembly	64
6-3	Dynamic post-processing.	65
6-4	Constructing signed Boolean matrices B	66
6-5	Rayleigh damping	67
6-5-1	Tuning of Rayleigh damping parameters $\xi_{i,j}$	69
7	Ice models applied to the superelement representation of the structure	71
7-1	Non-reduced loaded DoFs	72
7-2	Coupled simulations in superelement domain	74
7-2-1	NRLD accuracy.	74
7-2-2	Numerical errors	75
8	Conclusions and recommendations	77
8-1	Conclusions	77
8-1-1	Part I	77
8-1-2	Part II	79
8-2	Recommendations.	80
8-2-1	Part I	80
8-2-2	Part II	82
A	Derivations	83
B	Finite difference approximation	87
C	Newmark method	95
	Bibliography	102

List of Figures

1-1	Baltic Sea area. X Wikinger X Baltic 2 X Kriegers Flak The purple areas are in the Concept/Early planning stage (4C Offshore, 2021)	4
1-2	Substructure designs and jacket terminology	5
1-3	Baltic 2 jacket, ice cones installed at legs	5
1-4	Wikinger jacket, x-braces omitted at sea level	6
1-5	Left: Wikinger (Type 1) design; Right: Traditional jacket design with x-braces through the water line (Type 2)	7
2-1	Failure modes for vertically sided structures (Hendrikse, 2017)	11
2-2	Failure modes for inclined surfaces	12
2-3	Failure behaviour for ice failing in bending	12
2-4	Schematic of the ice crushing model. The ice edge is modelled by N individual elements each with an offset to the structure drawn from a uniform distribution. Each element is described by Burgers model to capture the ice velocity dependent crushing behaviour	17
2-5	Load induced by a single ice element as function of the deformation of the element for different ice velocities	18
2-6	IIV regimes as function of ice velocity (Hendrikse, 2017). The top figures represent the structural motion, the bottom figures represent the ice load	19
3-1	Approach angle θ and ice-jacket interaction points	21
3-2	Ice failing in upward bending	22
3-3	Visualized influence of the threshold angle α . A lower threshold angle will lead to more crushing and less bending in the model	22
3-4	Shielding effect for multi-legged structures. Left: back legs fully sheltered by the wake of the front legs. Right: Back leg partially loaded due to wake formed by front leg (Hendrikse, 2017)	23
3-5	Number of elements per failure mode as function of approach angle θ	24
3-6	Quantification of failure modes as function of θ for $\alpha = \{58, 70, 82\}$	25

3-7	Interaction per element for different approach angles θ , $\alpha = 70$ [deg]. The purple line indicates the ice approach angle θ . A red element indicates that ice impacting this element is failing in crushing. Cyan elements indicate upward bending ice failure and yellow elements indicate downward bending ice failure. White elements are shielded by other elements	27
4-1	Deflection of the ice beam as function of time	32
4-2	Contribution of bending stress and normal stress to total tensile stress	32
4-3	Tensile stress as function of time	33
4-4	Deflection, total tensile stress and horizontal force for an ice beam with parameters listed in Table 4-1	34
4-5	Left: Induced horizontal force profiles for multiple ice velocities. Right: Breaking time for multiple ice velocities	36
4-6	Maximum and mean crushing force per meter structure width as function of ice velocity, $h = 0.4$ [m]	40
5-1	Amplitude FRF for symmetrical load (\rightarrow) around vertical axis - Type 1 vs Type 2	43
5-2	Amplitude FRF for unsymmetrical load (\rightarrow) around vertical axis - Type 1 vs Type 2	43
5-3	Left: Relation of ice thickness versus breaking length, Right: Failure frequency as function of ice velocity for $L = 10h$	44
5-4	Failure frequency as function of ice velocity for $L = 5h$	45
5-5	Structure responses due to periodic loads induced by ice failing in bending . .	46
5-6	AMD of legs vs braces	47
5-7	Regime comparison between legs and braces for $v_{ice} = 0.075$ [m/s]	48
5-8	The global motion at interaction level is obtained by computing the average displacement of the green nodes scaled to interaction level. This global motion is subtracted from the total displacement of the red node, obtaining the local motion indicated in blue. Here the ice velocity is 0.075 [m/s]	48
5-9	AMLD of local leg and brace displacement	49
5-10	Local displacement profile matches with global ice load profile on the brace .	49
5-11	Loaded brace velocity and displacement for $v_{ice} = \{0.025, 0.075, 0.145\}$ [m/s]. Although the brace is vibrating in one of its eigenmodes upon being dragged back through the ice (caused by the global motion being opposite to the ice direction) for all ice velocities, the vibration does not always correspond to local FLI	50

5-12	AMD of jacket with stiff legs and flexible braces	51
5-13	AMD of x-brace only for different structural properties	52
5-14	Worst case situation for $\theta = 15$ [deg]	53
5-15	Equivalent stick model	54
5-16	ULS brace load simplification	55
5-17	Brace utilisation as function of ice velocity	56
6-1	Jacket nodes divided in boundary nodes and internal nodes	60
6-2	Coupling two substructures	66
6-3	Rayleigh damping parameters a and b as function of modal damping ratio $\xi_{i,j}$	70
7-1	Force applied at internal node. The computed displacement of this loaded internal node is compared to the computed displacement of a non-loaded internal node	72
7-2	Jacket nodes divided in boundary nodes and internal nodes with NRLD approach	73
7-3	Force applied at internal node. Displacement computed with NRLD superelement. The displacement is now computed correctly	73
7-4	Comparison between modal, NRLD superelement and regular superelement solution for $v_{ice} = 0.01$ [m/s]	75
7-5	Comparison between modal domain and superelement domain solution	76

Nomenclature

Acronyms

AMD	Average maximum displacement
AMLD	Average maximum local displacement
CBR	Continuous brittle crushing
DoF	Degree of freedom
FEM	Finite Element Model
FLI	Frequency lock-in
FLS	Fatigue Limit State
FRF	Frequency response function
IC	Intermittent crushing
IEC	International Electrotechnical Commission
IIV	Ice-induced vibrations
ISO	International Organization for Standardization
MSL	Mean sea level
NRLD	Non-reduced loaded DoFs
OC4	Offshore Code Comparison Collaboration Continuation
PRD	Proportional Rayleigh Damping
RHS	Right-hand side
RNA	Rotor-Nacelle Assembly
SGRE	Siemens Gamesa Renewable Energy
TP	Transition piece
ULS	Ultimate Limit State

Symbols

α	Threshold angle	[deg]
α_s	Slope of the brace	[rad]
β	Slope coefficient	[-]
$\gamma_{R,b}$	Partial resistance factor for bending strength	[-]
δ_{crit}	Critical local deformation	[m]
ζ	Ratio between F_h and F_v exerted on the ice beam	[-]
$\boldsymbol{\eta}$	Vector of modal displacements	[-]
θ	Approach angle of ice direction relative to structure	[deg]
$\boldsymbol{\lambda}$	Vector of interface forces	[N]
μ	Ice-structure friction coefficient	[-]
ξ	Modal damping ratio	[-]
ρ	Ice density	[kg/m ³]
ρ_w	Seawater density	[kg/m ³]
σ_b	Internal bending stress	[MPa]
σ_f	Flexural stress capacity	[MPa]
σ_n	Normal stress	[MPa]
$\boldsymbol{\phi}_i$	Eigenvector	[-]
$\boldsymbol{\Phi}$	Eigenmatrix	[-]
$\boldsymbol{\Phi}$	Fixed interface vibration modes	[-]
$\boldsymbol{\Psi}_C$	Constraint modes	[-]
ω_i	Eigenfrequency	[rad/s]
Ω	Sinusoidal load frequency in FRF	[rad/s]
A	Beam cross-sectional area	[m ²]
\mathbf{B}	Signed Boolean matrix locating interface DoFs	[-]
b	Width of ice beam element	[m]
\mathbf{C}	Damping matrix	[Ns/m]
\mathbf{C}^*	Modal damping matrix	[Ns/m]
C_1	Parallel damper in Burgers model	[Ns/m]
C_2	Rear non-linear dashpot in Burgers model	[N ³ s/m]
C_d	Hydrodynamic drag coefficient	[-]
C_m	Hydrodynamic inertia coefficient	[-]
c	Material damping coefficient	[s]
D	Cylinder diameter	[m]
E	Yield strength	[Pa]
EI	Flexural stiffness	[Nm ²]
\mathbf{f}	Force vector	[N]
F_H	Horizontal force exerted on the ice beam	[N]
F_{ice}	Global ice load	[N]
F_v	Vertical force exerted on the ice beam, N	[N]
f_b	Representative bending strength	[Pa]
f_d	Hydrodynamic drag action per unit length	[N/m]
f_i	Hydrodynamic inertia action per unit length	[N/m]

g	Gravitational constant	[m/s ²]
h	Ice thickness	[m]
\mathbf{K}	Stiffness matrix	[N/m]
\mathbf{K}^*	Modal stiffness matrix	[N/m]
K_1	Parallel spring in Burgers model	[N/m]
K_2	Front non-linear spring in Burgers model	[N/m]
k	Winkler foundation stiffness	[N/m ²]
L	Beam length	[m]
L	Clear distance between jacket elements	[m]
\mathbf{L}	Boolean localization matrix	[-]
M	Internal moment	[Nm]
\mathbf{M}	Mass matrix	[kg]
\mathbf{M}^*	Modal mass matrix	[kg]
N	Axial compression force	[N]
N	Number of individual ice elements	[-]
n	Number of discretised beam elements	[-]
R_T	Tangential reaction force	[N/m]
R_N	Normal reaction force	[N/m]
r_{max}	Max offset of ice element with respect to structure	[m]
S	Salinity	[ppt]
t	Wall thickness	[m]
$ T $	Absolute average ice surface temperature	[°C]
Δt_0	Elapsed time since interaction	[s]
t_{frac}	Time of fracture	[s]
u	Beam deflection	[m]
u	Node displacement in ice element	[m]
u	Horizontal water particle velocity in the wave	[m/s]
\dot{u}	Horizontal water particle acceleration in the wave	[m/s ²]
u_s	Displacement of structure	[m]
V_b	Brine volume fraction	[ppt]
v_{ice}	Ice velocity	[m/s]
v_x	Horizontal (constant) ice velocity	[m/s]
w	Diameter of jacket element	[m]
Δx	Length of discretised beam element	[m]
Z_e	Elastic section modulus	[m ³]

Acknowledgements

Now that this thesis is finished, I would like to thank the people that contributed to it and supported me during the last ten months. First of all, many thanks go to my daily supervisors, Jeroen Speet and Tim Hammer. Jeroen, aka the jacket man, I learned a lot from you and really liked how you could bring your practical experience into the topic. Whenever I got stuck with something, you always provided another approach which eventually got me further. This also holds for Tim, aka the iceman. Thanks for all the help and interesting discussions. Your passion for ice is contagious and I am sure we will continue discussing ice regimes occasionally at the Friday afternoon drinks.

Next, I would like to thank my supervisor from the TU Delft, Hayo Hendrikse. Your interesting questions and comments really raised the level of this thesis. I always got helpful feedback from you and if I needed an additional meeting to get some things straight it was never a problem, which I appreciate a lot. I am sure we will continue discussing ice-structure interaction in the future.

I would also like to thank Andre van der Stap, my graduation chairman, for challenging me to really get my conclusions solid and to look at the problem from a helicopter view instead of too much into the details. I will keep this approach with me for the rest of my career as an engineer.

Furthermore, thanks to all colleagues and fellow students at SGRE for the relaxed working environment and for the small talks at the coffee machine, which offered me a different perspective to the problems I had. Col, thanks for providing the smooth start during these challenging times and I am glad we will continue being colleagues.

Last but definitely not least, thanks to my parents, brothers and family in law for the continuous support during my studies. Tim en Thomas, thanks for the discussions accompanied by a beer or two, which provided me new ideas to include in the research. Sammy, my lovely girlfriend, thank you for your endless love and support and for being always there for me.

*Jeffrey Hoek
The Hague, December 2021*

Part I

Ice load applied to jacket substructures

1

Introduction

Climate change is one of the biggest challenges the world is facing today. In an effort to combat climate change, an international accord also known as Paris Agreement was signed (United Nations, 2015). In addition to the Paris Agreement, the European Union has set up an initiative, the Green Deal, to be fully climate neutral by 2050. The target for 2030 is to reduce the emission of greenhouse gasses by 55% in comparison to 1990 (European Commission, 2019). Because the costs of offshore wind have significantly dropped over recent years (Wind Europe, 2021a), the offshore wind industry is one of the most promising and one of the fastest growing fields of renewable energy.

1-1 Baltic Sea

The research in this thesis will consider the area of the Baltic Sea (Fig.1-1). Offshore wind activities are already carried out in this area (Wikinger, Baltic 2) and windparks are being developed and under construction (Kriegers Flak). Currently the Baltic Sea has 2 [GW] of installed capacity, but could host up to 93 [GW] by 2050 (Wind Europe, 2021b). The purple areas in Fig.1-1 indicate the possible sites in the near future. One major contributor in the coming years will be Poland. In 2019, Poland was the only EU member not to commit to the targets of the Green Deal (European Council, 2019). However, pressure from other EU members, rising prices of carbon and the increased awareness of climate change has driven the government of Poland to reconsider their decision (Żuk and Żuk, 2021). Poland is now planning to install 8 to 11 [GW] of offshore wind power by 2040 (Reuters, 2021). The Polish exclusive economic zone extends in the Baltic Sea. The objective to install a very significant amount of offshore wind turbines in the Baltic Sea makes it a relevant location for research.

However, the Baltic Sea is located in a sub-arctic region meaning that sea ice can occur. The loads induced by this ice on the supporting structure of wind turbines should be taken into consideration in the design of these structures (ISO 19906, 2019).

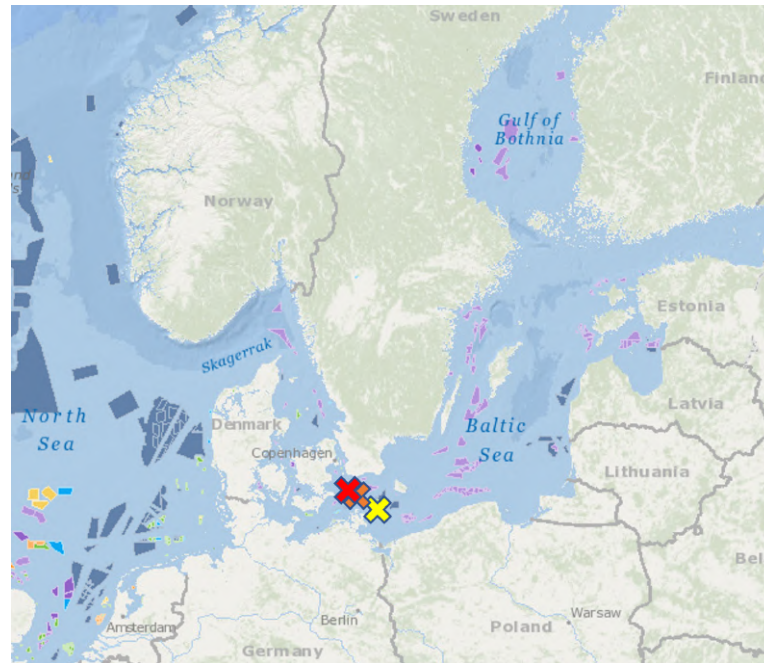


Figure 1-1: Baltic Sea area. X Wikinger X Baltic 2 X Kriegers Flak
The purple areas are in the Concept/Early planning stage (4C Offshore, 2021)

1-2 Substructure designs

Various types of substructure designs exist for offshore wind turbines, the most common being: monopiles, jackets, gravity base structures, tripods and floating structures. Monopiles are by far the most used type of foundation with a market share of 81.2% (WindEurope, 2021c), but for challenging water depths and/or soil conditions, jackets (Fig.1-2a) can be preferred over monopiles (9.9% market share). This is because in comparison to monopile foundations, less material is needed to obtain the desired structural properties and jacket foundations could therefore be more economically feasible (Voormeeren et al., 2014). A jacket typically consists of legs, braces and a transition piece (TP) (Fig.1-2b). In this case the braces are configured as x-braces.

Currently the industry is mitigating ice loads on jackets by various methods. In Fig.1-3 a jacket from the Baltic 2 wind farm in the Baltic Sea is shown. Note that conical tubes of steel named ice cones are installed at water level. One leg is not equipped with a cone in order to preserve a boat landing. These ice cones are pushing the ice sheet out-of-plane, i.e. upwards

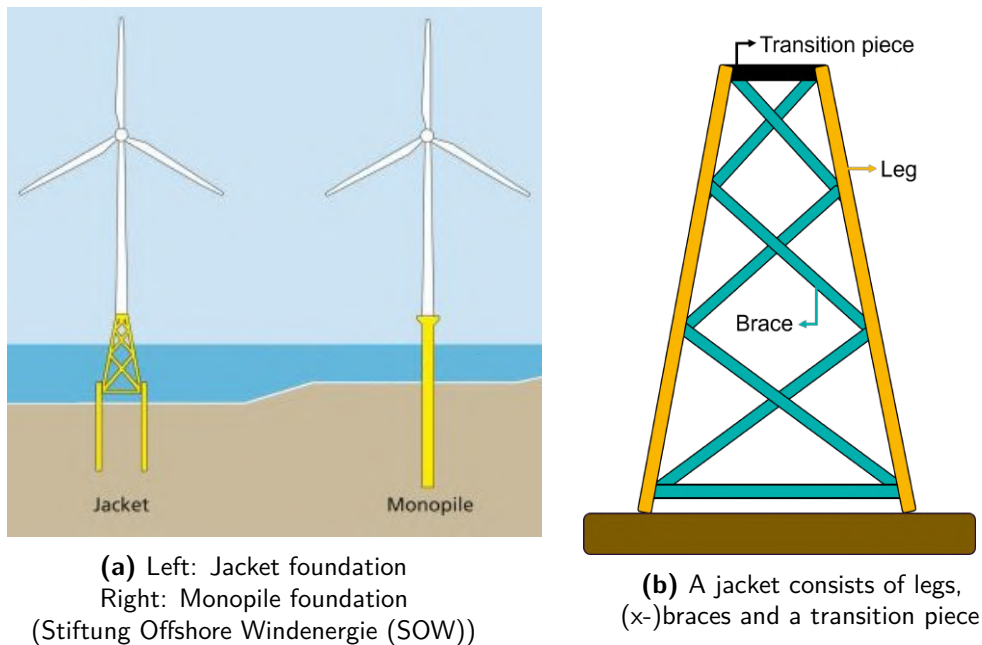


Figure 1-2: Substructure designs and jacket terminology

or downwards, causing the ice to fail in bending. Ice bending failure is described in Section 2-1. The effect of bending the ice out-of-plane is that it reduces the ice load on the structure in comparison to a situation without an ice cone (Danys and Bercha, 1976). On top of this, it reduces the susceptibility of ice-induced vibrations (IIV) (Brown and Määttänen, 2009). However, these ice cones are expensive to fabricate and require special attention at assembly. Also, the cones increase the diameter at water level, resulting in significantly higher wave loads when no ice is present (Tang et al., 2020).



Figure 1-3: Baltic 2 jacket, ice cones installed at legs

Another method to mitigate ice loading is seen at the Wiking wind farm (Fig.1-4) located north of Germany in the Baltic Sea. To reduce the effect of ice loading no braces are crossing the waterline. This is to prevent the ice from crushing into the braces. Ice crushing failure is described in detail in Section 2-2.



Figure 1-4: Wikinger jacket, x-braces omitted at sea level

When one compares the Wikinger jacket to a 'regular' jacket as illustrated in Fig.1-5, one notices that the difference between both types of jackets is whether the x-braces are crossing the waterline or not. A regular jacket in this case is one that is commonly used in areas that are not affected by ice. For clarity, from now on the Wikinger jacket will be called 'Type 1' and the regular jacket will be called 'Type 2'. There are several reasons to prefer Type 2 over Type 1. Firstly, the fabrication of jackets in this way is industry practice. This is an advantage as foundation designers can use their conventional methods to design and construct the jacket. Secondly, in case of failure of one brace or leg, the redundancy of the Type 2 jacket is higher (Sambu Potty and Ahmad Sohaimi, 2013). It is less likely to collapse in case of failure of one leg caused by a vessel impact for example. Furthermore, the structural integrity is better in wave loading. The in-plane loads caused by wave loading will be covered by axial forces in the members instead of significant internal shear forces and moments in the legs of the Type 1 jacket. Also, because of this integrity, the legs of the Type 1 jacket often need to be thicker which could be more expensive. Another important point is that a failure in the pitch or yaw system of the turbine can cause the turbine to vibrate in the torsional direction because of asymmetric loading. This causes large oscillating moments around the vertical axis in the top part of the jacket. A Type 2 jacket naturally has a larger resistance against these torsional moments because of the aforementioned points.

Following the statements of the previous section, the main point of this thesis is to compare these jacket designs with each other in terms of Ultimate Limit State (ULS) loading. On top of that, the internal dynamics will be investigated.

Therefore, the first research question is:

1. *Can the use of the Type 1 design be justified or is a Type 2 jacket also suitable in sub-arctic areas?*

Part I of this thesis will focus on answering this research question. To answer this question finite element models (FEM) will be made of the Type 1 and Type 2 jacket. Subsequently, both models will be subjected to different types of ice-loading. Analysing the static and dynamic loading will justify or debunk the use of the Type 1 jacket.

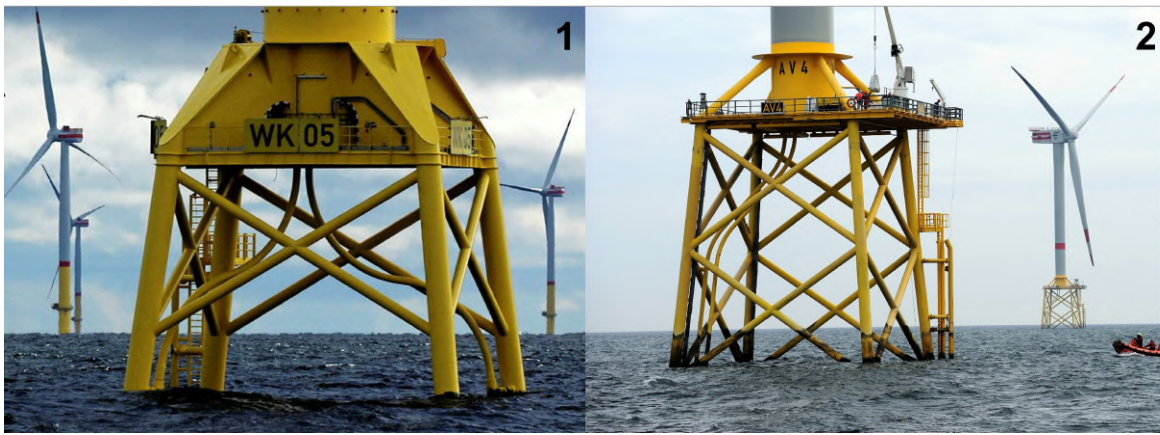


Figure 1-5: Left: Wikinger (Type 1) design; Right: Traditional jacket design with x-braces through the water line (Type 2)

1-3 Ice-structure interaction

Ice failing in bending upon interacting with the inclined parts of the structure induces loading to the structure. It is important to assess these loads for the relatively slender braces in the structure. This will be further discussed in Section 2-1 and 4-2. The crushing of ice against a vertical structure can cause the structure to respond in three different ways (Hendrikse, 2017), being: Intermittent crushing (IC), Frequency lock-in (FLI) and Continuous brittle crushing (CBR). These different responses will be extensively discussed in Section 2-2. The IC regime can govern both Ultimate Limit State (ULS) and Fatigue Limit State (FLS) loads and the FLI regime can have a significant contribution to fatigue (Hendrikse and Koot, 2019). There are several examples of previous work on this topic and research is still ongoing. Many of these studies consider monopiles, fewer are concerning jackets. For jackets often the OC4 reference model is used (Vorpahl et al., 2013). However, in these studies the global behaviour of the structure is considered instead of the local behaviour. On top of that, the ice loading is often applied only to the legs of the jacket disregarding the loading subjected to the braces.

1-4 Thesis objective

Since over the past years the modelling techniques regarding ice-structure interaction have been updated and improved significantly, assessing the loads at the jacket braces can be done more accurately, allowing to give a more thorough conclusion on whether to use braces crossing the waterline on jackets in sub-arctic areas. As a result, a design including these braces could become feasible, whereas in the past it would be disregarded.

The novelty of this research will be the comparison of the susceptibility to IIV of different jacket types (Type 1 and 2), including the effect of braces. Instead of only analysing the global response of the structure, the response of the individual braces will now be investigated. When the responses are known it can be assessed if these braces are susceptible to the regimes described in Section 1-3 and if so, which regime is governing. Additionally, the loads will be assessed at these braces to draw conclusions in terms of ULS loading.

Two methods will be considered in this thesis. One is the full model approach. A full FEM will return the most extensive results so in order to have this, the aforementioned OC4 jacket model will be built in `MATLAB` and a FEM will be constructed. Coupling this FEM to the ice crushing and bending model (Chapter 2) and adding a tower and Rotor-Nacelle Assembly (RNA) will complete the model. The RNA will be modelled as a lumped mass. This full FEM will be subjected to different types of ice loading and the response will be analysed. The second method is discussed in the next section.

1-4-1 Dynamic substructuring

In addition to the full model approach, there is a second modelling option called the 'dynamic substructuring method'. This method is based on a model order reduction of the jacket model (Van der Valk, 2014a). One of the effects of the reduction is that the computational effort per simulation is reduced. Typically, a wind turbine manufacturer runs up to fifty thousand simulations to assess the structural integrity of the system. Therefore, due to the reduced simulation time, this modelling option is preferred. Siemens Gamesa Renewable Energy (SGRE) uses this dynamic substructuring method to model the complete assembly of foundation, tower and RNA. The principle of the method will be discussed extensively in Chapter 6.

Apart from improved simulation time, there are more reasons to use this method. Firstly, the full system can be analysed without evaluating a full FEM of the combined system. Secondly, it allows a foundation designer to model the structure in their desired software, while the turbine manufacturer can include the reduced matrices representing the foundation in their load calculations, using their own software. This removes the need to remodel the complete system and lowers the risk of errors. Furthermore, because there is typically a clear division between foundation designer and turbine manufacturer, this method protects intellectual property and

separates responsibility. A downside of this method is that it simplifies the problem and important information regarding the dynamic behaviour of the jacket substructure could be lost. It is important to know in which situations the dynamic substructuring method is applicable to analyse the structure. Therefore, a second research question arises:

2. *Can coupled dynamic ice-structure interaction be modelled by a dynamic substructuring modelling technique?*

Part II of this thesis will be about the research regarding this second research question.

1-5 Thesis outline

This thesis is divided in two parts. Each part is devoted to answering one research question.

1-5-1 Part I

The first part is about ice load applied to jacket substructures. In Chapter 1 it has been outlined what geographical area is considered, which substructure designs exist and what the challenges are regarding ice loading for these substructures. In Chapter 2 it will be discussed which ice failure types will be considered in this thesis and what models exist describing these ice failure types. Thereafter, in Chapter 3, it will be quantified how much of these ice failure types will occur at a jacket substructure, to have a good overview of the ice actions at a jacket. Next, in Chapter 4, the models introduced in Chapter 2 will be numerically solved and implemented to gain understanding of which forces will be induced to the structure by both ice failure types. In Chapter 5 these forces are applied to the structure and as a result conclusions can be drawn answering the first research question.

1-5-2 Part II

The second part of this thesis will discuss the dynamic substructuring modelling technique. In Chapter 6 the method is explained. It will give a thorough overview of the procedure, substructure assembly, damping and post-processing involved using this method. In Chapter 7 it is discussed what is important to consider when modelling coupled ice-structure interaction with this modelling technique and it will be verified whether it is possible to use this method in coupled ice-structure problems, answering the second research question.

Finally, in Chapter 8 a conclusion is provided as well as a discussion on recommendations for future research.

2

Ice mechanics

Level ice, i.e. floating ice with a flat surface, may fail in multiple ways to the structure. In this research it is assumed that upon interacting with the structure, the ice can only fail in *bending* and *crushing*.

On *vertically sided* parts of a structure, ice can fail in creep, crushing, and buckling. Creep is the (ductile) failure of ice for very low indentation velocities. For higher indentation velocities, the ice fails in crushing. Buckling failure of the ice as described by Hendrikse and Metrikine (2016) is not taken into account. On top of these splitting can also occur, referring to an initiated crack at the ice-structure interaction point propagating to a free edge. This mainly occurs for small ice floes. In this research it is assumed that the ice floe is sufficient in size that splitting does not occur. The failure modes for vertically sided structures are shown in Fig.2-1.

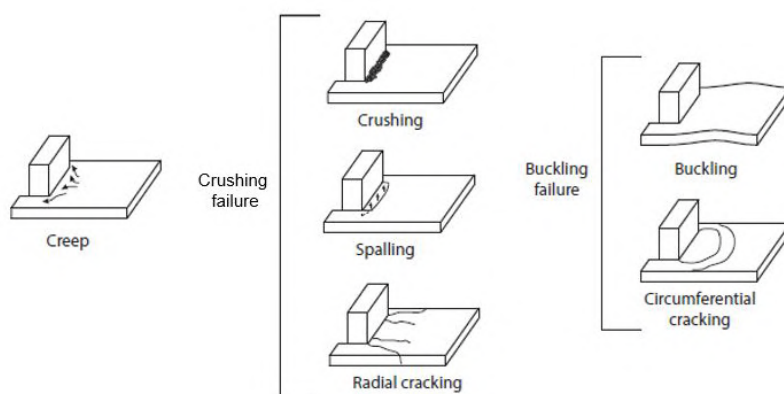


Figure 2-1: Failure modes for vertically sided structures (Hendrikse, 2017)

For *inclined* surfaces, the ice can fail in upward or downward bending, depending on the direction of the slope (Fig.2-2).

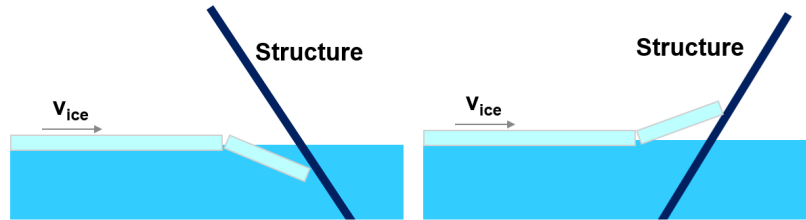


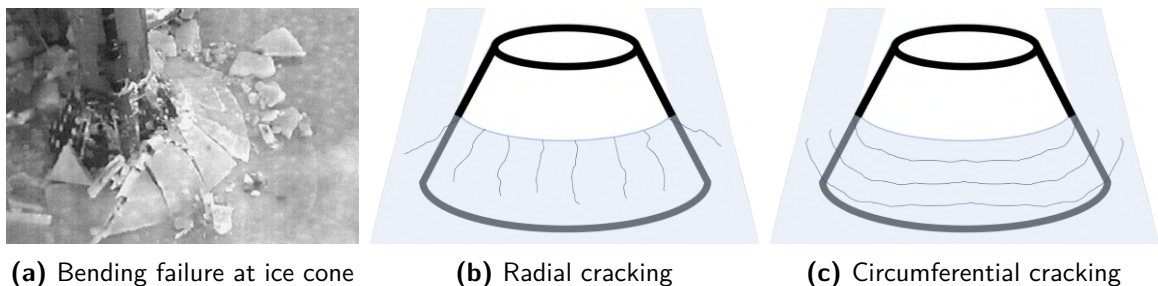
Figure 2-2: Failure modes for inclined surfaces

In this chapter ice bending failure and ice crushing failure will be described. Also, for both failure modes models will be introduced that can be used to apply forces to the structure.

2-1 Ice bending failure

When an ice sheet runs up or down on a sloping surface, for example the braces in a jacket, ice bending failure can occur. Upon bending the internal stress in the ice sheet will increase because of the out-of-plane bending of the ice. When this stress exceeds the stress capacity of the ice, the ice will fail in bending. If the velocity of the ice, the angle of the slope and the mechanical properties of the ice change, the time it takes until breaking, the length of the broken ice part and the force induced to the structure will differ. An ice bending model can be constructed to investigate this behaviour.

Ice bending failure is what typically occurs at ice cones (Section 1-2) and is illustrated in Fig.2-3a (Yue and Bi, 2000). It can be seen that the ice fails in the radial and in the circumferential direction, shown in Fig.2-3b and 2-3c. Because of the curvature of the cone, radial cracks will initiate from the ice-structure interaction point. Since the cone is also inclined, circumferential cracks will develop.



(a) Bending failure at ice cone

(b) Radial cracking

(c) Circumferential cracking

Figure 2-3: Failure behaviour for ice failing in bending

To investigate the behaviour of the bending ice, first it needs to be defined on what theory the ice model will be built. As is clear from Fig.2-3, the ice could be best described by plate theory. In this way the model will be two dimensional, allowing to account for the curvature of the cone and thereby include the circumferential and radial cracking behaviour. However, since the main interest lies in the induced forces to the structure and not particularly in how the ice cracks, a more simplified one dimensional model could be sufficient.

The jacket structure in this research will be based on the OC4 reference jacket. The braces in the OC4 model do have a diameter of 0.8 [m], but since they are inclined, the waterline-crossing width of the created ellipse is close to 1 [m]. This is a much smaller width in comparison to an ice cone, reducing the effect of circumferential cracks. The effect of radial cracks will also be reduced because of the width between these cracks. Less radial cracks can be formed on a smaller diameter slope. The ice could therefore also be approximated by a beam model, expressed in terms of [N/m]. It will be less accurate than using plate theory, but it gives good insight in the physics of ice bending failure.

2-1-1 Euler-Bernoulli beam theory to model bending ice

Based on the research by Wille et al. (2011), where bending ice is also approximated by a beam, a model will be constructed that will describe *downward* bending ice. A very long beam of ice ($L = 1000$ [m]) of 1 [m] width is assumed. Since the beam is very long, it can be assumed that the plane cross-sections initially perpendicular to the axis of the beam remain plane and perpendicular to the neutral axis during bending. This makes it relevant to use the Euler-Bernoulli beam theory instead of more elaborate beam theories like Timoshenko's (Metrikine, 2006). The general equation of motion of an Euler-Bernoulli beam is:

$$\rho A \frac{\delta^2 u_z}{\delta t^2} + EI \frac{\delta^4 u_z}{\delta x^4} = q(x, t) \quad (2.1)$$

The beam has a mass density ρ [kg/m³], a cross-sectional area A [m²] and a flexural stiffness EI [Nm²] (Spijkers et al., 2005). The unit of each term is [N/m]. The right-hand side (RHS) represents the loading on the beam. For the remainder of the chapter, the external load is assumed to be zero, i.e. no wave load is acting on the ice:

$$\rho A \frac{\delta^2 u_z}{\delta t^2} + EI \frac{\delta^4 u_z}{\delta x^4} = 0 \quad (2.2)$$

Since the ice beam is floating on water, the buoyancy is modelled by distributed springs, known as a Winkler foundation. The stiffness k can be computed by $k = \rho_w g b$ [N/m²]. Where ρ_w [kg/m³] is the density of the water, g [m/s²] is the gravitational constant and b [m] is the width of the beam:

$$\rho A \frac{\delta^2 u_z}{\delta t^2} + EI \frac{\delta^4 u_z}{\delta x^4} + k u_z = 0 \quad (2.3)$$

The beam is floating to the right side in the direction of the structure (Fig.2-2). When the beam touches the structure, an axial compression force N [N] is applied to the beam. In bending, this axial force yields an additional shear force along the beam. Adding this shear force to the moment equilibrium yields the equation of motion:

$$\rho A \frac{\delta^2 u_z}{\delta t^2} + EI \frac{\delta^4 u_z}{\delta x^4} + k u_z + N \frac{\delta^2 u_z}{\delta x^2} = 0 \quad (2.4)$$

The beam is moving with respect to the global coordinate system with velocity v_x [m/s]. To account for this velocity a 'convective term' is added to the equation of motion. Furthermore, it is assumed that the horizontal velocity of the ice beam remains constant. As mentioned by Hendrikse and Nord (2019), what is interesting for jackets opposed to monopiles is that the jacket members are more slender, resulting in a lower load acting on the ice, resulting in slowing down the ice less rapidly. This substantiates the assumption of constant horizontal velocity. The derivation of the convective term can be found in Appendix A.

$$\rho A \left(\frac{\delta^2 u_z}{\delta t^2} + 2v_x \frac{\delta^2 u_z}{\delta x \delta t} + v_x^2 \frac{\delta^2 u_z}{\delta x^2} \right) + EI \frac{\delta^4 u_z}{\delta x^4} + k u_z + N \frac{\delta^2 u_z}{\delta x^2} = 0 \quad (2.5)$$

To complete the equation of motion, a damping term has to be added. Unfortunately, it is unknown how damping is incorporated in the interaction between ice and structure. To be able to solve the problem, the damping is chosen proportional to the axial compression. The derivation can be found in Appendix A. This yields the final equation of motion as:

$$\rho A \left(\underbrace{\frac{\delta^2 u_z}{\delta t^2}}_{\text{mass}} + \underbrace{2v_x \frac{\delta^2 u_z}{\delta x \delta t} + v_x^2 \frac{\delta^2 u_z}{\delta x^2}}_{\text{convective}} \right) + \underbrace{EI \frac{\delta^4 u_z}{\delta x^4}}_{\text{beam stiffness}} + \underbrace{k u_z}_{\text{buoyancy}} + \underbrace{N \frac{\delta^2 u_z}{\delta x^2}}_{\text{axial compression}} - \underbrace{cN \left(\frac{\delta^3 u_z}{\delta x^2 \delta t} + v_x \frac{\delta^3 u_z}{\delta x^3} \right)}_{\text{damping}} = 0 \quad (2.6)$$

Where c [s] is the material damping coefficient and N [N] is the axial force, expressed as (Wille et al., 2011):

$$N = \frac{-EI\zeta \frac{\delta^3 u_z}{\delta x^3}}{1 + \zeta \frac{\delta u_z}{\delta x} - c\zeta \left(\frac{\delta^2 u_z}{\delta x \delta t} + v_x \frac{\delta^2 u_z}{\delta x^2} \right)} \quad (2.7)$$

ζ [-] is the ratio between the horizontal and the vertical force exerted on the beam upon interaction with the structure, expressed as:

$$\zeta = \frac{F_H}{F_V} = \frac{\sin \alpha_s + \mu \cos \alpha_s}{-\cos \alpha_s + \mu \sin \alpha_s} \quad (2.8)$$

The derivation of ζ can be found in Appendix A. Here α_s [rad] is the slope of the structure and μ [-] is the ice-structure friction coefficient.

Eq.2.6 is a fourth order differential equation in space. To solve the system, four boundary conditions are required, two at each side of the beam. At the left (away from the structure) it is assumed that the beam is clamped (but moving in the horizontal direction with velocity v_x). Assuming a very long beam ($L = 1000$ [m]), the deflection and rotation will be negligible far away from the ice-structure interaction point. This yields the first two boundary conditions:

$$u_z(0, t) = 0, \quad \frac{\delta u_z}{\delta x}(0, t) = 0 \quad (2.9)$$

On the right end of the beam, the boundary conditions depend on the interaction with the structure. For the bending failure mode, the structure is assumed to be fixed and immovable. In Section 2-2, where crushing is discussed, the structure is assumed to be compliant. The axial force at the right end of the beam (N) is used to define the boundary condition. For clarity it is called F_H , being the horizontal force acting between the structure and the beam of ice. The bending moment and the deflection at the right end of the beam are used as the remaining two boundary conditions, being:

$$\begin{aligned} -EI \frac{\delta^2 u_z}{\delta x^2}(L, t) &= -\frac{h}{2} F_H \\ u_z(L, t) &= v_x \Delta t_0 \sin(\alpha_s), \quad \Delta t_0 = t - t_0 \end{aligned} \quad (2.10)$$

Where h [m] is the ice thickness, v_x [m/s] is the constant horizontal velocity of the beam and Δt_0 [s] is the elapsed time since interaction.

Eq.2.6 is second order in time, therefore two initial conditions are required. It is assumed that the beam is initially at rest, giving the two conditions:

$$u_z(x, 0) = \frac{\delta u_z}{\delta t}(x, 0) = 0 \quad (2.11)$$

Now this system of equations can be solved using the 'Finite Difference method', explained in Appendix B, using the explicit Runge-Kutta (4,5) method (ODE45) implemented in MATLAB. This is further discussed in Chapter 4, where it will also be discussed how the forces induced to the structure can be obtained from the solution of this system of equations.

2-2 Ice crushing failure

Now that the bending failure mode of the ice is described, the following step is to describe the ice crushing failure mode. The difficulty of modelling ice crushing failure is that the ice force induced to the structure is a function of the structural displacement and vice versa, requiring a coupled model. This behaviour is and has been investigated extensively for monopile structures (Willems, 2016; Hendrikse, 2017; Hendrikse et al., 2018; Hendrikse and Nord, 2019; Willems and Hendrikse, 2019), as well as some multi-leg structures (Timco et al., 1992; Yue and Bi, 2000; Marsman, 2018; Hendrikse and Koot, 2019; Chuang et al., 2020). The most recent iteration of the phenomenological model developed by Hendrikse and Metrikine (2016) as described by Hendrikse and Nord (2019) is used in this thesis.

2-2-1 Modelling crushing failure

In the ISO and IEC code (ISO 19906, 2019; IEC 61400-3-1, 2019a) guidance is given on how to account for ice loading. However, this guidance is based on predefined ice loads instead of coupled ice-structure loads. This results in such conservative structural responses that designing for IIV becomes challenging (Hendrikse and Nord, 2019). In order to account for the coupling between ice and structure, a phenomenological ice model has been developed by Hendrikse and Metrikine (2016). The latest iteration of that model described by Hendrikse and Nord (2019) will be discussed here. The numerical implementation of this model will be discussed in Section 4-3.

The model describes the load induced by ice crushing onto the structure. To capture the contact area variation and the statistical nature of the crushing process, the ice approaching the structure is divided into N [-] elements (Fig.2-4). Each element is positioned with a uniformly distributed offset to the structure.

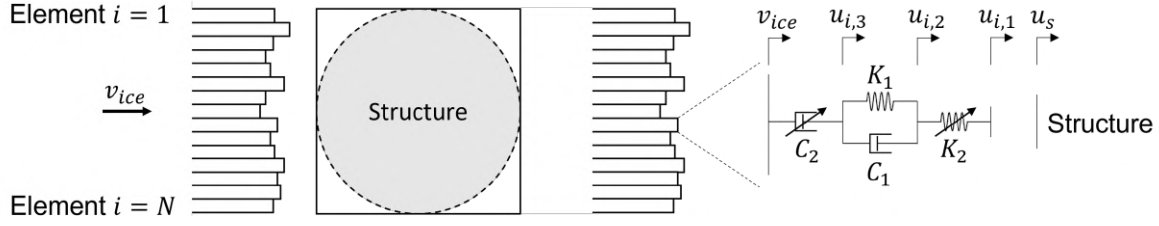


Figure 2-4: Schematic of the ice crushing model. The ice edge is modelled by N individual elements each with an offset to the structure drawn from a uniform distribution. Each element is described by Burgers model to capture the ice velocity dependent crushing behaviour

Upon contact, the local deformation and failure behaviour of the ice is described by a system of (non-)linear dashpots and springs, also known as Burgers rheological model. The rear non-linear dashpot, C_2 [$\text{N}^3 \text{m}^{-1} \text{s}$], describes the behaviour of the ice in the creep range, for very low ice velocities. The deformation of this part is a function of the stress cubed, also known as 'power law creep' (Weertman, 1983).

The parallel linear spring-dashpot combination consisting of spring K_1 [N/m] and damper C_1 [Ns/m] accounts for the delayed-elastic deformation of the ice. This is to describe the behaviour of the ice for ice velocities between creep and high velocity crushing.

The front non-linear spring K_2 [N/m] accounts for the local elastic deformation of the ice and failure when it reaches a predefined critical local deformation, δ_{crit} [m].

$$u_{i,2} - u_{i,1} = \delta_{crit} \quad (2.12)$$

When the indentation of the spring is equal to the maximum admissible value δ_{crit} , the ice element breaks and is removed from the interaction point. The element is placed back at a distance drawn from a uniform distribution U . The offset can therefore be described by:

$$u_{i,1} = u_{i,2} = u_{i,3} = u_s(t_{frac}) - U(0, r_{max}) \quad (2.13)$$

Where t_{frac} [s] is the time of fracture and r_{max} [m] is the maximum offset of the element with respect to the structure. Spring K_2 describes the behaviour of the ice for larger ice velocities.

The combined system of these three parts results in an ice velocity dependent deformation and failure behaviour of each ice element, shown in Fig.2-5. Here the ice load induced to the structure for an individual ice element can be seen as function of the deformation of the element. At high ice velocities, the deformation grows linearly until it reaches the predefined critical load deformation δ_{crit} . Upon reaching this point, brittle failure will occur and the element is removed and set back according to Eq.2.13. At low ice velocities, brittle failure will never occur because of the deformations in the rear dashpot element C_2 . For intermediate

ice velocities, local brittle failure will eventually occur when the element deformation exceeds δ_{crit} .

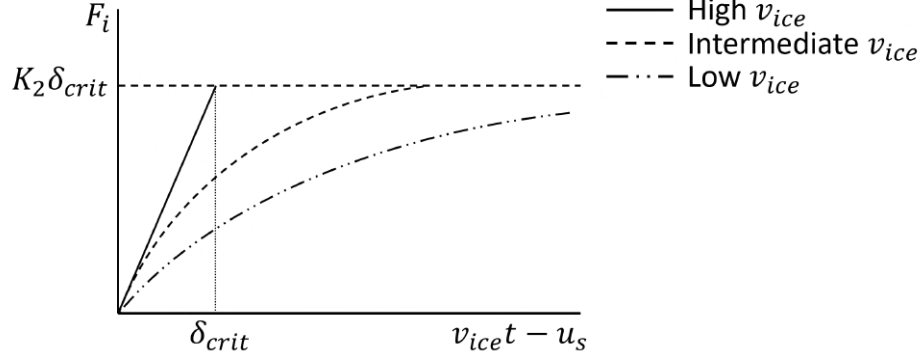


Figure 2-5: Load induced by a single ice element as function of the deformation of the element for different ice velocities

Equations of motion

The equations of motion for a single ice element are given as:

$$\begin{aligned}
 u_{i,1} &= \begin{cases} u_{i,2}, & u_{i,1} < u_s \text{ (no contact)} \\ u_s, & u_{i,1} \geq u_s \text{ (contact)} \end{cases} \\
 \dot{u}_{i,2} &= \frac{K_2}{C_1}(u_{i,1} - u_{i,2}) + \frac{K_1}{C_1}(u_{i,3} - u_{i,2}) + v_{ice} - \frac{1}{C_2} (K_2(u_{i,2} - u_{i,1}))^3 \\
 \dot{u}_{i,3} &= v_{ice} - \frac{1}{C_2} (K_2(u_{i,2} - u_{i,1}))^3
 \end{aligned} \tag{2.14}$$

Where $u_{i,1}$, $u_{i,2}$ and $u_{i,3}$ [m] are the displacements of the nodes in a single element. A single overdot represents the velocity of that node [m/s]. u_s [m] is the displacement of the structure. The total force induced to the structure by the ice, also referred to as global ice load, is the sum of the forces in springs K_2 for all ice elements N :

$$F_{ice} = \sum_{i=1}^N K_2(u_{i,2} - u_{i,1}) \tag{2.15}$$

Here it is assumed that each element i acts at a single point on the structure.

Ice parameters

The values for $K_1, K_2, C_1, C_2, N, \delta_{crit}$ and r_{max} have to be obtained from measurement data. These measurements are performed on a rigid structure, after which simulations can be performed on flexible structures with similar ice conditions (Hendrikse and Nord, 2019). In this thesis the values are based on data from the STRICE project, performed in the Baltic Sea (Cordis, 2021).

In this thesis the ice properties that will be varied are the ice velocity (v_{ice}) and the ice thickness (h). In the research by Gravesen et al. (2009) it was found that the 1/50 year ice thickness for the Southern Baltic sea is 0.4 [m]. For the ice velocity, reference is made to the research by Leppäranta (1981) who constructed an ice drift model for the Baltic Sea. A maximum ice velocity of 0.4 [m/s] was found and will also be used as maximum ice velocity in this thesis.

2-2-2 Ice induced vibrations

As can be deduced from the equations of motion, the force induced to the structure by crushing ice depends on the ice velocity relative to the structure. Hence, a coupled system is formed. For different relative velocities between ice and structure, the build-up of global ice load is different. As a result, different crushing failure regimes can be distinguished over a range of ice velocities. The regimes are illustrated in Fig.2-6.

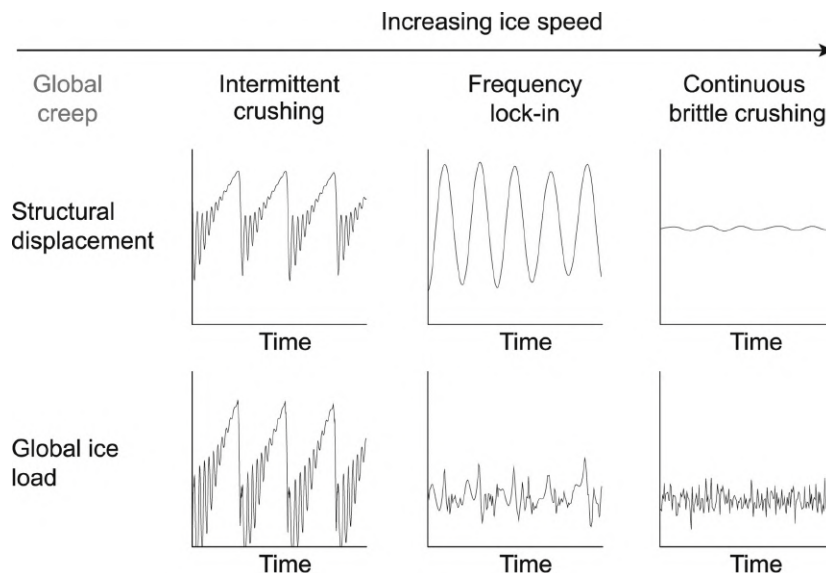


Figure 2-6: IIV regimes as function of ice velocity (Hendrikse, 2017). The top figures represent the structural motion, the bottom figures represent the ice load

Intermittent crushing

For low ice velocities intermittent crushing can develop. During loading the structure deflects slowly in the direction of the ice motion. During this phase the relative velocity decreases, resulting in ductile failure of the ice, gradually increasing the contact area between ice and structure. Energy is stored in the structure until the point of maximum deflection is reached. Now the ice starts to fail, resulting in a velocity of the structure opposite to the ice motion. During this phase the ice fails in a brittle manner, which results in a drop of the global ice load. The relative velocity is high preventing the contact area to increase. The structure may possibly vibrate around its equilibrium position until the relative velocity is low enough for the ice to induce energy into the structure again. This process is then repeated, resulting in the distinctive saw-tooth pattern of both the structural displacement and the global ice load over time (Sodhi and Haehnel, 2003). The maximum global ice load is significantly higher than observed during continuous brittle crushing.

Frequency lock-in

For slightly higher ice velocities frequency lock-in can develop. This regime extends over a range of ice velocities. It is characterized by periodic oscillation of the structure at a frequency close to or equal to one of the natural frequencies of the structure (Hendrikse, 2017). This is because the timing of ductile loading synchronises or 'locks in' with the sinusoidal displacement of the structure. The vibrations of the structure are largely influenced by the damping in the system (Marsman, 2018) and because a large amount of repetitions can occur in this failure regime, FLI can cause structural fatigue (Willems, 2016; Hendrikse and Koot, 2019). FLI typically occurs for structural vibration modes up to 10 [Hz] (Hendrikse, 2017). During FLI, there exists a linear relation between the ice velocity and the maximum structure velocity. The relation is given by:

$$\dot{u}_{max} = \beta v_{ice} \quad (2.16)$$

β [-] is found to be in the range of 1.0 to 1.5, according to multiple test campaigns (Hendrikse and Nord, 2019).

Continuous brittle crushing

For even higher ice velocities, ice crushes continuously. The relative velocity remains high which prevents the ice from deforming in a ductile manner. Therefore, the contact area can not be increased up to the point where significant energy can be transferred into the structure. The result is that the structure hardly responds to the ice loading and the induced forces to the structure are relatively low, oscillating around a mean value. Therefore the effect in terms of ULS and FLS due to CBR are insignificant in comparison to IC and FLI.

3

Ice action on a jacket substructure

In this chapter it will be quantified how many braces and legs in the jacket are subjected to ice failing in crushing or bending as function of the approach angle (θ) and the threshold angle (α). Bending failure is discussed in Section 2-1. The crushing failure mode is discussed in Section 2-2.

To model the jacket the OC4 reference jacket is used (Vorpahl et al., 2013). For the remainder of this chapter, braces and legs together are referred to as 'elements'. It is important to quantify how many elements will cause ice bending and ice crushing failure when ice interacts with the structure, since each failure mode induces a different type of force to the structure. This quantification depends on several parameters. In order to visualise what happens, a model is presented that gives the interaction per brace as function of the approach angle (θ , indicated in Fig.3-1) of the ice relative to the structure.

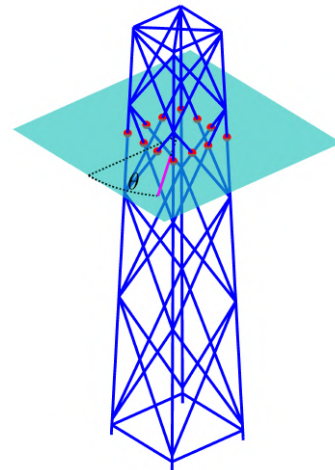


Figure 3-1: Approach angle θ and ice-jacket interaction points

3-1 Threshold angle

When an ice sheet encounters a sloping structure, the ice sheet will be pushed downwards or upwards, depending on the geometry, eventually causing the ice sheet to fail in bending. This is illustrated for upward bending in Fig.3-2.

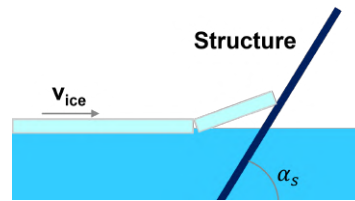


Figure 3-2: Ice failing in upward bending

It is assumed that when an ice sheet runs up (or down) on the inclined x-brace of the jacket, a similar event happens as with ice cones described in Section 2-1. When the ice sheet encounters a near vertical structure, the ice will fail in crushing rather than bending (Hendrikse, 2017). To identify whether bending or crushing occurs it is assumed that there is a 'threshold angle', α [deg], at which the failure mode switches from crushing into bending and vice versa. This threshold angle is not a standard value that can be found in literature. There are multiple studies regarding the bending of ice and it is found that no such value for α exists. It depends on many variables, including ice properties and relative dimensions between ice and structure (Timco and Weeks, 2010). In Fig.3-3 it is illustrated that more crushing will take place when the value of α is decreased. In literature it is found that the angle of ice cones installed on offshore structures ranges from 45 up to 70 [deg] relative to the waterline (Goldstein et al., 2005; Hasegawa et al., 2019; Zhang et al., 2005; Ranta and Polojärvi, 2019; Barker et al., 2005; Gravesen et al., 2005). In IEC 61400-3-1 (2019b), the international standard regarding design requirements for fixed offshore wind turbines, an equation is given to calculate the horizontal load on a structure due to ice being bent upwards or downwards by an ice cone. The formula quoted is valid for slopes in the range $0 < \alpha_s < 70$ [deg]. Since it is assumed that bending of ice on sloping braces can be compared to bending of ice on ice cones, a representative value for α is assumed of 70 [deg]. This implies that when the angle between drifting level ice and the brace of interest, α_s (Fig.3-2), is between 70 and 110 [deg] the ice is assumed to fail in crushing. When this angle is below 70 [deg], the ice is assumed to fail in upward bending and when this angle is above 110 [deg] the ice fails in downward bending. The sensitivity of the value for α is discussed in Section 3-4.

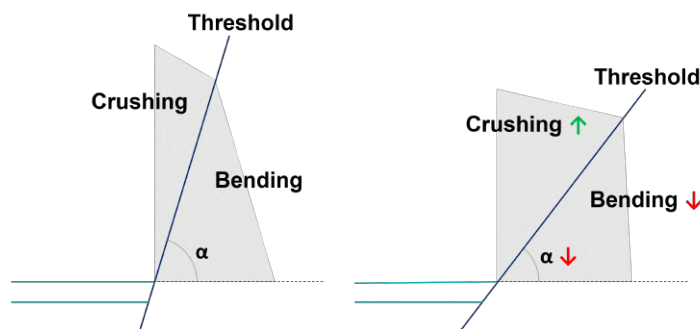


Figure 3-3: Visualized influence of the threshold angle α . A lower threshold angle will lead to more crushing and less bending in the model

3-2 Shielding

In the international standard (ISO 19906, 2019) and in other literature it is found that the 'shielding' effect should be taken into account (Li et al., 2009; Huang et al., 2007; Kato, 1990; Shi et al., 2002). When considering multi-element structures, the front elements provide a shielding effect on any kind of environmental load acting on the back elements, for instance, wind and wave loads (Huang et al., 2007). These shielding effects apply to ice loading as well (Kato, 1990; Shi et al., 2002). The front elements that are interacting first with the ice create slots in the ice. As the ice sheet is pushed towards the back elements by environmental driving forces, it could be that the back elements are completely or partially positioned inside one of these slots, i.e. shielded (Fig.3-4). Therefore, the load on the back elements will be lower than on the front ones. The ratio between the forces on the shielded and the non-shielded elements is called the shielding coefficient (Huang et al., 2007). According to literature, determining the shielding coefficient is a complicated task. It depends on longitudinal and lateral spacing between elements, the ice attack angle and the ratio of element diameter versus ice thickness (Shi et al., 2002). The forcing at the back elements mainly influences the force on the total system and therefore the response of the total jacket to ice loading. The focus in this thesis is to assess what the response is in a single x-brace. Therefore, it is not necessary to compute the force on the back elements precisely. The amount of shielding is determined using vector calculus. The vector representing the approach angle of the ice and the vector from one front element to one back element are compared. When the angle between them is less than 10 [deg] (to account for partially shielded back elements), it is assumed that the back element is shielded by the front element. Note that this is structure dependent and 10 [deg] is found suitable for this OC4 jacket. By investigating this for every element that crosses the water line, the shielded members can be identified.

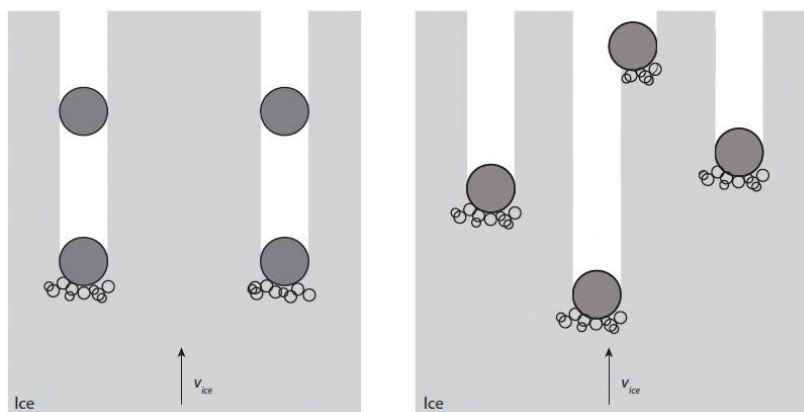


Figure 3-4: Shielding effect for multi-legged structures. Left: back legs fully sheltered by the wake of the front legs. Right: Back leg partially loaded due to wake formed by front leg (Hendrikse, 2017)

3-3 Jamming

The closer the gaps between the elements are, the more shielding will take place. The wake that will be created is then larger compared to the overall size of the structure. This results in a lower total ice force on the jacket, because more elements will be shielded. However, the danger of ice jamming in between the elements increases when they are spaced closer together. When jamming occurs, the total ice load will increase significantly (Määttänen, 1991). According to ISO19906 (2019) ice jamming can usually be expected when the L/w is less than 4. Here L [m] is the clear distance between two elements and w [m] is the diameter of an element. The Type 1 and Type 2 jacket in this thesis have an L/w ratio of 5.5 and 2, respectively. This implies that jamming is likely not to occur at the Type 1 jacket, but could lead to severe forces acting on the Type 2 jacket. However, the reference jacket considered is relatively small compared to the jackets used with the current high capacity wind turbines. The trend towards using larger wind turbines and therefore larger size jackets will reduce the susceptibility of jamming. Therefore, the effect of jamming ice is considered outside the scope of this thesis.

3-4 Quantification of interaction

A MATLAB model is constructed to visualise the interaction as function of the approach angle, θ , and the threshold angle, α . Depending on the input parameters, the model determines what failure mode (bending or crushing) each element is subjected to, while taking into account the shielding effect. The ice can approach the structure over a range of 360 [deg], but since the OC4 jacket is symmetric, only a range of 90 [deg] is considered. In this OC4 model, when the ice passes through the structure at $z = 0$ m (MSL), there are twelve elements crossing the waterline (Fig.3-1), being four legs and eight braces. Computing for each element what angle it makes with the ice direction (α_s), assigning the corresponding failure mode to it and taking into account the shielding effect, Fig.3-5 can be made.

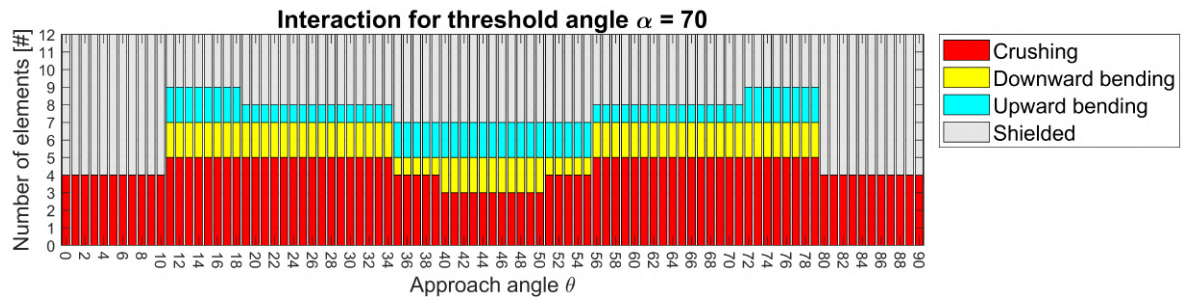


Figure 3-5: Number of elements per failure mode as function of approach angle θ

From this figure it can be seen that the structure is loaded differently depending on the ice approach angle, θ . It was found that nine different failure mode combinations can occur, better illustrated in Fig.3-7. The purple line in Fig.3-7 indicates the direction where the ice is approaching from. A red element indicates that ice impacting this element is failing in crushing. Cyan elements indicate ice failing in upward bending and yellow elements indicate ice failing in downward bending. White elements are shielded by the other elements.

As illustrated in Fig.3-3, the assumed threshold value discussed in Section 3-1 has influence on the amount of bending and crushing that occurs. A case study was performed to quantify the influence of α . It was found that for the geometry of the OC4 jacket, a value of α of 55 [deg] and lower would result in crushing failure only. It is more likely to assume that bending failure will start from higher threshold values, because the inclination angles of the ice cones found in literature go up to values of 70 [deg]. The case study therefore focused on threshold values between 56 and 82 [deg]. Fig.3-6 shows the influence of α , by quantifying the failure modes for $\alpha = \{58, 70, 82\}$.

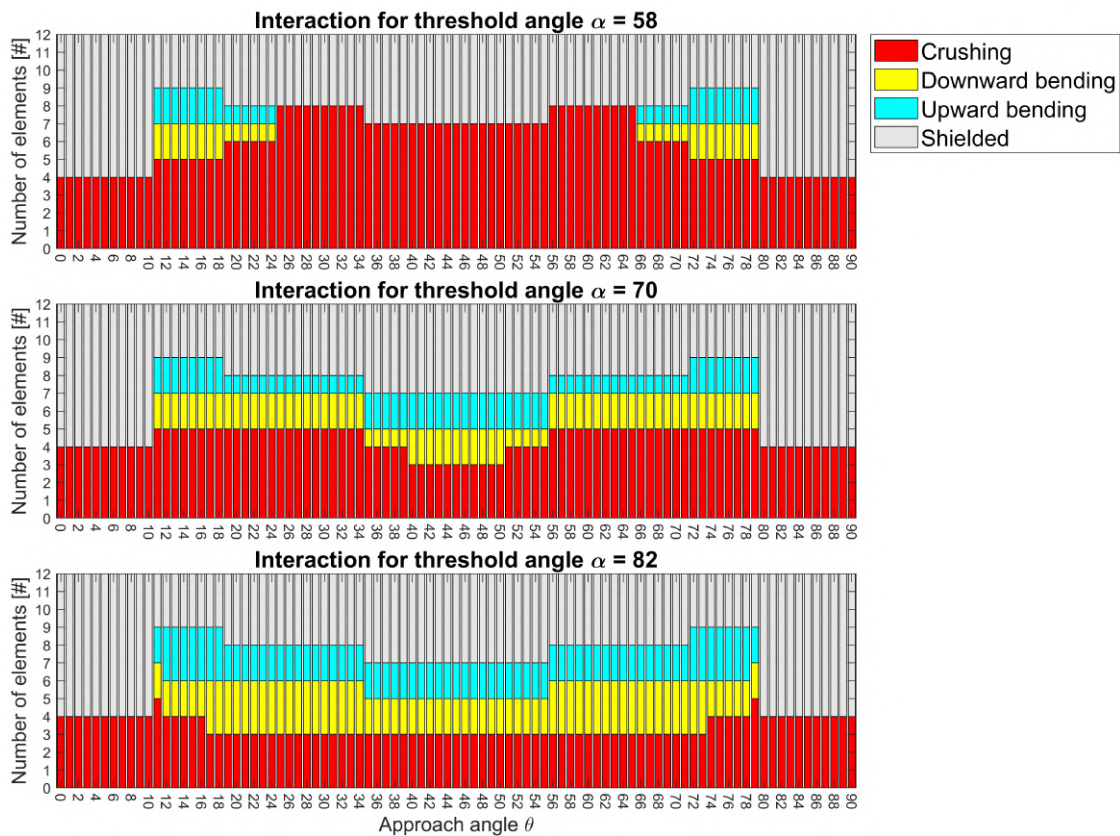


Figure 3-6: Quantification of failure modes as function of θ for $\alpha = \{58, 70, 82\}$

Indeed, a higher threshold angle α will result in more bending and less ice crushing failure. From these illustrations and figures it is deducted that ice crushing as well as ice bending failure is equally significantly present when assuming $\alpha = 70$ [deg]. Therefore, they should both be included in the model.

The analysis in this chapter was performed on the Type 2 jacket, including braces. The Type 1 jacket does not have any braces crossing the waterline, only four legs, which are crossing the waterline close to vertical. Therefore, α_s is close to 90 [deg], resulting in only crushing failure at the Type 1 jacket.

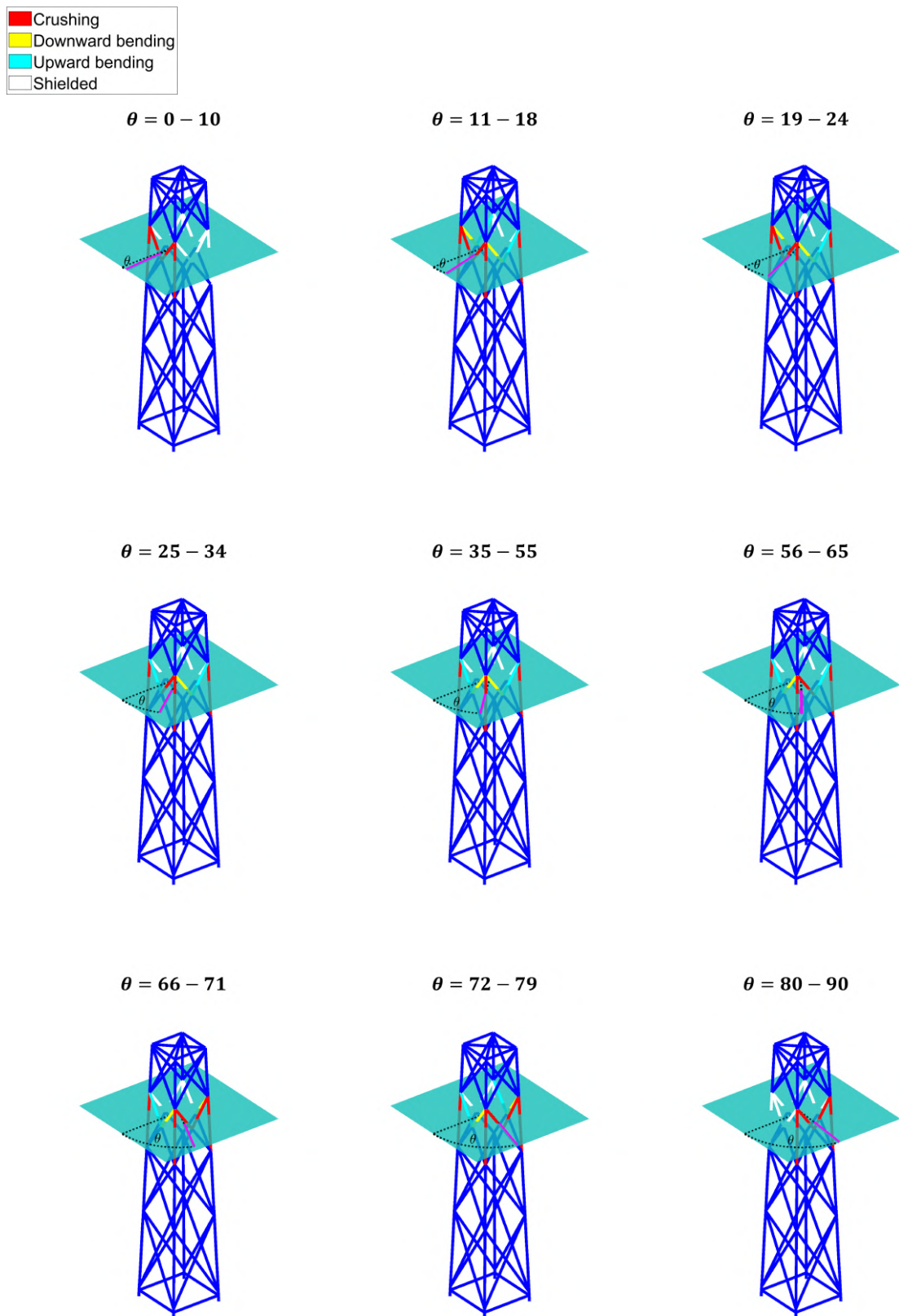
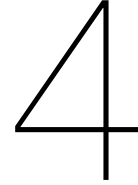


Figure 3-7: Interaction per element for different approach angles θ , $\alpha = 70$ [deg]. The purple line indicates the ice approach angle θ . A red element indicates that ice impacting this element is failing in crushing. Cyan elements indicate upward bending ice failure and yellow elements indicate downward bending ice failure. White elements are shielded by other elements



Forces induced by failing ice

In Chapter 2 both ice bending failure and ice crushing failure have been described. In this chapter it will be discussed how the force induced to the structure by both these ice failure modes can be computed. First, the system of equations regarding ice bending failure will be solved. After that, the force induced to the structure will be computed. At last, the numerical implementation of the ice crushing failure model will be discussed and the forces induced by crushing ice will be assessed.

4-1 Solve ice bending failure equations

In Section 2-1-1 the equation of motion for the ice beam displacement has been derived. To be able to use the ODE45 solver in MATLAB to solve the system, the equation of motion and the boundary conditions need to be rewritten into a system of two first order time derivatives and discretised using the finite difference method. Since it is apparent that the deflection is in the z direction, the subscript z will from now on be omitted from the equations. First, the beam is divided into n elements of length $\Delta x = L/n$ [m]. Each node is indexed by i , resulting in a displacement space of $u_i = u_1 \dots u_n$. The velocities of all the nodes are named $u_{n+1} \dots u_{2n}$. Next, Eq.2.6 is rewritten to give the expression for the acceleration in the beam for each node i . This is done by moving every term apart from the inertia term to the RHS and then dividing the equation by ρA :

$$\frac{\delta^2 u}{\delta t^2} = -\frac{EI}{\rho A} \frac{\delta^4 u}{\delta x^4} - \frac{N}{\rho A} \frac{\delta^2 u}{\delta x^2} - \frac{k}{\rho A} u + \frac{cNv_x}{\rho A} \frac{\delta^3 u}{\delta x^3} - v_x^2 \frac{\delta^2 u}{\delta x^2} + \frac{cN}{\rho A} \frac{\delta^3 u}{\delta x^2 \delta t} - 2v_x \frac{\delta^2 u}{\delta x \delta t} \quad (4.1)$$

Each (higher order) derivative in Eq.4.1 can be approximated using the finite difference method, which is explained in Appendix B. The central finite difference approximation of Eq.4.1 is:

$$\begin{aligned} \frac{\delta^2 u_i}{\delta t^2} = & -\frac{EI}{\rho A \Delta x^4} (u_{i+2} - 4u_{i+1} + 6u_i - 4u_{i-1} + u_{i-2}) - \frac{N}{\rho A \Delta x^2} (u_{i+1} - 2u_i + u_{i-1}) \\ & - \frac{k}{\rho A} (u_i) + \frac{cNv_x}{2\rho A \Delta x^3} (u_{i+2} - 2u_{i+1} + 2u_{i-1} - u_{i-2}) - \frac{v_x^2}{\Delta x^2} (u_{i+1} - 2u_i + u_{i-1}) \\ & + \frac{cN}{\rho A \Delta x^2} (u_{n+i+1} - 2u_{n+i} + u_{n+i-1}) - \frac{v_x}{\Delta x} (u_{n+i+1} - u_{n+i-1}) \end{aligned} \quad (4.2)$$

Here N (Eq.2.7) is approximated by backward difference equations at the right end of the beam, since there is no information outside the domain to use central difference:

$$N = \frac{\frac{-EI\zeta}{\Delta x^3} (u_n - 3u_{n-1} + 3u_{n-2} - u_{n-3})}{1 + \frac{\zeta}{\Delta x} (u_n - u_{n-1}) - \frac{c\zeta}{\Delta x} (u_{2n} - u_{2n-1}) - \frac{cv_x\zeta}{\Delta x^2} (u_n - 2u_{n-1} + u_{n-2})} \quad (4.3)$$

Rewriting Eq.4.2 into a system of first order equations yields:

$$\begin{cases} \frac{\delta u_i}{\delta t} & = u_{n+i} \\ \frac{\delta u_{n+i}}{\delta t} & = \frac{\delta^2 u_i}{\delta t^2} = \text{Eq.4.2} \end{cases} \quad (4.4)$$

For several values of i , information is needed from nodes that are outside the domain. To obtain expressions for these nodes the boundary conditions are used, of which the derivations can be found in Appendix B:

$u_{-1} = u_1$	Deflection at $i = 0$ is zero
$u_0 = 0$	Displacement at $i = 0$ is zero
$u_n = -v_x \Delta t \sin(\alpha_s)$	Displacement at $i = n$ is known
$u_{n+1} = 2u_n - u_{n-1} + \frac{hN\Delta x^2}{2EI}$	Bending moment at $i = n$ is known

The complete discretisation can be formed into a matrix equation of the form:

$$\begin{bmatrix} \dot{u}_1 \\ \dot{u}_2 \\ \vdots \\ \dot{u}_{n-1} \\ \dot{u}_n \\ \ddot{u}_1 \\ \ddot{u}_2 \\ \vdots \\ \ddot{u}_{n-1} \\ \ddot{u}_n \end{bmatrix} = \begin{bmatrix} \mathbf{0} & \mathbf{I} \\ \mathbf{K} & \mathbf{C} \end{bmatrix} \begin{bmatrix} u_1 \\ u_2 \\ \vdots \\ u_{n-1} \\ u_n \\ u_1 \\ u_2 \\ \vdots \\ u_{n-1} \\ u_n \end{bmatrix} + \begin{bmatrix} 0 \\ 0 \\ \vdots \\ \text{BC} \\ 0 \\ 0 \\ 0 \\ \vdots \\ 0 \\ 0 \end{bmatrix} \quad (4.5)$$

Reference is made to Appendix B for the complete matrix equation.

This system of equations is solved in MATLAB using the built-in ODE45 solver. The outcome of this model gives the displacement of the beam as function of time. An example of such an outcome for the input parameters listed in Table 4-1 is shown in Fig.4-1. The ice input properties are based on IEC61400 (2019b), Xu et al (2015) for the ice-structure friction coefficient μ and DNV GL (2014) for ice density ρ .

Table 4-1: Input parameters for the solved deflection in Fig.4-1.

Parameter	Name	Value	Unit
α_s	Slope angle	70	[deg]
μ	Ice-structure friction coefficient	0.15	[-]
ρ	Ice density	917	[kg/m ³]
ρ_w	Water density	1025	[kg/m ³]
b	Beam width	1	[m]
c	Damping coefficient	1000	[s]
E	Yield strength	1e9	[Pa]
h	Ice thickness	0.4	[m]
$ T $	Avg. surface temperature	5	[°C]
v_x	Horizontal ice velocity	0.15	[m/s]

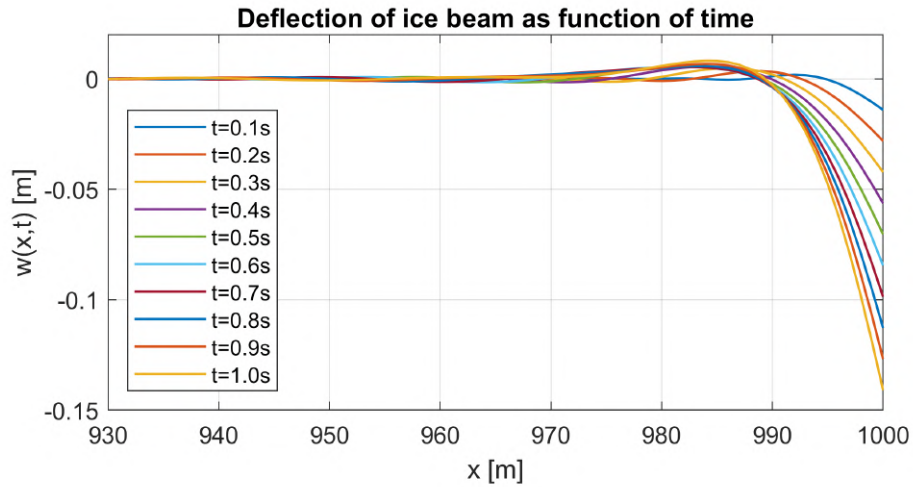


Figure 4-1: Deflection of the ice beam as function of time

The deflection can be converted to bending stress by first computing the internal moment in the beam using the following relation:

$$M = -EI \frac{\delta^2 u_z}{\delta x^2} \quad (4.6)$$

This internal moment can be converted to internal bending stress by (Hibbeler, 2013):

$$\sigma_b = \frac{My}{I} = \frac{M \cdot \frac{h}{2}}{\frac{1}{12}bh^3} \quad (4.7)$$

The axial force N induces a normal stress in the beam that can be computed by:

$$\sigma_n = \frac{N}{A} \quad (4.8)$$

The total tensile stress is the added contribution of the bending stress and the normal stress, illustrated in Fig.4-2.

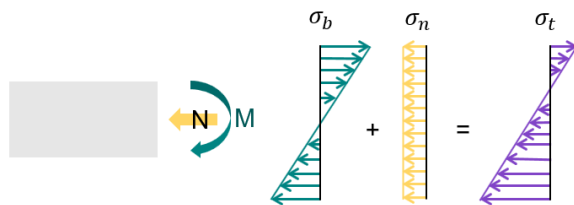


Figure 4-2: Contribution of bending stress and normal stress to total tensile stress

These stress profiles hold for a downward bending beam. The red dot indicates the location of the maximum tensile stress. The resulting total tensile stress as function of time is shown in Fig.4-3.

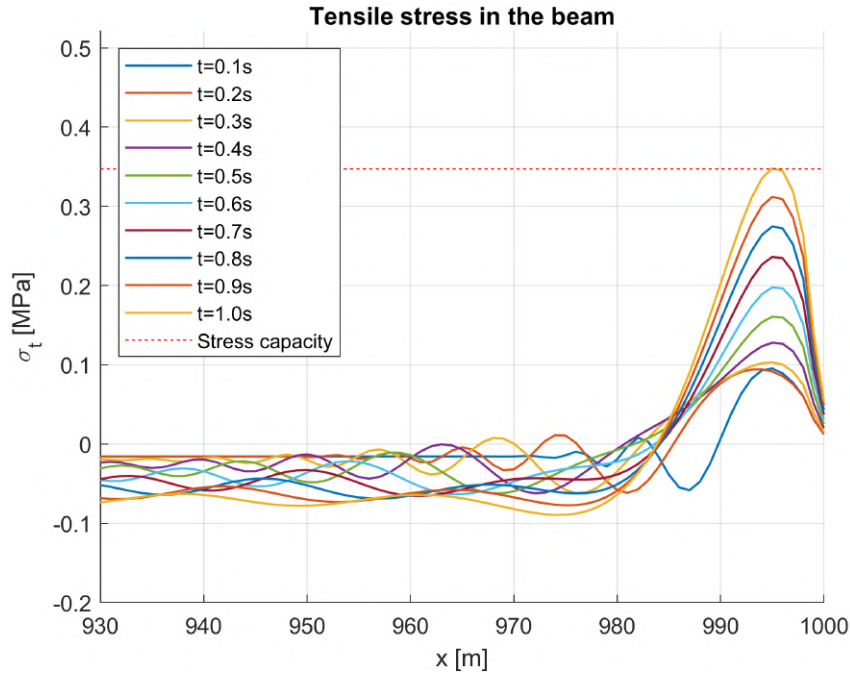


Figure 4-3: Tensile stress as function of time

These results are verified by the results found by Wille et al. (2011). It shows similar behaviour of the deflection as well as the total tensile stress over time.

To determine at which timestamp the ice beam fails, the stress capacity of the ice has to be determined. At the time instant where the total tensile stress exceeds this stress capacity, the ice beam breaks off and the broken part is removed (numerically), i.e. no longer interacting with the structure. It is assumed that the forces induced by broken ice pieces to the structure are significantly smaller than during the interaction phase and can be neglected. The stress capacity of the ice depends on the mechanical properties of the ice and on the ice thickness. According to the research by Timco and O'Brien (1994), whose results are incorporated in the ISO standard (ISO 19906, 2019) the flexural stress capacity of the ice, σ_f [MPa], can be computed as follows:

$$\begin{aligned}\sigma_f &= 1.76 \exp(-5.88\sqrt{V_b}) \\ V_b &= S \left(\frac{49.18}{|T|} + 0.53 \right) \\ S &= 13.4 - 17.4h \text{ for } h \leq 0.34 \text{ [m]} \\ S &= 8.0 - 1.62h \text{ for } h > 0.34 \text{ [m]}\end{aligned}\tag{4.9}$$

Where V_b [ppt] is the brine volume fraction and S [ppt] the salinity. The brine volume fraction equation is derived by Frankenstein and Garner (1967). The salinity equations were presented by Timco and Frederking (1990). Since the Baltic Sea area is considered, $|T|$ is set to 5 [°C], based on the observations by Leppäranta and Lewis (2007). The salinity is dependent on the ice thickness h [m], which makes the flexural stress capacity also dependent of the ice thickness.

4-2 Force induced by ice bending failure

The horizontal force that is acting on the structure (F_H) can be deduced from the equation of motion and the boundary condition at the right end of the beam. The value for F_H can be calculated by rewriting the first equation in Eq.2.10:

$$F_H = -\frac{2EI}{h \cos(\alpha_s)} \frac{\delta^2 u_z}{\delta x^2}(L, t) \quad (4.10)$$

In Fig.4-4 the deflection, total tensile stress and horizontal force induced to the structure are shown for the input parameters listed in Table 4-1.

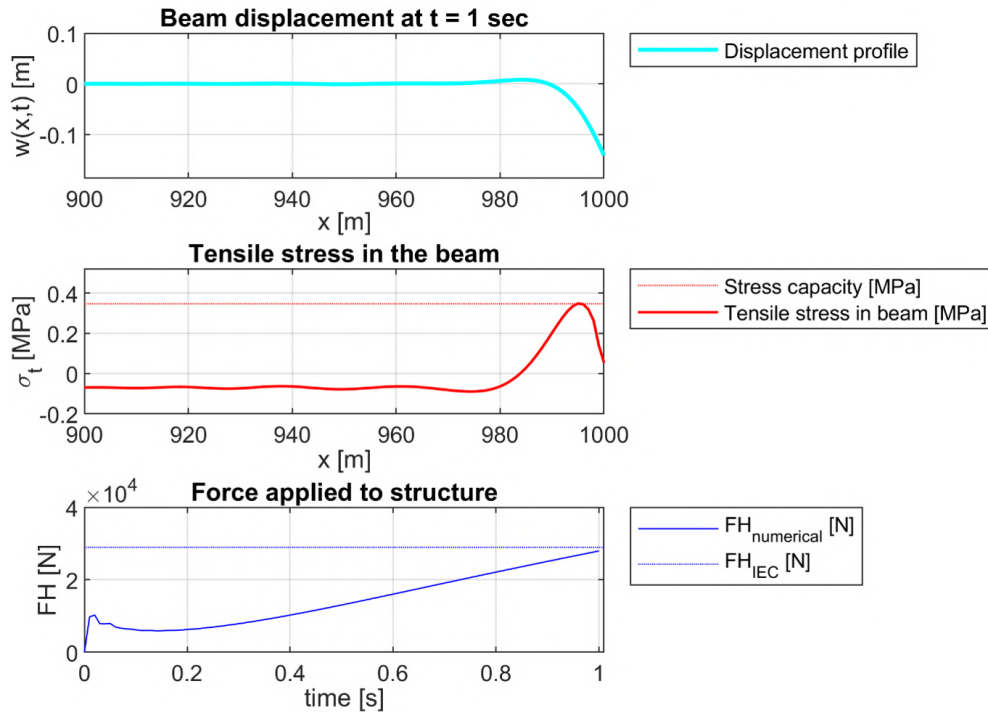


Figure 4-4: Deflection, total tensile stress and horizontal force for an ice beam with parameters listed in Table 4-1

The dashed line in the tensile stress plot indicates the stress capacity of the ice beam. At the time instant where the total tensile stress exceeds this capacity, the beam breaks. For these input parameters the beam breaks after $t = 1$ [s]. The breaking point is at ± 5 [m] from the structure. Altering the input parameters will lead to different values for t and the breaking length. As was discussed in Section 4-1 the part that breaks off is numerically removed and no longer interacting with the structure. Therefore, the force induced to the structure occurs with a certain frequency, dependent of the breaking length, the breaking time and the ice velocity, which will be further discussed in Section 5-2.

The force induced to the structure is shown in the bottom plot of Fig.4-4. Upon impact with the structure the force starts low, after which it gradually increases over time until the beam breaks. The peak around $t = 0$ [s] is because of the sudden acceleration in the first time step, representing the effect of the impact of the ice with the structure. The value of the maximum force induced to the structure is compared to the reference provided in IEC61400-3-1 D.4.4.3 (2019b). Here an equation is provided that can be used to calculate the horizontal force induced by level ice to an offshore structure equipped with an ice cone. The equation is based on research by Ralston (1977, 1980). As is discussed previously, the ice failure at the braces is assumed to be comparable with ice failure at an ice cone. Following the procedure in the IEC code, a reference horizontal force value can be computed. This value is plotted at the bottom of Fig.4-4. What can be seen is that the maximum horizontal force value found by solving the set of equations provided in this thesis, corresponds well to the reference value that can be deducted from the IEC code. Besides the information about the maximum induced force to the structure, now also information is available about the breaking time and the breaking length. These properties can not be deducted from the IEC code, but are important when assessing the dynamic interaction between ice and structure, which is further discussed in Section 5-2.

The force profile shown in Fig.4-4 can be computed for multiple ice velocities, of which the results can be seen in Fig.4-5. What is interesting to see is that the maximum ice force does not depend much on ice velocity and remains in good correspondence with the code, only the breaking time decreases for faster moving ice.

Note that this is a rough approximation of the ice bending load since beam theory instead of plate theory is used. Also, ice buckling is not included and the structure is assumed rigid and not compliant. However, the forces correspond well to the design code and are also verified with the work by Keijndener et al. (2019). Therefore, the forces are assumed sufficiently accurate to use in this thesis.

The analysis in this chapter has been performed on downward bending ice. Instead of constructing a separate model for upward bending ice, the load induced is approximated by a different method. Since it was found that the maximum ice load is corresponding well to the IEC code, the ratio between maximum force induced by downward and upward bending ice is deducted from the IEC as well. Here it was found that the horizontal force induced by upward bending ice is a factor 1.2-1.4 higher than induced by downward bending ice. Infor-

mation about the breaking time and length is not further assessed for upward bending ice and should be investigated in further research. For now it is assumed that the characteristics are comparable to downward bending ice.

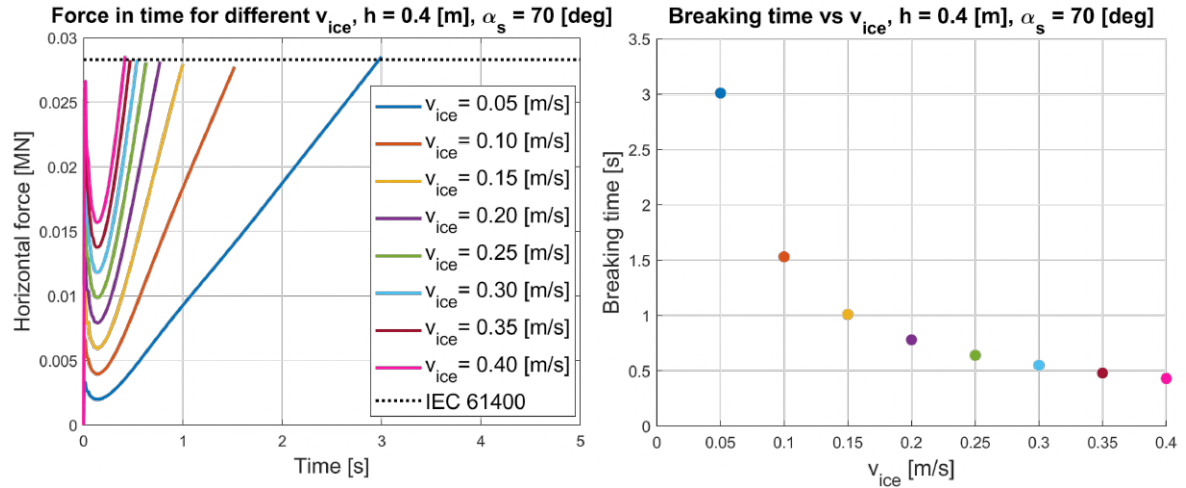


Figure 4-5: Left: Induced horizontal force profiles for multiple ice velocities. Right: Breaking time for multiple ice velocities

4-3 Force induced by ice crushing failure

In Section 2-2 the phenomenological ice model as described by Hendrikse and Nord (2019) has been introduced. In this section the numerical implementation of this model will be discussed.

4-3-1 OC4 model

Since the forces induced by ice crushing onto the structure are dependent of the motion of the structure itself, first a structural model based on the OC4 reference jacket (Vorpahl et al., 2013) is constructed that will be implemented in MATLAB. It consists of a jacket substructure, a transition piece and a tower-RNA assembly, designed for a 5 [MW] wind turbine in waters of 50 [m] deep (Jonkman et al., 2009). All elements of the structure are modelled as Timoshenko beam elements. The connection to the seabed is assumed rigid (clamped at seabed level) and the RNA is modelled as a lumped mass, thereby not taking into account the (dynamics of the) individual blades. Marine growth is added to the parts of the structure lower than 2 [m] below mean sea level. The legs are flooded with water, increasing the mass of these elements. The TP is modelled as a heavy rigid block by increasing the stiffness at interface. The mass of the TP is represented by four lumped masses at the top corners of the jacket.

Combining all elements and point masses in MATLAB yields the system of equations describing the offshore wind turbine as:

$$\mathbf{M}\ddot{\mathbf{x}} + \mathbf{C}\dot{\mathbf{x}} + \mathbf{K}\mathbf{x} = \mathbf{f}(t) \quad (4.11)$$

Where \mathbf{M} is the mass matrix, \mathbf{C} is the damping matrix and \mathbf{K} is the stiffness matrix. The form of \mathbf{C} will be Rayleigh damping, further discussed in Section 6-5.

4-3-2 Modal analysis

Instead of solving the system in the time domain, it is preferred to solve it in the modal domain, for which there are two main reasons. Firstly, the equations of motion will decouple, allowing to solve the set of equations separately. Secondly, the solution space can be truncated, meaning that not all modes are included in the system of equations, yielding a smaller set of equations to be solved, reducing computational time.

When a harmonic free vibration with frequency ω [rad/s] is assumed, the eigenvalue problem of Eq.4.11 is:

$$(\mathbf{K} - \omega_i^2 \mathbf{M})\boldsymbol{\phi}_i = \mathbf{0} \quad (4.12)$$

Solving this system yields the eigenfrequencies ω_i and the corresponding eigenvectors $\boldsymbol{\phi}_i$. The solution of the equations of motion of the structure can then be expressed as a superposition of the eigenmodes, written as:

$$\mathbf{x}(t) = \sum_{i=1}^N \boldsymbol{\phi}_i \eta_i(t) = \boldsymbol{\Phi} \boldsymbol{\eta}(t) \quad (4.13)$$

Where N is the number of eigenmodes of the system, corresponding to the number of degrees of freedom (DoFs). $\boldsymbol{\Phi}$ is the eigenmatrix, containing the eigenmodes and $\boldsymbol{\eta}$ is the vector of modal displacements.

The eigenmodes are orthogonal with respect to the mass and stiffness matrices. Therefore the modal mass and modal stiffness matrices will be diagonal. Since the damping matrix is constructed by means of Rayleigh damping (Section 6-5), it will be diagonal as well.

When not all N eigenmodes are included in the modal system, the system is truncated. The truncated solution will then be of the form:

$$x = \sum_{i=1}^k \phi_i \eta_i = \Phi \eta = x_t \quad (4.14)$$

Substituting this truncated solution in Eq.4.11 yields:

$$M \Phi_t \ddot{\eta}_t + C \Phi_t \dot{\eta}_t + K \Phi_t \eta_t = \mathbf{f} + \mathbf{r} \quad (4.15)$$

Because the system is truncated, a residual force \mathbf{r} remains. However, because of the orthogonality principle, $\Phi^T \mathbf{r} = \mathbf{0}$. Pre-multiplying by the truncated eigenmatrix will therefore yield the reduced set of equations of motion:

$$\begin{aligned} \Phi_t^T M \Phi_t \ddot{\eta}_t + \Phi_t^T C \Phi_t \dot{\eta}_t + \Phi_t^T K \Phi_t \eta_t &= \Phi_t^T \mathbf{f} \\ M_t^* \ddot{\eta}_t + C_t^* \dot{\eta}_t + K_t^* \eta_t &= \mathbf{f}_t^* \end{aligned} \quad (4.16)$$

This system of equations is solved in MATLAB by the implemented ODE45 solver. This is convenient because the ice equations of motion will also be solved through this solver. Therefore, both systems of equations can be solved simultaneously. The set of equations in Eq.4.16 is first transformed into a system of first order differential equations by means of a state space representation, of which the state vector is defined as:

$$y = \begin{bmatrix} \eta_t \\ \dot{\eta}_t \end{bmatrix} \quad (4.17)$$

Substituting this state vector in Eq.4.16 yields the set of first order equations:

$$\dot{y} = \begin{bmatrix} \dot{\eta}_t \\ \ddot{\eta}_t \end{bmatrix} = \begin{bmatrix} \mathbf{0} & \mathbf{I} \\ -\mathbf{K}_t^* & -\mathbf{C}_t^* \end{bmatrix} \begin{bmatrix} \eta_t \\ \dot{\eta}_t \end{bmatrix} + \begin{bmatrix} \mathbf{0} \\ \Phi_t^T \end{bmatrix} \mathbf{f} \quad (4.18)$$

Where the ice force \mathbf{f} is a function of the relative motion between ice and structure. Therefore, a coupling has to be constructed, which is discussed in the next section.

Coupling structure and ice

Since the displacement of the structure is computed in the modal domain and the ice equations in the spatial domain, the modal displacements η_i need to be transferred to the spatial domain again in order to couple both systems. Assume degree of freedom p is loaded by ice, then the structural displacement at DoF p can be found by:

$$x_s = \begin{bmatrix} \phi_{p,1} & \phi_{p,2} & \phi_{p,3} & \dots & \phi_{p,k} \end{bmatrix} \begin{bmatrix} \eta_1 \\ \eta_2 \\ \eta_3 \\ \vdots \\ \eta_k \end{bmatrix} = \Phi_{t,p} \eta_t \quad (4.19)$$

The structural displacement of DoF p where the ice acts can be found by multiplying the row in the eigenmatrix corresponding to DoF p by the vector of modal displacements. This yields the value of the structural displacement at the ice-structure interaction point which is needed as a value for x_s in the ice equations, Eq.2.14 and 2.15.

Both the structural and the ice equations of motion can be incorporated in the same solver, allowing to solve the coupled system simultaneously. The coupled system is solved until one ice element breaks. The detection of breaking is handled by an event function, embedded within the ODE45 solver. Upon breaking, the displacements, velocities and forces are stored. The broken ice element is set-back as described in Section 2-2 and this procedure is repeated for the full length of the simulation time.

Crushing load versus bending load

With this coupled system, ice-structure interaction problems can be solved. As an output, the structural displacements and the global induced ice force can be deduced. The response of the structure will be discussed in Chapter 5. When one computes the global ice force induced to the structure for multiple ice velocities, the plot shown in Fig.4-6 can be made. Here, ice with a thickness of $h = 0.4$ [m] is interacting with a Type 2 structure, assuming an ice approach angle of $\theta = 0$ [deg], thereby loading two legs and two braces in crushing simultaneously (Fig.3-7). The force induced to one of the legs is divided by the leg diameter to obtain the force induced per meter width of the structure.

What can be concluded from Fig.4-6 is that for low ice velocities below 0.03 [m/s], the induced force is the highest, which will be further discussed in the next chapter. For higher ice velocities, both the maximum and mean induced force are significantly lower, oscillating around a mean value. What holds for all ice velocities, is that the induced force by ice crushing is much higher than for the ice bending case. For an ice thickness of $h = 0.4$ [m],

the induced force by ice bending is close to 30 [kN/m], for all ice velocities (Fig.4-5). For ice crushing, the maximum induced force is a factor 20-40 higher, depending on ice velocity. What can be concluded is that ice crushing load is much more significant to take into account for the design of the structure than ice bending load.

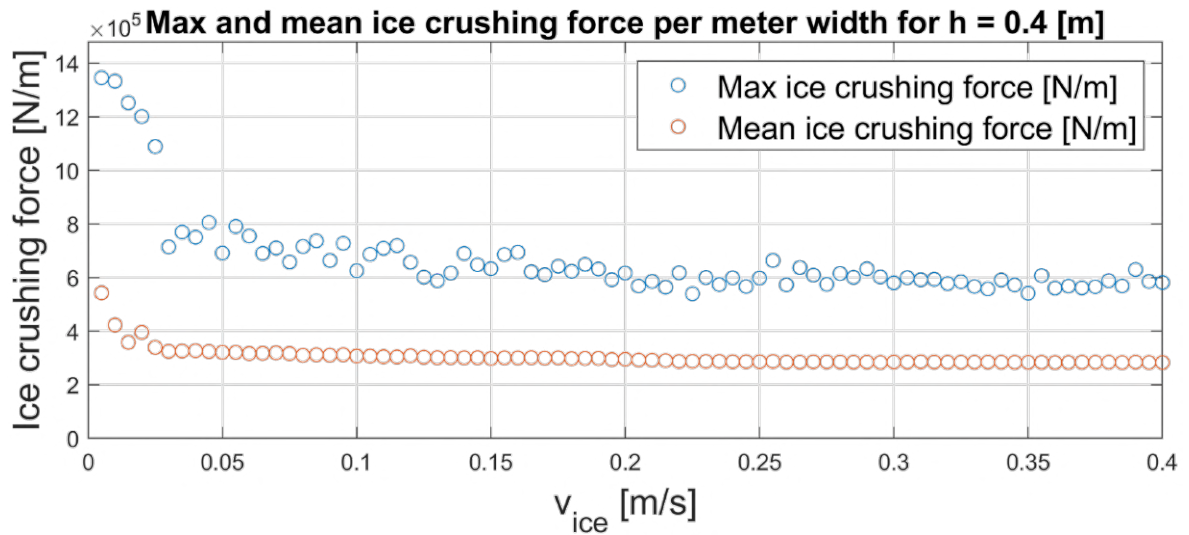


Figure 4-6: Maximum and mean crushing force per meter structure width as function of ice velocity, $h = 0.4$ [m]

5

Ice models applied to the structure

Now that it is defined what forces both ice failure types will induce to the structure, the forces can be applied to the jacket model. This chapter will discuss the numerical simulations performed, in order to answer the first research question. First, a global motion analysis will be performed, indicating the difference in terms of global motion between the Type 1 and Type 2 jacket. After that, the forces induced by ice bending and ice crushing failure will be applied to the Type 2 jacket in order to investigate the dynamic (local) response. Furthermore, a base shear check is executed, as this is typically done for jacket substructures. Finally, the ULS brace load will be assessed, which is found to be of great importance for the design.

5-1 Global motion analyses

Two types of jackets are considered, Type 1 without and Type 2 with x-braces crossing the waterline (Fig.1-5). Type 2 is represented by the OC4 jacket model and Type 1 is a modified version of it, where the x-braces at waterlevel are removed and the remaining bays are changed in height. Coupling each jacket to a tower-RNA assembly yields two different systems. It is important to assess what the natural frequencies of both systems are and if any significant differences exist between the global motion characteristics of the two systems. The first five distinct eigenfrequencies and eigenmodes of both systems are given in Table 5-1. From the table it can be deduced that both systems have similar global behaviour, only the Type 1 system is less stiff in the torsional direction, as is expected. From practice it is known that the first bending mode can interfere with the rotor frequency and the second bending mode is important because it has the largest amplitude around mean sea level, meaning that lots of energy can be put into this second mode. It can also interfere with higher rotor dynamics, for example the 6P rotor frequency.

To analyse these modes a frequency response function (FRF) is used. First, a modal amplitude FRF is obtained by applying a sinusoidal load with frequency Ω [rad/s] to node p in the system, after which the response of node i is computed. The function in Eq.5.1 then demonstrates how the quotient $\frac{\hat{u}_i}{\hat{F}_p}$ depends on the load frequency Ω , where \hat{u}_i is the response of node i in the system and \hat{F}_p the load function (Spijkers et al., 2005).

$$H_{u_i F_p}^A(\Omega) = \frac{\hat{u}_i}{\hat{F}_p} = \frac{1}{\sqrt{\left(1 - \left(\frac{\Omega}{\omega_i}\right)^2\right)^2 + \left(2\xi_i \frac{\Omega}{\omega_i}\right)^2}} \frac{1}{\omega_i^2 m_{ii}^*} \hat{x}_{pi} \quad (5.1)$$

Here ω_i , ξ_i and m_{ii}^* are the modal frequency, modal damping ratio and modal mass, respectively. The amplitude FRF can then be obtained by:

$$H_{x_q F_p}(\Omega) = \frac{x_q}{\hat{F}_p} = \sqrt{(C_{qF_p})^2 + (D_{qF_p})^2} \quad (5.2)$$

In which:

$$\begin{aligned} C_{qF_p} &= \sum_{i=1}^{N_s} \hat{x}_{qi} H_{u_i F_p}(\Omega) \sin(\phi_i) \\ D_{qF_p} &= \sum_{i=1}^{N_s} \hat{x}_{qi} H_{u_i F_p}(\Omega) \cos(\phi_i) \\ \phi_i &= \arctan\left(\frac{2\xi_i \frac{\Omega}{\omega_i}}{1 - \left(\frac{\Omega}{\omega_i}\right)^2}\right) \end{aligned} \quad (5.3)$$

Here ϕ_i [rad] is the phase shift between applied load and response.

Table 5-1: First five eigenfrequencies of both systems

Mode	Modeshape	Type 1	Type 2
		Frequency [Hz]	
1	1 st Bending mode	0.307	0.305
2	2 nd Bending mode	1.161	1.245
3	1 st Torsional mode	2.203	3.057
4	3 rd Bending mode	3.952	4.002
5	1 st Breathing mode	5.211	5.198

By applying a symmetric load with respect to the vertical axis to the nodes at water level and having the interface node as an output node, an energy spectrum can be formed (Fig.5-1). Note that the tower-RNA assembly is not illustrated here.

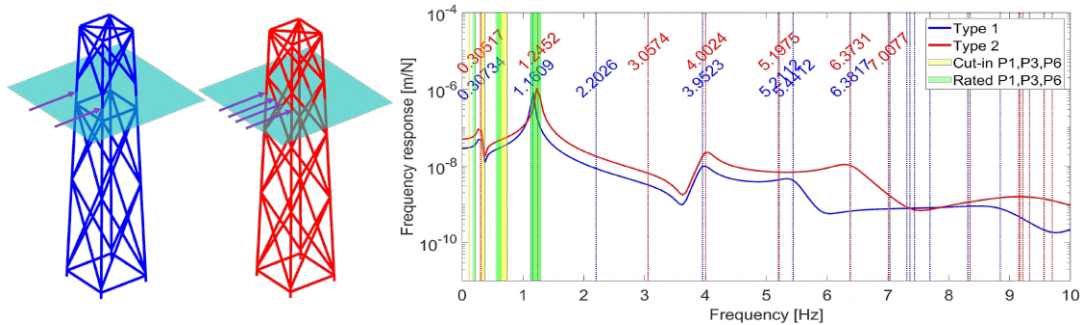


Figure 5-1: Amplitude FRF for symmetrical load (→) around vertical axis - Type 1 vs Type 2

The yellow and green bands indicate the 1P, 3P and 6P rotor frequencies. These are based on the 5 [MW] reference turbine that is used together with the OC4 jacket (Jonkman et al., 2009). A 7% positive and negative margin is accounted for around the rotor frequencies, resulting in a frequency band of rotor frequencies. The structure’s eigenfrequencies must not coincide with the rotor frequencies, as resonance can occur accordingly, negatively affecting the structure’s lifetime. Considering the FRF plots, around the first and second bending mode there are no severe differences between both systems. The only difference is that the peak in the second bending mode for the Type 2 system is higher due to the higher amount of loaded elements, resulting in a larger response. It can also be seen that the second eigenfrequency is interfering with the 6P frequency of the rotor, but since both a reference jacket and a reference turbine that is designed for it is considered, it is assumed that this is poor design in terms of 6P interference of the reference structures and this will not be further discussed. No torsional mode is excited in this analysis, because the jackets are loaded symmetrically around the vertical axis. To investigate the response in the torsional mode, both jackets are loaded at a single side only, of which the amplitude FRF can be seen in Fig.5-2. Again the tower-RNA assembly is not illustrated.

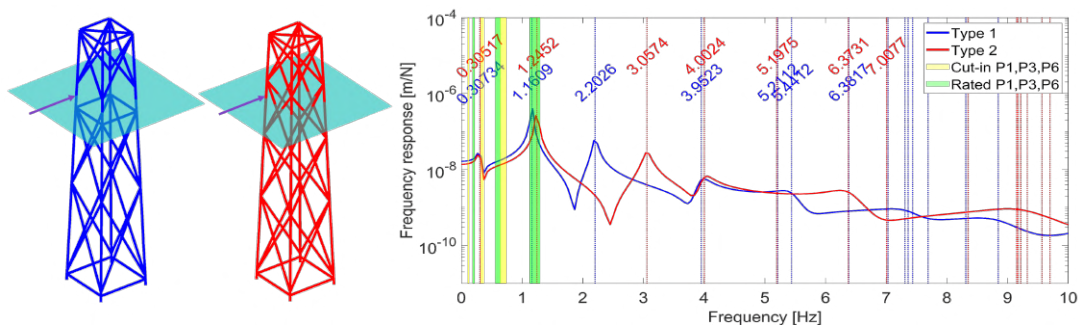


Figure 5-2: Amplitude FRF for unsymmetrical load (→) around vertical axis - Type 1 vs Type 2

Here it can be seen that the FRF of the Type 1 system is higher in the first torsional mode and that the natural frequency of that mode is lower, as expected. This could be important in unsymmetrical ice loading, during yaw-errors in the RNA or during wind-wave misalignment, as the Type 1 system is more susceptible to these kind of loads. Based on both these FRF analyses it can be concluded that there is no significant difference between both systems, resulting that the Type 2 jacket is equally as useful as the Type 1 jacket in terms of global motion.

5-2 Local motion analyses - Ice bending failure

In order to investigate the local motion of the structure due to loads applied to it, the Newmark method (Newmark, 1959) is used to solve the equations of motion representing the structure. The procedure of the method is explained in Appendix C.

The forces illustrated in Fig.4-5 can be applied to the structure to analyse the response. However, periodicity in the load due to the breaking time and length are not yet incorporated in the force profile. In the numerical approximation of ice bending failure, it takes some time for a new piece of ice to arrive when a piece of ice breaks off, inducing a periodic loading. It is important to assess that this loading frequency does not coincide with the structure frequency, as was also found by Yue and Bi (2000), Ji and Oterkus (2016), Xu et al (2015), Kärnä and Jochmann (2003) and by Croasdale and Metge (1991), since this could result in dynamic amplification. It was found that the bending model predicts the breaking length to be 10 times the ice thickness (Fig.5-3, left). Combining that with the information about the breaking time dependent of ice velocity (Fig.4-5, right), the failure frequency can be computed as function of ice velocity, shown at the right in Fig.5-3.

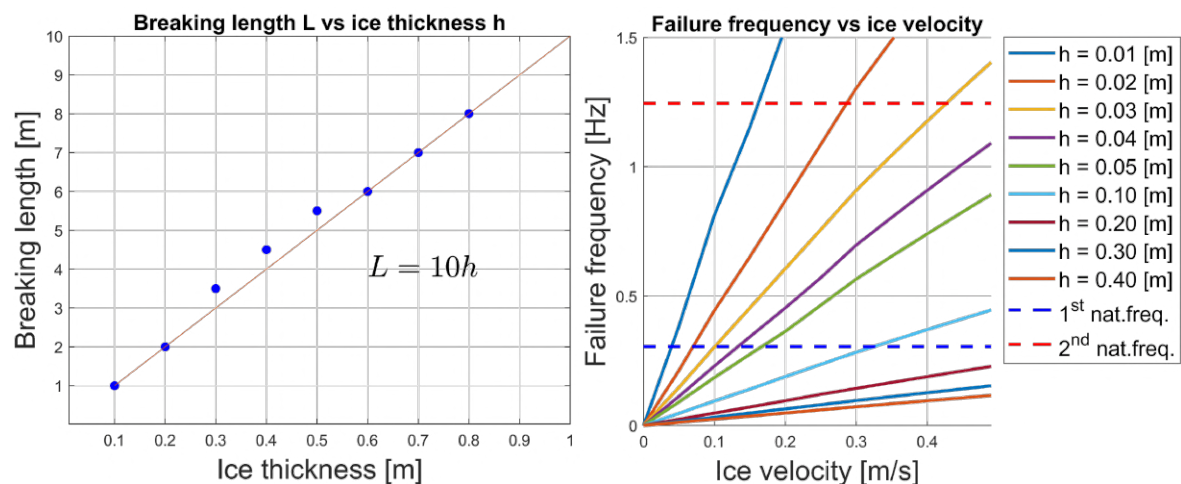


Figure 5-3: Left: Relation of ice thickness versus breaking length, Right: Failure frequency as function of ice velocity for $L = 10h$

The first and second natural frequency of the Type 2 system are plotted too. It can be seen that for small ice thicknesses the frequency of ice failing in bending could coincide with the structure frequency. In literature it was found that the breaking length is between 5 and 10 times the ice thickness, indicating that this model predicts the strength of ice to be on the stronger side, which is conservative. However, the influence on the failure frequency due to weaker ice should be assessed as well. This is shown in Fig.5-4 in case the breaking length is 5 times the ice thickness. It can be seen that now also for thicker ice the failure frequency could coincide with the structure frequency.

With this model, dynamic amplification at individual braces can not be induced. Since the brace eigenfrequency is > 10 [Hz], dynamic amplification could in theory occur for very high ice velocities, however these have never been observed in the Baltic Sea.

Note that these findings hold for the assumptions made in this thesis. In reality, the broken off part of the ice keeps interacting with the structure, instead of being removed. Different ice failing modes could be initiated, outside the scope of this thesis. For example, a pile of ice rubble could accumulate in front of the interaction point, causing the ice to fail in a different way than computed by the model, due to the change of boundary conditions. Small pieces of accumulated ice could for instance cause ice failing in crushing, inducing a kind of damping, mitigating the failure frequency coinciding phenomenon as seen before. On top of that, the ice could also fail due to splitting, also mitigating the possibility of coinciding frequencies. Therefore, ice bending failure is likely not inducing any dynamic amplification in reality. Crushing failure on the other hand is more critical in terms of dynamic amplification, as will be discussed in the next section.

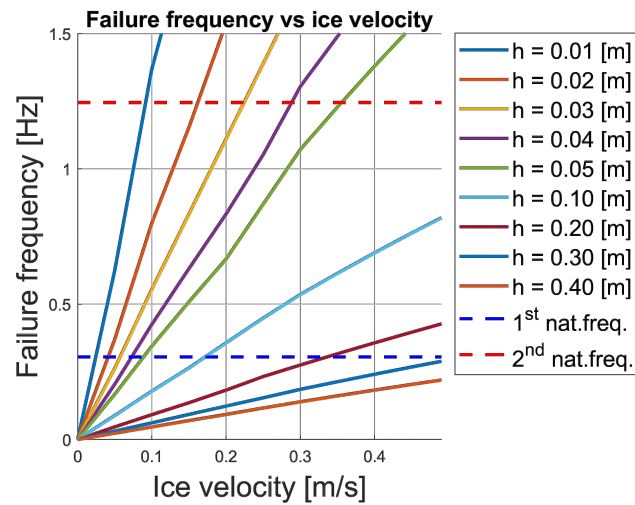


Figure 5-4: Failure frequency as function of ice velocity for $L = 5h$

Applying the loads taking into account the periodicity and solving the equations of motion with the Newmark method, yields the displacement of all the nodes in the system over time, as illustrated in Fig.5-5. In this example, an ice approach angle θ is assumed of 40 [deg], resulting in having two braces causing upward and two braces causing downward ice bending failure, indicated by cyan and yellow braces, respectively. An ice thickness h of 0.4 [m] is considered moving with a horizontal velocity of 0.15 [m/s]. It can be seen that the response is very small due to the loads induced, concluding that these ice bending loads are not important for the design.

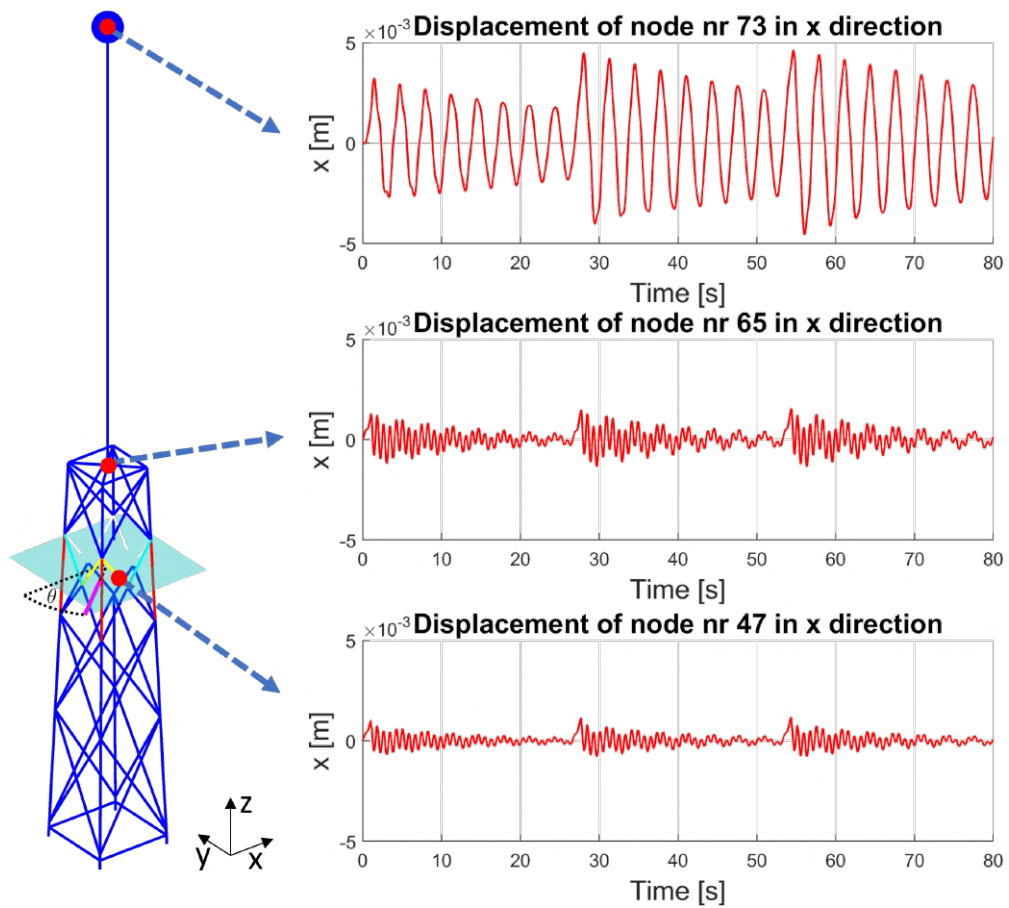


Figure 5-5: Structure responses due to periodic loads induced by ice failing in bending

5-3 Local motion analyses - Ice crushing failure

In the research done by Marsman (2018) it was found that in terms of global motion, the three regimes as described by Hendrikse and Nord (2019) and illustrated in Fig.2-6 can occur at jacket supported wind turbines due to crushing ice loading. To assess whether these regimes could also occur at local brace level, crushing ice load with a thickness of $h = 0.4$ [m] is applied to the jacket structure at the legs as well as at the braces (Fig.5-6). The ice velocity is varied from 0.005 [m/s] to 0.4 [m/s]. Next, the average maximum displacement (AMD) was computed of the loaded legs and braces (Fig.5-6), as this is a good indicator to distinguish the different regimes.

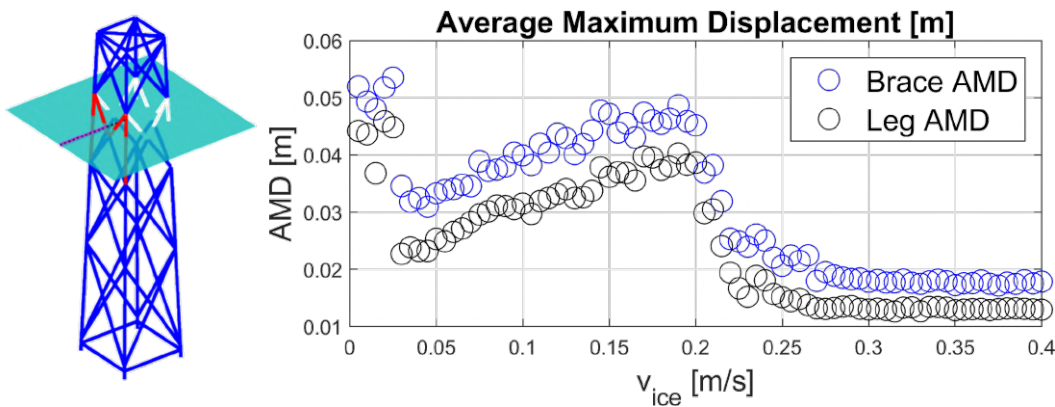


Figure 5-6: AMD of legs vs braces

What can be seen is that for ice velocities lower than 0.03 [m/s], IC occurs, characterised by high displacements. Then, for ice velocities between 0.03 and 0.21 [m/s], FLI can be distinguished. For higher ice velocities, the regime switches to CBR. It was expected that the AMD plot of the braces would appear differently than that of the legs, however, they look similar. This would indicate that no difference in terms of regime identification exist between the response of the legs and braces. However, if the displacement plots are compared, as seen in Fig.5-7 for an ice velocity of 0.075 [m/s], there is a clear difference. Now the legs are in FLI, whereas the braces are in a mix of IC and FLI. This characteristic can not be traced back in the AMD plot, which means that the regimes occurring at the braces are 'overshadowed' by the global motion of the structure.

Therefore, in order to better analyse the local regimes, the local motion is extracted from the total motion. This is done by subtracting the average global displacement from the brace displacement in order to obtain the local brace displacement. Essentially, the influence of the global motion is removed from the total displacement, as indicated in Fig.5-8.

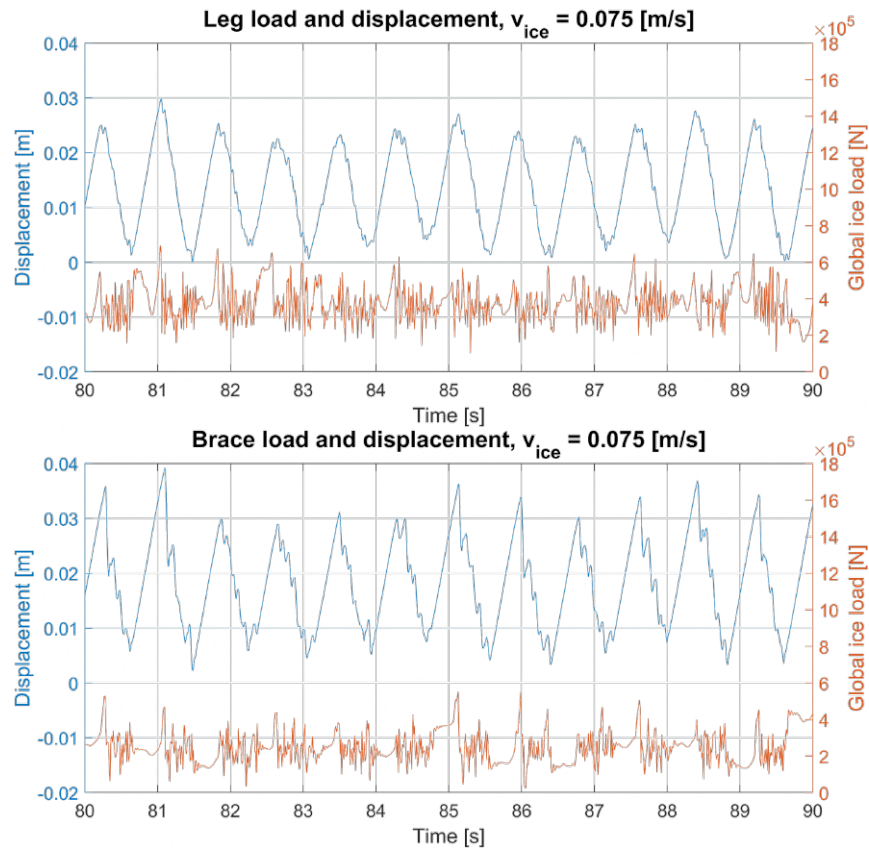


Figure 5-7: Regime comparison between legs and braces for $v_{ice} = 0.075$ [m/s]

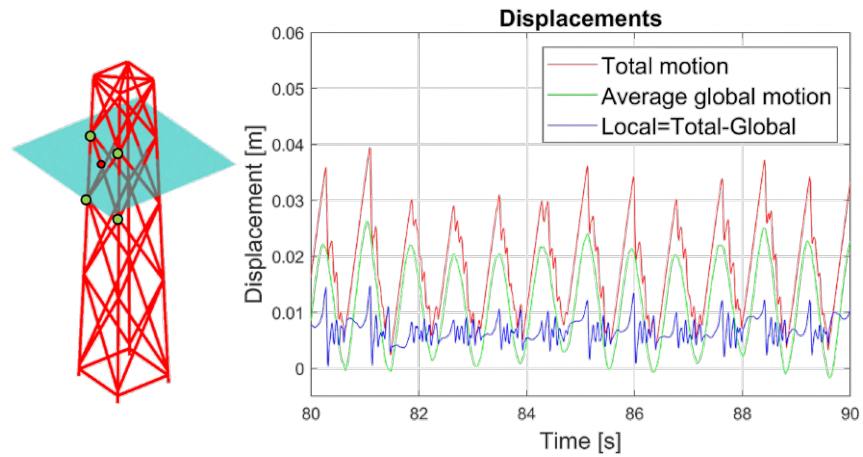


Figure 5-8: The global motion at interaction level is obtained by computing the average displacement of the green nodes scaled to interaction level. This global motion is subtracted from the total displacement of the red node, obtaining the local motion indicated in blue. Here the ice velocity is 0.075 [m/s]

An average maximum local displacement (AMLD) plot of this local motion as function of ice velocity is shown in Fig.5-9. What can be deduced from this plot, is that the displacement at the brace nodes is higher in comparison to the leg displacement and is more fluctuating, however no clear local IIV regimes can be distinguished here.

What is however remarkable, is that the local displacement profile of the brace (Fig.5-8, blue) matches exactly with the global brace ice load profile (Fig.5-7, orange), better illustrated in Fig.5-10. In the simulation time plotted, the brace is loaded three times and pulled back through the ice two times. The high peaks are corresponding to the second natural frequency of the jacket, which is 1.245 [Hz], indicating that the jacket is vibrating globally in its second bending mode. When the jacket oscillates back opposite to the direction of ice movement, the brace is dragged through the ice and starts to vibrate in one of its eigenmodes. It was found that the maximum velocity of the brace during this vibration matches the ice velocity, which typically suggests FLI (Fig.5-11, bottom left). Therefore, this phenomenon can be called local FLI.

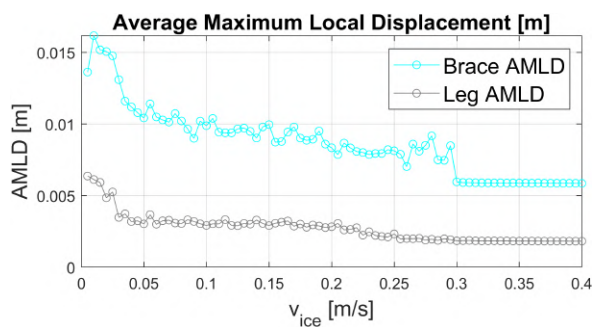


Figure 5-9: AMLD of local leg and brace displacement

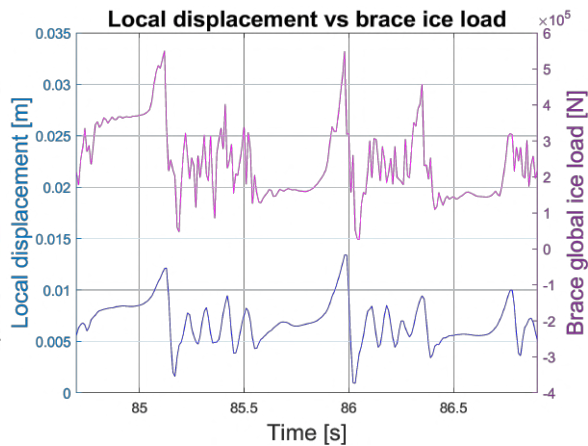


Figure 5-10: Local displacement profile matches with global ice load profile on the brace

However, this does not occur for all ice velocities, as illustrated in Fig.5-11. Here the brace velocity and displacement are plotted for three different ice velocities, being 0.025, 0.075 and 0.145 [m/s]. What can be seen is that the brace is oscillating differently in these situations when dragged back through the ice. For low ice velocities (0.025 [m/s]), the maximum brace velocity does not match with the ice velocity and is even higher than the ice velocity, resulting in short time-periods of no contact between ice and brace. For the intermediate ice velocity (0.075 [m/s]), the maximum brace velocity matches with the ice velocity and as discussed, this suggests local FLI. For higher ice velocities (0.145 [m/s]), the maximum brace velocity is lower than the ice velocity, indicating that the brace is vibrating while in contact with the ice, but not locked-in to the failure of ice. These vibrations are important to consider when FLS is assessed, further discussed in Section 8-2.

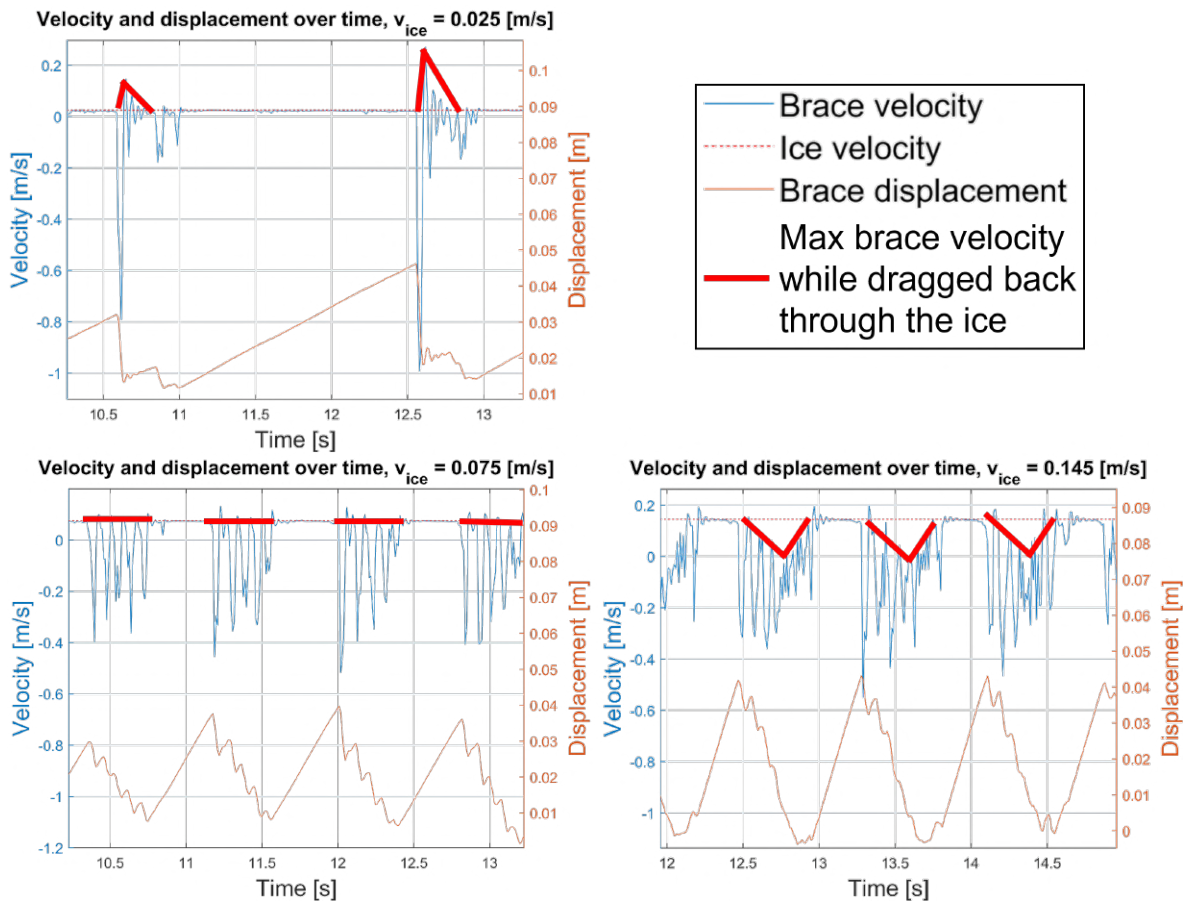


Figure 5-11: Loaded brace velocity and displacement for $v_{ice} = \{0.025, 0.075, 0.145\}$ [m/s]. Although the brace is vibrating in one of its eigenmodes upon being dragged back through the ice (caused by the global motion being opposite to the ice direction) for all ice velocities, the vibration does not always correspond to local FLI

As is clear, in the situations where local FLI is occurring, it is not sustained, as it is governed by the global motion of the jacket. Only local FLI could be observed when the structure is globally vibrating opposite to the ice direction. Therefore, the case studies described in the next section were performed to check whether sustained local FLI could develop.

5-3-1 Case studies

Since no clear IC and no sustained local FLI could be identified in the braces of the regular Type 2 jacket, a case study was performed on a modified jacket model having very stiff legs and flexible braces to see whether these IIV could build up in the braces. The purpose of the stiff legs is to ensure that the global motion is very limited and the flexibility of the braces is to make them more susceptible to IIV. The brace frequency was adjusted from being 11.8 [Hz] to 4.9 [Hz], by reducing the wall thickness by a factor 20, as well as reducing the yield strength by 25%. To make the legs more stiff, the wall thickness was increased by a factor 6. Again, crushing ice load was applied according to Fig.5-6 and the resulting AMD plot is shown in Fig.5-12.

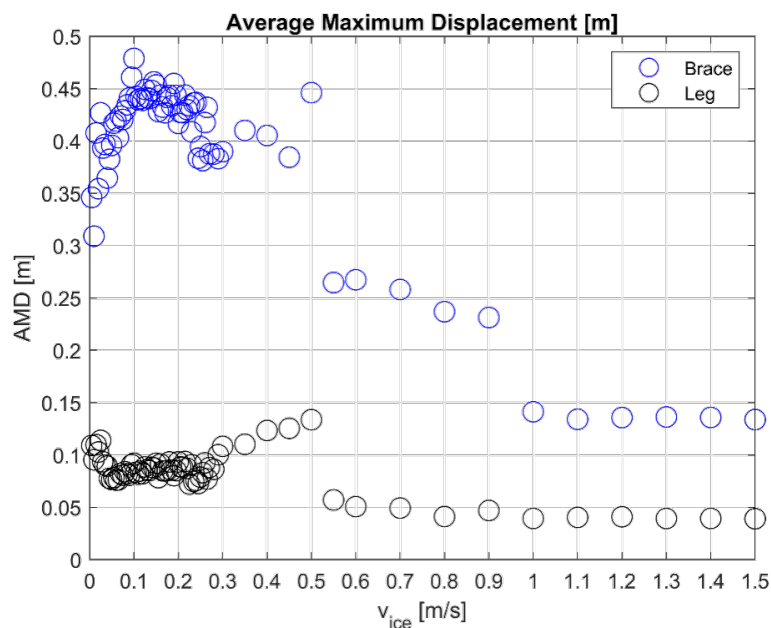


Figure 5-12: AMD of jacket with stiff legs and flexible braces

Now IC could be identified in the braces and for ice velocities higher than observed in the Baltic Sea, CBR could be identified. Local brace FLI could not be identified. Despite the stiff legs, FLI did build up in the global motion between $v_{ice} = 0.3 - 0.5$ [m/s]. This could have an influence on the build up of local FLI in the braces or even prevent it from developing.

Therefore, to further assess whether sustained local FLI could build up in the braces, a second case study was performed, now applying crushing ice load with varying ice thicknesses to a structural model only representing the x-bracing (Fig.5-13). The outer nodes of the structural model are clamped to completely eliminate the influence of the global motion. The natural frequency of the brace was varied between 4.3 and 15 [Hz], achieved by either having the wall

thickness reduced by a factor 8 or the yield strength reduced by a factor 2, in comparison to the structural properties of the Type 2 jacket. The AMD results are shown in Fig.5-13, where the different combinations of wall thickness, yield strength and ice thickness analysed are shown in the legend. Again, only IC could be identified for low ice velocities (< 0.1 [m/s]) and CBR for higher ice velocities.

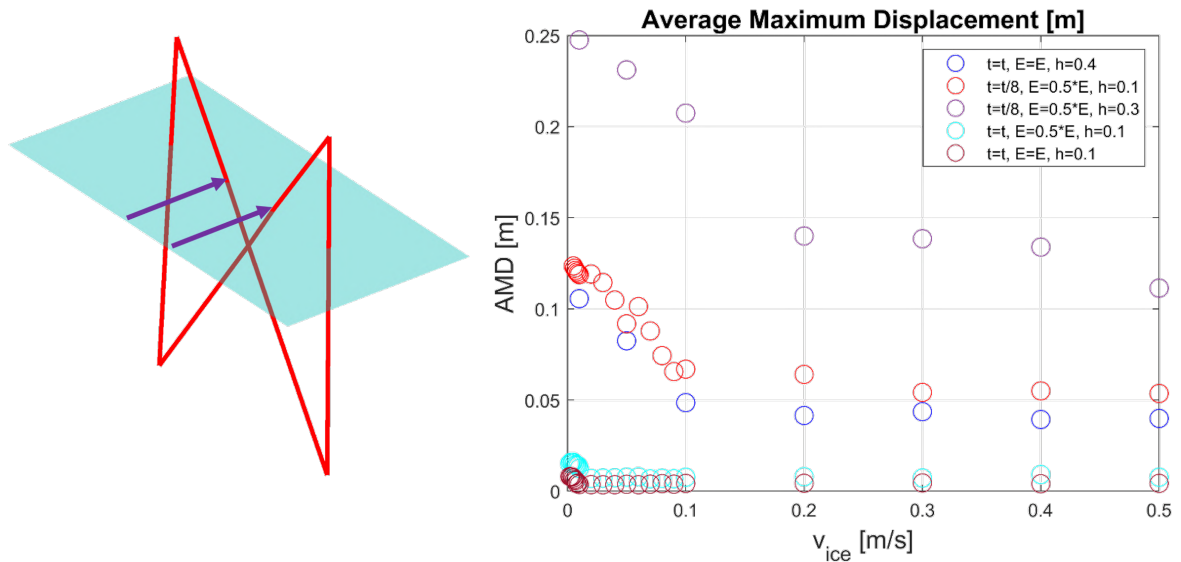


Figure 5-13: AMD of x-brace only for different structural properties

To conclude on the local FLI in the original Type 2 jacket, it appears that the global motion of the jacket causes the dragging of the brace through the ice, thereby initiating the local FLI. If one removes the influence of the global motion, as was done in the case studies, no brace is dragged through the ice which keeps the initial relative velocity between brace and ice too low in order to develop local FLI. Increasing the relative velocity by applying crushing ice with a constant high ice velocity does not induce local FLI as the velocity then remains too high. In local FLI, only the initial relative velocity is high, whereas after that the velocity corresponds to the FLI profile, which is not a constant velocity.

5-4 Base shear

In the previous sections the dynamic response of the jacket nodes have been investigated, which are useful in further research when FLS analyses are performed. Next sections will consider the static ULS loading on the jacket, starting with the assessment of the total base shear in this section.

What is clear is that the contribution to the total horizontal force is much higher for crushing ice than for bending ice (Section 4-3-2). This holds for all ice velocities. To find the worst case situation for the base shear, it needs to be defined in which situation the most crushing is occurring. The model presented in Chapter 3 and the results in Fig.3-5 can be used to find this situation. In this figure it is clear that for ice approach angles of 11-34 and 56-79 [deg], the most crushing is occurring and when the ranges 11-18 and 72-79 [deg] are considered, crushing is accompanied by the most bending failure. Therefore, a value for θ of 15 [deg] can be assumed to find the worst case situation for the base shear. In this situation there are three legs and two braces loaded by crushing ice, two braces by downward bending ice and two braces by upward bending ice (Fig.5-14).

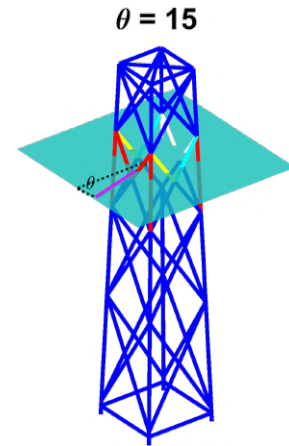


Figure 5-14: Worst case situation for $\theta = 15$ [deg]

The contributions of all the bending and crushing ice forces on all loaded elements are added together to find the total base shear value. It was found that for an ice velocity of 0.01 [m/s] the peak base shear force is maximum, with a magnitude of ≈ 6 [MN].

In order to say something about this magnitude, the total base shear due to wave loading was computed to have a comparison value. To calculate the hydrodynamic actions on the slender members in the jacket, the Morison equation is used (Vugts, 2013). The equation reads:

$$F_{mor} = f_d + f_i = \frac{1}{2}\rho_w C_d D u |u| + \frac{\pi}{4}\rho_w C_m D^2 \dot{u} \quad (5.4)$$

Where:

f_d	Hydrodynamic drag action per unit length	[N/m]
f_i	Hydrodynamic inertia action per unit length	[N/m]
ρ_w	Seawater density	[kg/m ³]
C_d	Hydrodynamic drag coefficient	[-]
C_m	Hydrodynamic inertia coefficient	[-]
D	Cylinder diameter	[m]
u	Horizontal water particle velocity in the wave	[m/s]
\dot{u}	Horizontal water particle acceleration in the wave	[m/s ²]

Determining the hydrodynamic load on each individual member using the Morison equation is cumbersome. Therefore, an equivalent stick model (Sliggers, 2019) was constructed representing the Type 2 jacket as a simple pile to reduce the difficulty in using the Morison equation, illustrated in Fig.5-15.

It was found that for wave properties in the Baltic Sea (Lindgren et al., 2020), assuming linear Airy wave theory (Airy, 1845) and a linear load distribution (for simplicity), the maximum base shear would also have a value of ≈ 6 [MN]. Thus, the base shear is of the same order of magnitude considering ice loading and wave loading, which makes that ice loading is not of particular severity for the base shear. However, in terms of overturning moment the ice loading case is more severe. This is because in contrast to wave loading, all the ice load is applied at the top of the jacket, resulting in a larger moment arm. Thus, although the maximum base shear due to ice and wave loading is found to be comparable, this is not the case for the overturning moment. The overturning moment is not assessed here and should be investigated in further research.

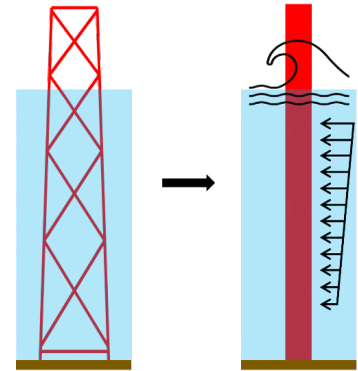


Figure 5-15: Equivalent stick model

5-5 ULS brace load

Another difference between wave loading and ice loading is that for ice loading only a few members are loaded, whereas in wave loading a large part of the structure is loaded. Therefore, it is important to assess whether a single brace will be able to withstand the load so that it will not be plastically deformed by the ice. In order to analyse this situation, the ULS brace load was assessed. First, to simplify the problem, a single brace was extracted from the jacket and represented by a simply supported beam, as illustrated in Fig.5-16. Assuming a simply supported beam will result in the highest internal moment because the boundaries can not carry any moment. As a result, the full load has to be covered by the beam itself. The internal moment in the beam can then be calculated by Eq.5.5, which is maximum when the length of a [m] is assumed equal to the length of b [m]. Then, when the appropriate parameters for P [N] and L [m] are inserted a maximum internal moment, M_{max} [Nm], can be found. Since the load P [N] is a function of ice velocity, the maximum internal moment is also dependent of ice velocity.

$$M_{max} = \frac{Pab}{L} \rightarrow \frac{PL}{4} \quad (5.5)$$

According to the International standard for fixed steel offshore structures (ISO 19902, 2007), tubular members subjected to bending moments must be designed to satisfy the condition stated in Eq.5.6.

$$\sigma_b = \frac{M}{Z_e} \leq \frac{f_b}{\gamma_{R,b}} \quad (5.6)$$

Where:

σ_b	Bending stress	[Pa]
M	Internal bending moment	[Nm]
Z_e	Elastic section modulus, $Z_e = \frac{\pi}{64} (D^4 - (D - 2t)^4) / (\frac{D}{2})$	[m ³]
t	Wall thickness	[m]
f_b	Representative bending strength	[Pa]
$\gamma_{R,b}$	Partial resistance factor for bending strength, $\gamma_{R,b} = 1.05$	[-]

The value for f_b is dependent of the structural properties and should be calculated according to the design code. Since the internal bending moment is dependent of ice velocity, the utilisation as defined in Eq.5.7 can be calculated as function of ice velocity, of which the result is plotted in Fig.5-17. Here it can be seen that for low ice velocities, in the IC regime, the utilisation is close to unity. A utilisation value below unity is considered safe enough, which makes the Type 2 design suitable in sub-arctic waters, but it indicates that brace utilisation should be carefully assessed when other jacket designs are investigated. Note that the assumptions made here overestimate the maximum internal bending moment. In reality, the welds in the structural nodes are capable of carrying moment, reducing the maximum moment in the brace. On top of that, the x-brace is supported in the middle by another brace, which in turn reduces the maximum internal moment.

$$U_m = \frac{\sigma_b}{f_b/\gamma_{R,b}} = \frac{M/Z_e}{f_b/\gamma_{R,b}} \quad (5.7)$$

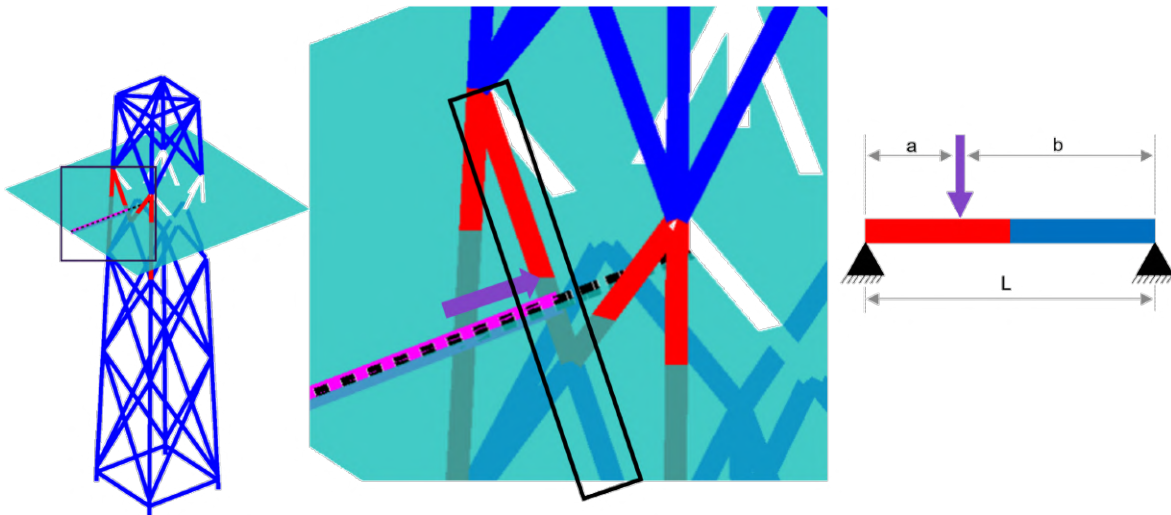


Figure 5-16: ULS brace load simplification

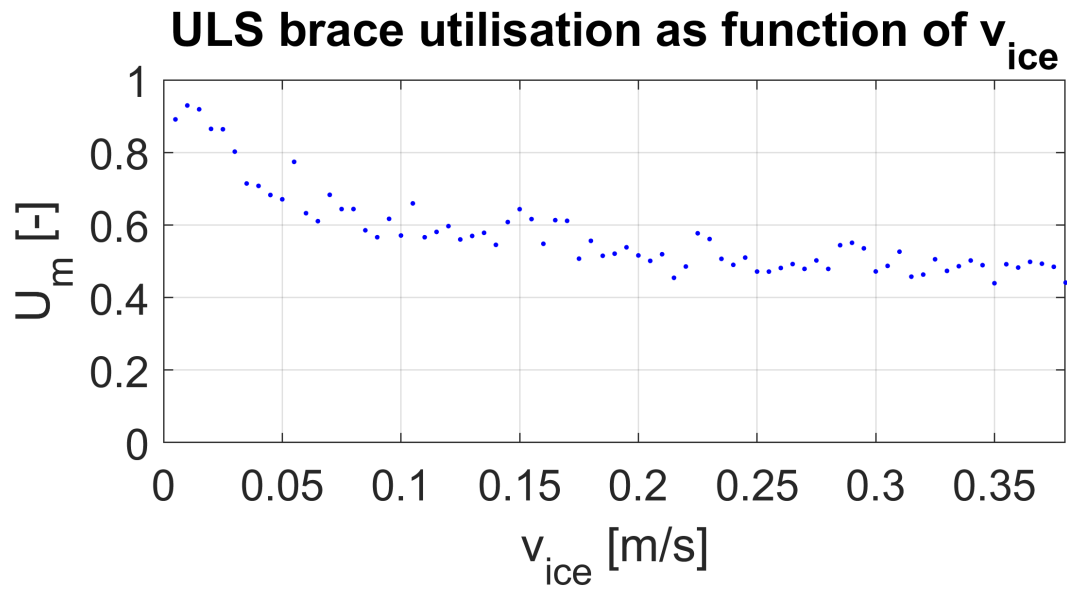


Figure 5-17: Brace utilisation as function of ice velocity

Part II

Dynamic substructuring in modelling ice-structure interaction

6

Dynamic substructuring

In the previous chapters the dynamic behaviour of a jacket structure due to ice loading has been investigated and several numerical models have been utilised to simulate the dynamics. A full finite element model is used to represent the full structure, that is, the jacket attached to a tower with a lumped RNA mass on top. This chapter will consider a Type 1 jacket, since it is a bit more simple to explain the concept of dynamic substructuring having a structure with less loaded nodes.

The full model of the Type 1 jacket consists of 61 nodes, having a total of 366 degrees of freedom (DoFs), because each node of a 3D beam model has 6 DoFs. Soil stiffness is not taken into account meaning that the four fixed bottom nodes of the legs will be constrained at seabed level. Removing the 24 DoFs representing these nodes results in 342 free DoFs, meaning that the model has 342 eigenmodes. Solving the dynamics taking into account all eigenmodes is computationally expensive. One solution is to apply modal analysis. In this way only a selection of all modes is taken into account, truncating the higher frequency modes, still leading to sufficiently accurate results. Usually the higher modes are unreliable anyway because of the unknown damping in the system. Performing computations in the modal domain is computationally preferred. However, in complex structures it is convenient to split the structure into smaller substructures. In this way the dynamics of the particular substructure can be better investigated allowing for local optimisation of the design. On top of that, model simplification can be used by eliminating local subsystem behaviour which is of no influence to the assembled system. However, different (modally reduced) substructures have to be assembled to a complete system to analyse the complete dynamics. This coupling can be done using the Craig-Bampton method, which will be explained hereafter.

6-1 The Craig-Bampton method

The Craig-Bampton method (Craig and Bampton, 1968) is a reduction method without coarsening the mesh. In other words, leaving out nodes would be coarsening the mesh, hence making the structure stiffer and leading to unreliable results (Van der Valk, 2014a). Reduction methods without coarsening the mesh are known as *component model reduction methods*. In fact it works the same as modal superposition (Section 4-3-2), only the modes are associated with boundary nodes and internal nodes.

To explain the theory of the Craig-Bampton method, consider a stand-alone jacket model and a stand-alone tower-RNA model. Typically only the jacket is reduced using the Craig-Bampton method, hence from now on referred to as *superelement*. In practice, each part is designed by a different party. The jacket is designed by the foundation designer, whereas the tower-RNA assembly is designed by SGRE, after which load calculations need to be performed on the integrated system. For both parties it is desired to be able to model the full system, without having to provide the full details of the design to the other party. The superelement is modally truncated in a way similar to modal analysis, only the advantage of the Craig-Bampton method is that it makes it possible to couple different superelements to other structural models, without the need to share the details of the design. This is not possible with modal analysis, where it would be necessary to combine the full subsystems with each other, after which modal truncation could be done.

Consider the system of equations of motion for the jacket (without damping):

$$\mathbf{M}\ddot{\mathbf{u}}(t) + \mathbf{K}\mathbf{u}(t) = \mathbf{f}(t) \quad (6.1)$$

Here \mathbf{M} is the mass matrix, \mathbf{K} is the stiffness matrix, \mathbf{u} is the vector of DoFs and \mathbf{f} is the external force vector. Next step is to split the DoFs into boundary DoFs (b) and internal DoFs (i). Note that the time dependency (t) is omitted here for ease of reading.

$$\begin{bmatrix} \mathbf{M}_{bb} & \mathbf{M}_{bi} \\ \mathbf{M}_{ib} & \mathbf{M}_{ii} \end{bmatrix} \begin{bmatrix} \ddot{\mathbf{u}}_b \\ \ddot{\mathbf{u}}_i \end{bmatrix} + \begin{bmatrix} \mathbf{K}_{bb} & \mathbf{K}_{bi} \\ \mathbf{K}_{ib} & \mathbf{K}_{ii} \end{bmatrix} \begin{bmatrix} \mathbf{u}_b \\ \mathbf{u}_i \end{bmatrix} = \begin{bmatrix} \mathbf{f}_b \\ \mathbf{f}_i \end{bmatrix} \quad (6.2)$$

In the case of the jacket, the boundary DoFs are associated to the interface node, where the tower bottom will be attached to. The internal DoFs are all other DoFs in the jacket (Fig.6-1).

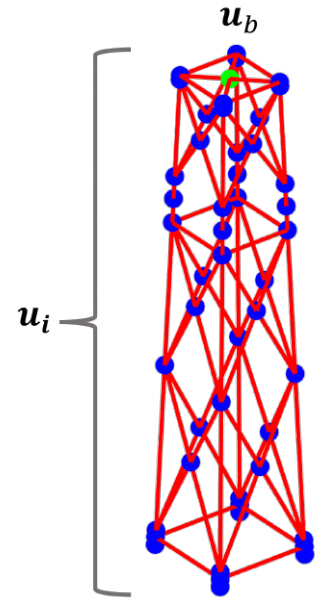


Figure 6-1: Jacket nodes divided in boundary nodes and internal nodes

The objective is to retain the boundary DoFs to ensure coupling through the interface between jacket and tower and also describe the dynamics of the internal DoFs correctly. This is done by assuming that the response of the internal DoFs can be captured by a static and a dynamic part:

$$\mathbf{u}_i = \mathbf{u}_{i,stat} + \mathbf{u}_{i,dyn} \quad (6.3)$$

Applying a unit displacement at the boundary node and then solving the equation of motion yields the Constraint modes Ψ_C , also known as Guyan reduction modes (Guyan, 1965). The constraint modes can be found by solving Eq.6.4. Here it is assumed that no external force is applied to the internal DoFs.

$$\mathbf{u}_{i,stat} = -\mathbf{K}_{ii}^{-1} \mathbf{K}_{ib} \mathbf{u}_b = \Psi_C \mathbf{u}_b \quad (6.4)$$

To find an approximation for the dynamic part of the response, the modal superposition principle is used. The internal vibration modes Φ are computed by fixing the boundary node and then solving the eigenvalue problem:

$$(\mathbf{K}_{ii} - \omega_i^2 \mathbf{M}_{ii}) \phi_i = \mathbf{0} \quad (6.5)$$

To actually reduce or truncate the problem, only the first mode shapes ϕ_i are retained. First, it is investigated what the maximum frequency of interest is, because it is important that the reduced system can still capture that frequency. In practice around 20-25 vibrational modes are included in the reduced system. Combining the constraint modes and the fixed interface vibration modes is what defines the Craig-Bampton method. The internal DoFs can therefore be approximated by:

$$\mathbf{u}_i = \Psi_C \mathbf{u}_b + \Phi_i \boldsymbol{\eta}_i \quad (6.6)$$

Here $\boldsymbol{\eta}_i$ are the modal amplitudes of the internal modes. In matrix format Eq.6.6 looks like:

$$\begin{bmatrix} \mathbf{u}_b \\ \mathbf{u}_i \end{bmatrix} = \begin{bmatrix} \mathbf{u}_b \\ \Psi_C \mathbf{u}_b + \Phi_i \boldsymbol{\eta}_i \end{bmatrix} = \begin{bmatrix} \mathbf{I} & \mathbf{0} \\ \Psi_C & \Phi_i \end{bmatrix} \begin{bmatrix} \mathbf{u}_b \\ \boldsymbol{\eta}_i \end{bmatrix} = \mathbf{R} \mathbf{q} \quad (6.7)$$

The vector of DoFs \mathbf{u} can thus be described by $\mathbf{u} = \mathbf{R} \mathbf{q}$, where \mathbf{R} is the reduction matrix, consisting of constraint modes Ψ_C and vibrational modes Φ . Upon substitution the original system of equations of motion for the jacket in Eq.6.1 can be written as:

$$\mathbf{M}\mathbf{R}\ddot{\mathbf{q}} + \mathbf{K}\mathbf{R}\mathbf{q} = \mathbf{f} + \mathbf{r} \quad (6.8)$$

A residual force \mathbf{r} is present because the accuracy of the reduced model is always less than the full model so an error will exist. This error is however by definition orthogonal to the space of eigenmodes used in the reduction matrix \mathbf{R} and can therefore be eliminated by pre-multiplying the equation with \mathbf{R}^T :

$$\begin{aligned} \mathbf{R}^T \mathbf{M}\mathbf{R}\ddot{\mathbf{q}} + \mathbf{R}^T \mathbf{K}\mathbf{R}\mathbf{q} &= \mathbf{R}^T \mathbf{f} + \mathbf{R}^T \mathbf{r} \\ \tilde{\mathbf{M}}\ddot{\mathbf{q}} + \tilde{\mathbf{K}}\mathbf{q} &= \tilde{\mathbf{f}} \end{aligned} \quad (6.9)$$

Now the original set of equations of motion have been reduced by making use of the reduction matrix \mathbf{R} . Since the interface DoFs are retained, this reduced model can be assembled to other components. These components can still contain all modes or can also be reduced through the same procedure. The possibility to couple these reduced components makes them referred to as *superelements* (Van der Valk, 2014a).

6-2 Assembly of (super)elements

In the previous section a superelement was created from a jacket model. The eventual objective is to perform time domain simulations with an integrated system consisting of a jacket, tower and RNA. Therefore, the jacket superelement needs to be assembled to the tower-RNA assembly. This section will explain the procedure of assembly.

The jacket superelement and the tower-RNA assembly are coupled through the interface node (top of the jacket, bottom of the tower). Combining the equations of motion of both components yields:

$$\begin{bmatrix} \mathbf{M}^{(W)} & 0 \\ 0 & \tilde{\mathbf{M}}^{(J)} \end{bmatrix} \begin{bmatrix} \ddot{\mathbf{u}}^{(W)} \\ \ddot{\mathbf{q}}^{(J)} \end{bmatrix} + \begin{bmatrix} \mathbf{K}^{(W)} & 0 \\ 0 & \tilde{\mathbf{K}}^{(J)} \end{bmatrix} \begin{bmatrix} \mathbf{u}^{(W)} \\ \mathbf{q}^{(J)} \end{bmatrix} = \begin{bmatrix} \mathbf{f}_{wind} \\ \tilde{\mathbf{f}}_{wave/ice} \end{bmatrix} + \begin{bmatrix} \mathbf{g}^{(W)} \\ \mathbf{g}^{(J)} \end{bmatrix} \quad (6.10)$$

The superscript $^{(W)}$ indicates the tower-RNA assembly and $^{(J)}$ indicates the jacket model. Again damping is neglected here for simplicity, but will be discussed in Section 6-5-1. The force vector \mathbf{g} indicates the interface forces that the jacket 'feels' from the tower-RNA assembly (Voormeeren et al., 2011). This force vector is therefore only non-zero at the coupling DoFs. The connection forces \mathbf{g} are unknown however, making it impossible to solve the system. Also, the equations are not yet coupled. In order to solve the system in a coupled way, two different assembly conditions are introduced (De Klerk et al., 2008):

1. **Compatibility:** The displacements at the interface DoFs must be equal. This can be expressed as:

$$[\mathbf{B}^{(W)} \quad \mathbf{B}^{(J)}] \begin{bmatrix} \mathbf{u}^{(W)} \\ \mathbf{q}^{(J)} \end{bmatrix} = \mathbf{0} \quad (6.11)$$

2. **Equilibrium:** The connection forces must be equal and opposite in direction. This can be expressed as:

$$[\mathbf{L}^{(W)T} \quad \mathbf{L}^{(J)T}] \begin{bmatrix} \mathbf{g}^{(W)} \\ \mathbf{g}^{(J)} \end{bmatrix} = \mathbf{0} \quad (6.12)$$

The matrices \mathbf{B} are signed Boolean matrices indicating the location of the interface DoFs. The matrices \mathbf{L} are Boolean localization matrices, localizing the unique DoFs from the total set of DoFs. It can be shown mathematically that the matrices \mathbf{B} and \mathbf{L} are in each other's nullspace. Constructing \mathbf{B} is straightforward (Section 6-4), hence \mathbf{L} can be computed easily by executing $\mathbf{L} = \text{null}(\mathbf{B})$ in MATLAB for example.

$$[\mathbf{B}^{(W)} \quad \mathbf{B}^{(J)}] \begin{bmatrix} \mathbf{L}^{(W)} \\ \mathbf{L}^{(J)} \end{bmatrix} = \mathbf{0} \quad (6.13)$$

Combining the assembly conditions (Eq.6.11 and Eq.6.12) with the combined equations of motion of the jacket superelement and tower-RNA assembly in Eq.6.10 yields a coupled set of equations to be solved. However, solving three sets of equations simultaneously is cumbersome. In practice the equation can be more compact by performing a simplification. Two different methods exist being the so-called *primal* and *dual* assembly. The *primal* assembly procedure is almost always applied in practice due to its simplicity. Moreover, it was found doing the calculations for this thesis that in terms of computational time, the *primal* assembly procedure is approximately two times faster than the *dual* assembly procedure. However, the use of interface force data is more clear using the *dual* assembly procedure. Therefore, both procedures will be discussed.

6-2-1 Primal assembly

In the primal assembly method, the compatibility condition is satisfied a priori (Voormeeren et al., 2011). In order to satisfy compatibility, a unique set of interface displacement DoFs \mathbf{u}_γ is defined. Realizing that compatibility has to be enforced between the substructure boundary DoFs and these unique set of interface displacements, a simple substitution based on Eq.6.11 and Eq.6.13 can be done:

$$\mathbf{u}_b = \mathbf{L}_b \mathbf{u}_\gamma \quad (6.14)$$

Adding a second equation to enforce interface force equilibrium, results in the following coupled system of equations:

$$\begin{cases} \mathbf{M}\mathbf{L}\ddot{\mathbf{u}}_\gamma + \mathbf{C}\mathbf{L}\dot{\mathbf{u}}_\gamma + \mathbf{K}\mathbf{L}\mathbf{u}_\gamma = \mathbf{f} + \mathbf{g} \\ \mathbf{L}^T \mathbf{g} = \mathbf{0} \end{cases} \quad (6.15)$$

Pre-multiplying by \mathbf{L}^T will still satisfy both conditions and noting that $\mathbf{L}^T \mathbf{g} = \mathbf{0}$, results in:

$$\tilde{\mathbf{M}}\ddot{\mathbf{u}}_\gamma + \tilde{\mathbf{C}}\dot{\mathbf{u}}_\gamma + \tilde{\mathbf{K}}\mathbf{u}_\gamma = \mathbf{L}^T \begin{cases} \tilde{\mathbf{M}} = \mathbf{L}^T \mathbf{M} \mathbf{L} \\ \tilde{\mathbf{C}} = \mathbf{L}^T \mathbf{C} \mathbf{L} \\ \tilde{\mathbf{K}} = \mathbf{L}^T \mathbf{K} \mathbf{L} \end{cases} \quad (6.16)$$

Note that in Eq.6.15 and Eq.6.16 matrices \mathbf{M} , \mathbf{C} and \mathbf{K} are the block-diagonal matrices formed by the individual matrices from the jacket superelement and tower-RNA assembly (De Klerk et al., 2008):

$$\mathbf{M} = \text{diag}(\mathbf{M}^{(W)}, \mathbf{M}^{(J)}), \mathbf{C} = \text{diag}(\mathbf{C}^{(W)}, \mathbf{C}^{(J)}), \mathbf{K} = \text{diag}(\mathbf{K}^{(W)}, \mathbf{K}^{(J)}) \quad (6.17)$$

This system can be solved by using time stepping algorithms, for example *Newmark implicit linear* (Newmark, 1959) explained in Appendix C, described relating to Craig-Bampton reduced systems by Gruber et al. (2017) or by built-in variable time stepping algorithms like ODE45 in MATLAB.

6-2-2 Dual assembly

In the dual assembly method, the equilibrium condition is satisfied a priori, while including the compatibility condition in the equations to be solved (De Klerk et al., 2008). The interface forces are then expressed as:

$$\begin{bmatrix} \mathbf{g}^{(W)} \\ \mathbf{g}^{(J)} \end{bmatrix} = - \begin{bmatrix} \mathbf{B}^{(W)T} \\ \mathbf{B}^{(J)T} \end{bmatrix} \boldsymbol{\lambda} \quad (6.18)$$

The vector $\boldsymbol{\lambda}$ represents the interface forces. The length of the vector is equal to the number of DoFs of the boundary nodes. In this case the jacket and the tower-RNA assembly will be coupled through one interface node, hence the length of $\boldsymbol{\lambda}$ will be 6.

When the expression in Eq.6.18 is substituted in Eq.6.10 and combined into a single set of equations, the "dual assembled" equations of motion are:

$$\begin{bmatrix} \mathbf{M}^{(W)} & 0 & 0 \\ 0 & \tilde{\mathbf{M}}^{(J)} & 0 \\ 0 & 0 & 0 \end{bmatrix} \begin{bmatrix} \ddot{\mathbf{u}}^{(W)} \\ \ddot{\mathbf{q}}^{(J)} \\ \ddot{\boldsymbol{\lambda}} \end{bmatrix} + \begin{bmatrix} \mathbf{K}^{(W)} & 0 & \mathbf{B}^{(W)T} \\ 0 & \tilde{\mathbf{K}}^{(J)} & \mathbf{B}^{(J)T} \\ \mathbf{B}^{(W)} & \mathbf{B}^{(J)} & 0 \end{bmatrix} \begin{bmatrix} \mathbf{u}^{(W)} \\ \mathbf{q}^{(J)} \\ \boldsymbol{\lambda} \end{bmatrix} = \begin{bmatrix} \mathbf{f}_{wind} \\ \tilde{\mathbf{f}}_{wave/ice} \\ \mathbf{0} \end{bmatrix} \quad (6.19)$$

With the integrated model from Eq.6.19 time domain simulations can be performed. Again the *Newmark implicit linear* method (Newmark, 1959)(Appendix C) can be used to solve the system. The output of the simulation when damping is taken into account too consists of:

$$\begin{array}{ll} \text{Tower-RNA assembly:} & \ddot{\mathbf{u}}^{(W)}, \dot{\mathbf{u}}^{(W)}, \mathbf{u}^{(W)} \\ \text{Jacket:} & \ddot{\mathbf{q}}^{(J)}, \dot{\mathbf{q}}^{(J)}, \mathbf{q}^{(J)} \\ \text{Interface forces:} & \boldsymbol{\lambda} \end{array}$$

6-3 Dynamic post-processing

In practice, the integrated system as described in the previous section is solved by SGRE. The interface load time series $\boldsymbol{\lambda}$ are then supplied by SGRE to the foundation designer. Using the interface force time series, the dynamic response of the jacket can be reconstructed by the foundation designer by applying these interface forces as an additional external force to the jacket and then solve for the response:

$$\tilde{\mathbf{M}}^{(J)} \ddot{\mathbf{q}}^{(J)} + \tilde{\mathbf{K}}^{(J)} \mathbf{q}^{(J)} = \tilde{\mathbf{f}}_{wave/ice} - \mathbf{B}^{(J)T} \boldsymbol{\lambda} \quad (6.20)$$

This is equivalent to solving the second row in Eq.6.19. The response is therefore computed correctly. Thus, by using only these interface forces it is possible for the foundation designer to model the dynamics of the jacket structure as if it were connected to the tower-RNA assembly. However, usually the foundation designer applies these interface forces to the full jacket model instead of the reduced one. The system then becomes:

$$\mathbf{M}^{(J)} \ddot{\mathbf{u}}^{(J)} + \mathbf{K}^{(J)} \mathbf{u}^{(J)} = \mathbf{f}_{wave/ice} - \mathbf{B}_{full}^{(J)T} \boldsymbol{\lambda} \quad (6.21)$$

There will be a slight difference between the output $\mathbf{q}^{(J)}$ and $\mathbf{u}^{(J)}$. However, if the superelement model is properly constructed, the difference will be negligible.

6-4 Constructing signed Boolean matrices B

To illustrate the construction of Boolean matrices B and L , consider the system shown in Fig.6-2. Substructure A consists of 5 nodes with 8 DoFs in total. Substructure B consists of 3 nodes with 4 DoFs in total. In this example, node 5 and node 6 will be coupled. In order to do that, two compatibility conditions must be satisfied:

$$\begin{cases} u_{5x} = u_{6x} \\ u_{5y} = u_{6y} \end{cases} \quad (6.22)$$

The total vector of degrees of freedom is:

$$\mathbf{u} = [u_{1x} \quad u_{2x} \quad u_{3x} \quad u_{3y} \quad u_{4x} \quad u_{4y} \quad u_{5x} \quad u_{5y} \quad u_{6x} \quad u_{6y} \quad u_{7x} \quad u_{8x}] \quad (6.23)$$

To express the compatibility condition as in Eq.6.11, the signed Boolean matrix B must be:

$$B = \begin{bmatrix} 0 & 0 & 0 & 0 & 0 & 0 & 1 & 0 & -1 & 0 & 0 & 0 \\ 0 & 0 & 0 & 0 & 0 & 0 & 0 & 1 & 0 & -1 & 0 & 0 \end{bmatrix} \quad (6.24)$$

In case substructure A is reduced, the DoFs are localized differently than initially. Constructing a reduced system will be done through reduction matrix R :

$$\mathbf{u} = \begin{bmatrix} \mathbf{I} & \mathbf{0} \\ \Psi_C & \Phi_i \end{bmatrix} \begin{bmatrix} \mathbf{u}_b \\ \boldsymbol{\eta}_i \end{bmatrix} = \mathbf{R}\mathbf{q} \quad (6.25)$$

This means that the first two columns in the reduction matrix R will represent the static modes, associated to the boundary DoFs. The columns right of the static modes are the internal vibration modes, associated to the free DoFs. This makes that the Boolean matrix has to be constructed slightly different:

$$B = \begin{bmatrix} 1 & 0 & \dots & -1 & 0 & 0 & 0 \\ 0 & 1 & \dots & 0 & -1 & 0 & 0 \end{bmatrix} \quad (6.26)$$

Where "... " are x columns of zeros with x equal to the number of vibration modes included in the reduced system.

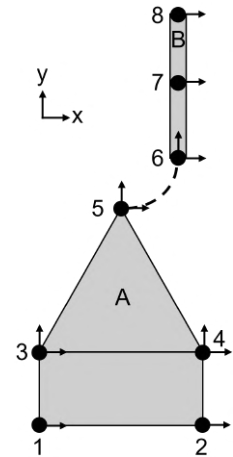


Figure 6-2:
Coupling two substructures

6-5 Rayleigh damping

The concept of the Craig-Bampton method has been explained without taking damping into account. However, assembling substructures with damping is not as straightforward as coupling the mass and stiffness matrices. First, the concept of Rayleigh damping will be discussed, as this type of damping is typically used in the industry, after which it will be explained how the correct parameters can be found for further analyses.

Consider a full integrated FEM of a jacket with a tower-RNA assembly attached. The equations of motion can be expressed by:

$$M\ddot{\mathbf{x}} + C\dot{\mathbf{x}} + K\mathbf{x} = \mathbf{f} \quad (6.27)$$

In modal analysis, the forced motion is represented as a superposition of normal modes of free undamped vibrations multiplied by unknown functions in time:

$$\mathbf{x}(t) = \Phi \mathbf{u}(t) \quad (6.28)$$

Substituting this assumption into the equations of motion and premultiplying by the matrix of eigenmodes Φ yields:

$$M^* \ddot{\mathbf{u}} + C^* \dot{\mathbf{u}} + K^* \mathbf{u} = \Phi^T \mathbf{f} \quad (6.29)$$

Where $M^* = \Phi^T M \Phi$, $C^* = \Phi^T C \Phi$, $K^* = \Phi^T K \Phi$.

Multiplying these equations of motion with the inverse of the modal mass matrix M^* :

$$\ddot{u}_i + \frac{c_{ii}^*}{m_{ii}^*} \dot{u}_i + \omega_i^2 u_i = \frac{F_i^*(t)}{m_{ii}^*} \quad (6.30)$$

It is then possible to introduce the Modal Damping Ratio ξ_i (Metrikine, 2020):

$$\xi_i = \frac{c_{ii}^*}{c_{ii}^{crit}} = \frac{c_{ii}^*}{2\sqrt{k_{ii}^* m_{ii}^*}} = \frac{c_{ii}^*}{2m_{ii}^* \omega_i} \quad (6.31)$$

Where c_{ii}^{crit} is the critical damping. Using this, Eq.6.30 can be rewritten to:

$$\ddot{u}_i + 2\xi_i \omega_i \dot{u}_i + \omega_i^2 u_i = \frac{F_i^*(t)}{m_{ii}^*} \quad (6.32)$$

This equation has a general solution and can be solved. However, all this is based upon the assumption that the Modal Damping Matrix is diagonal, which is usually not the case. This prevents the possibility to decouple the equations of motion, which means modal analysis can not be executed (Metrikine, 2020). To overcome this issue, the damping of the system can be constructed by assuming Proportional Rayleigh Damping (PRD), which is defined as follows:

$$\mathbf{C} = a\mathbf{M} + b\mathbf{K} \quad (6.33)$$

Where a and b are unknown constants. The PRD assumes damping can be constructed by assuming it to be a linear combination of mass and stiffness. Therefore, the modal damping takes the form:

$$\mathbf{C}^* = \Phi^T \mathbf{C} \Phi = \Phi^T (a\mathbf{M} + b\mathbf{K}) \Phi = a\Phi^T \mathbf{M} \Phi + b\Phi^T \mathbf{K} \Phi = a\mathbf{M}^* + b\mathbf{K}^* \quad (6.34)$$

In this way the damping matrix \mathbf{C}^* will be diagonal (\mathbf{M}^* and \mathbf{K}^* are also diagonal because of modal decoupling), which allows for the decoupling of the total set of equations of motion, after which modal analysis can be performed. The modal damping ratio takes the form:

$$\xi_i = \frac{c_{ii}^*}{2m_{ii}^*\omega_i} = \frac{am_{ii}^* + bk_{ii}^*}{2m_{ii}^*\omega_i} = \frac{a}{2\omega_i} + \frac{b\omega_i}{2} \quad (6.35)$$

To determine a and b , it is possible to assume that the modal damping ratios (ξ_i) for the first two modes are known. Solving for a and b leads to:

$$a = \frac{2\omega_1\omega_2(\xi_1\omega_2 - \xi_2\omega_1)}{\omega_2^2 - \omega_1^2}, \quad b = \frac{2(\xi_2\omega_2 - \xi_1\omega_1)}{\omega_2^2 - \omega_1^2} \quad (6.36)$$

In this thesis the full model consisting of a jacket and a tower-RNA assembly was modelled with both modal damping ratios set to $\xi_1 = \xi_2 = 0.01$. This value implies that the structural damping in the complete system is 1% of critical. This lead to values for a and b of 0.0305 and 0.0022, respectively. These values are dependent of the first two natural frequencies of the system, ω_1 and ω_2 . When considering the jacket superelement and the tower-RNA assembly, the natural frequencies of these systems naturally differ from the total assembled system:

Component	ω_1 [Hz]	ω_2 [Hz]
Full coupled model	0.307	1.161
Jacket superelement	1.136	2.258
Tower-RNA assembly	3.702	12.015

Which implies that setting $\xi_1 = \xi_2 = 0.01$ for the jacket superelement and also for the tower-RNA assembly and assembling the two will *not* lead to the same a and b values of the full system, leading to a different overall damping matrix \mathbf{C} . Therefore, ξ_1 and ξ_2 of both superelements have to be tuned so that the eventual assembly of both superelements has the same proportional damping as the full system.

6-5-1 Tuning of Rayleigh damping parameters $\xi_{i,j}$

Since there are two structures considered, a jacket superelement and a tower-RNA assembly, in total four modal damping ratios need to be found. These are referred to as $\xi_{i,j}$, where the subscript i indicates the first (1) or second (2) damping ratio and the subscript j indicates the jacket (j) or tower-RNA (t) component.

By assembling both substructures with help of the Boolean matrices explained in Section 6-4, it is possible to compute the values for a and b for the jacket superelement and the tower-RNA assembly, for different values of $\xi_{i,j}$. The goal is to find the damping ratios $\xi_{i,j}$ for each superelement so that the Rayleigh damping parameters a and b of each superelement match with the a and b values in the full assembled system. This is illustrated in Fig.6-3.

The horizontal planes in the top four figures represent the target damping parameters a and b of the full assembled system. The inclined planes are a result of calculating the damping parameters for different modal damping ratios. It can be seen that the intersection between the planes forms a straight line. That implies that the intersection point of these straight lines indicate the combination of modal damping ratios that will result in the correct assembled superelement damping. The intersection points are illustrated in the bottom two figures of Fig.6-3.

Now that the procedure of constructing a superelement representation of a structural assembly is known, the method can be applied to solve the coupled interaction between ice and structure. Since specific adjustments have to be made regarding this coupled problem, the details will be handled in a separate chapter, namely Chapter 7.

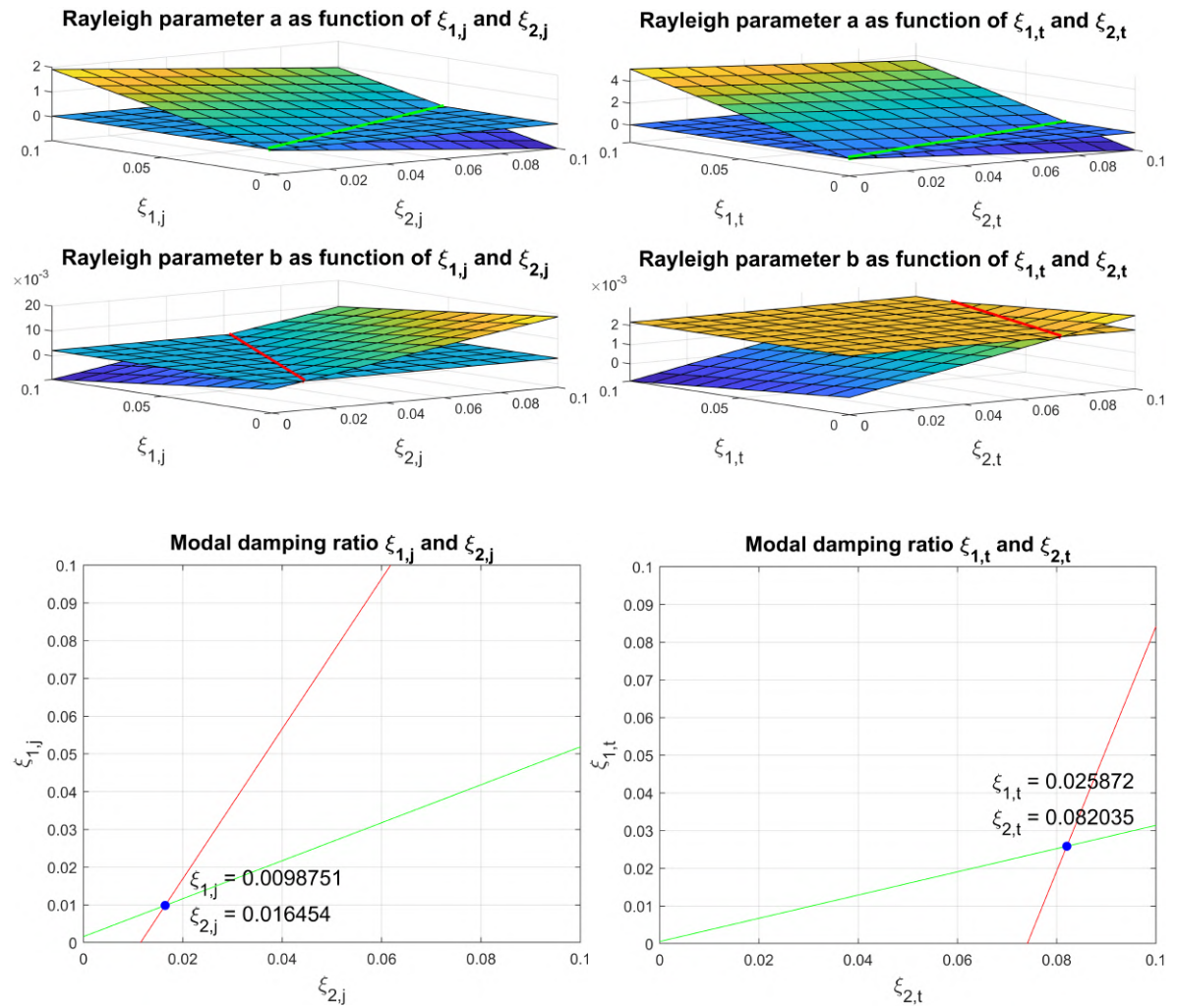


Figure 6-3: Rayleigh damping parameters a and b as function of modal damping ratio $\xi_{i,j}$



Ice models applied to the superelement representation of the structure

In Chapter 6 the dynamic substructuring method has been discussed. The Type 1 jacket has been represented by a superelement and a tower-RNA assembly has been coupled to it. This chapter will discuss how numerical simulations regarding ice-structure interaction can be performed with this superelement assembly.

The system described by Eq.6.19 can be solved easily when the force matrix is completely known. This goes for wave loading (assuming wave loads are uncoupled due to the stiff nature of the jacket) as well as loads induced by ice bending failure, described in Section 2-1. For these types of loading the forces that will be induced on the structure can be pre-calculated after which the system of equations can be solved by the Newmark method (Newmark, 1959, Gruber et al., 2017) (Appendix C). This is not as straightforward when the forces induced to the structure are coupled with the motion of the structure, because the forces can not be computed a priori but have to be computed at every timestep. This is the case for ice crushing failure, as described in Section 2-2.

Three main difficulties arise when modelling coupled interaction using a superelement model. One is that the structural equations in the 'superelement domain' and the ice equations in the spatial domain have to be solved simultaneously. Second is that by definition, using the superelement representation of a system will result in losing information about the internal nodes, all contributing to the structural response at the interface node, which could lead to inaccurate results. Third is that the ice crushing force is actually applied at the internal nodes and the force induced to the structure is dependent on the motion of these loaded nodes. Therefore, the force at the loaded nodes will not be computed correctly, since the computed displacement at the internal nodes has a slight error. This is explained in Section 7-1.

7-1 Non-reduced loaded DoFs

A problem often encountered in the field of dynamic substructuring is to properly represent forces acting at the internal DoFs of a substructure (Van der Valk, 2014b). To illustrate that, consider the following situation (Fig.7-1):

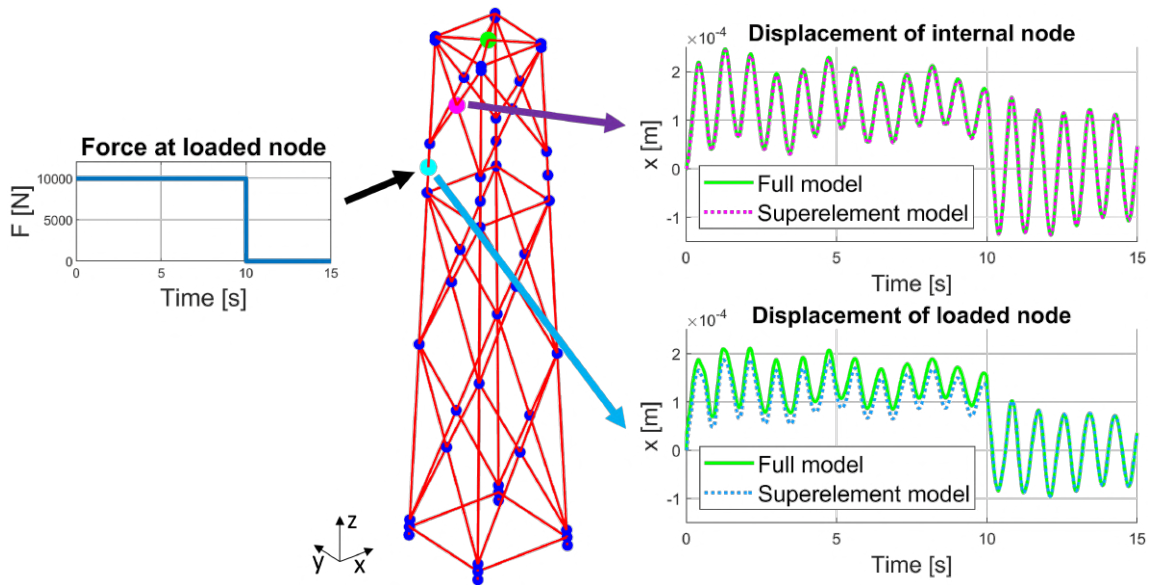


Figure 7-1: Force applied at internal node. The computed displacement of this loaded internal node is compared to the computed displacement of a non-loaded internal node

A force is applied at the cyan (●) colored node in Fig.7-1. At the green (●) node a tower-RNA assembly is attached, which is not shown in the figure. Next, the displacement at this loaded node and at a random other internal node (●) is computed. This is done using the full model as well as the superelement reduced model. When one compares the responses computed by these different modelling approaches, one can see that the superelement reduced model is capable of calculating the displacement at the (●) node correctly, but is not capable of calculating the displacement at the loaded node (●) correctly during loading.

Because of this error, it is more convenient to not include this node in the subset of internal DoFs, but instead include it in the subset of boundary DoFs. Retaining the nodes that will be loaded as boundary nodes divides the structure in u_b and u_i as seen in Fig.7-2. Applying the same force to the 'non-reduced loaded DoFs' (NRLD) structure yields the computed displacement at the (●) node shown in Fig.7-3. Now the displacement computed by the reduced model has no error in comparison to the displacement computed by the full model. This finding is fundamental in computing ice-structure interaction because the forces induced to the structure depend on the displacement of these loaded nodes. It is therefore crucial to compute the displacements of these nodes correctly.

However, if a large part of the structure is loaded, i.e. lots of DoFs are excited, it is not convenient anymore to include all these DoFs in the subset of retained DoFs. This would lead to unacceptably large reduced superelements which takes down the effectiveness of the dynamic substructuring algorithm. This is the case for wave loading, where almost the full support structure will be loaded. Several methods exist to overcome this issue, for example *spectral decomposition*, *equivalent blocked forces* or *dual blocked forces*. Reference is made to the PhD thesis by Paul van der Valk (2014a) on these methods and will not be discussed here. However, in ice loading, only a few nodes are loaded, which makes it convenient to use the NRLD approach without taking down the effectiveness of the dynamic substructuring algorithm. The methods to overcome the issue are therefore not needed regarding ice loading, which is a very valuable finding.

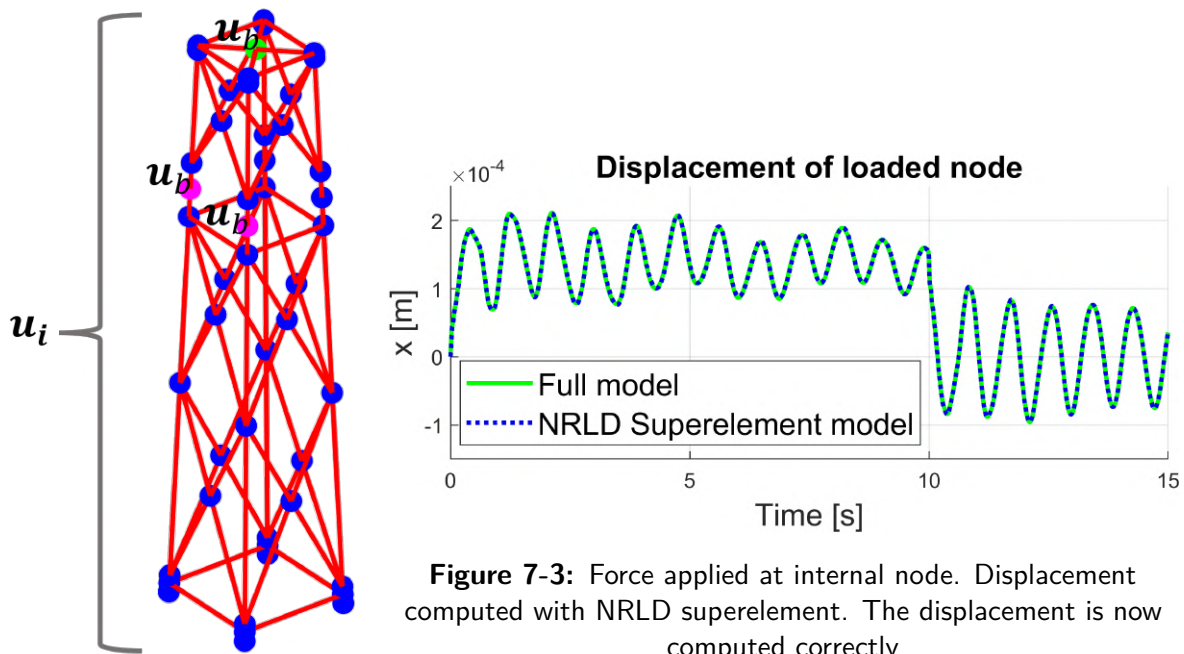


Figure 7-2: Jacket nodes divided in boundary nodes and internal nodes with NRLD approach

Figure 7-3: Force applied at internal node. Displacement computed with NRLD superelement. The displacement is now computed correctly

7-2 Coupled simulations in superelement domain

In Section 4-3-2, it was described how structural computations in the modal domain could be coupled to ice computations in the spatial domain. The same coupling must be done using the dynamic substructuring method. Now structural computations in the 'superelement domain' must be coupled to ice computations in the spatial domain. Think of the modal eigenmatrix Φ as the 'transfer function' between the modal domain and the spatial domain. The reduction matrix R , can be interpreted as the transfer function between the superelement domain and the spatial domain. Using this, the MATLAB model used to model ice-structure interaction in the modal domain was successfully rewritten to model ice-structure interaction in the superelement domain.

Two things are important to consider. One is that the primal assembly method described in Section 6-2-1 should be used, as the ODE solver cannot deal with the singular matrices resulting from the dual assembled equations, shown in Eq.6.19. Rewriting this equation into state space form would require to divide the equation by the mass matrix. Since this mass matrix is singular, the output would not be representative. The primal assembly system in Eq.6.16 does not contain singular matrices. Therefore, this system of equations can be rewritten into state-space form and implemented into the ODE solver accordingly. Second is that the NRLD approach explained in Section 7-1 should be used to improve accuracy. The differences in accuracy between the regular and the NRLD approach are considered in the next section.

7-2-1 NRLD accuracy

To see the effect of the NRLD approach, the NRLD solution is compared to the modal domain solution and to the regular superelement solution. In this example, the modal domain solution including modes up to 1500 [Hz] is used as a reference solution. Almost all modes are included in this way, leading to the most exact solution. Next, the solutions using the NRLD superelement and the normal superelement are compared, of which the results can be seen in Fig.7-4.

What can be seen is that coupled ice-structure interaction can be modelled using the Craig-Bampton reduction method, as the solutions of both superelement models match with the modal domain solution. However, using the NRLD approach leads to more accurate results, as the regular superelement domain solution starts to diverge from the reference solution after some simulation time. Note that both superelement models were constructed including 200 vibration modes, which is more than usual. It was found that including less vibration modes in the reduction matrix, lead to diverging results earlier in the simulation, also for the NRLD approach. To verify whether the nature of the accumulating errors is numerical and not fundamental, the analysis explained in the next section was performed.

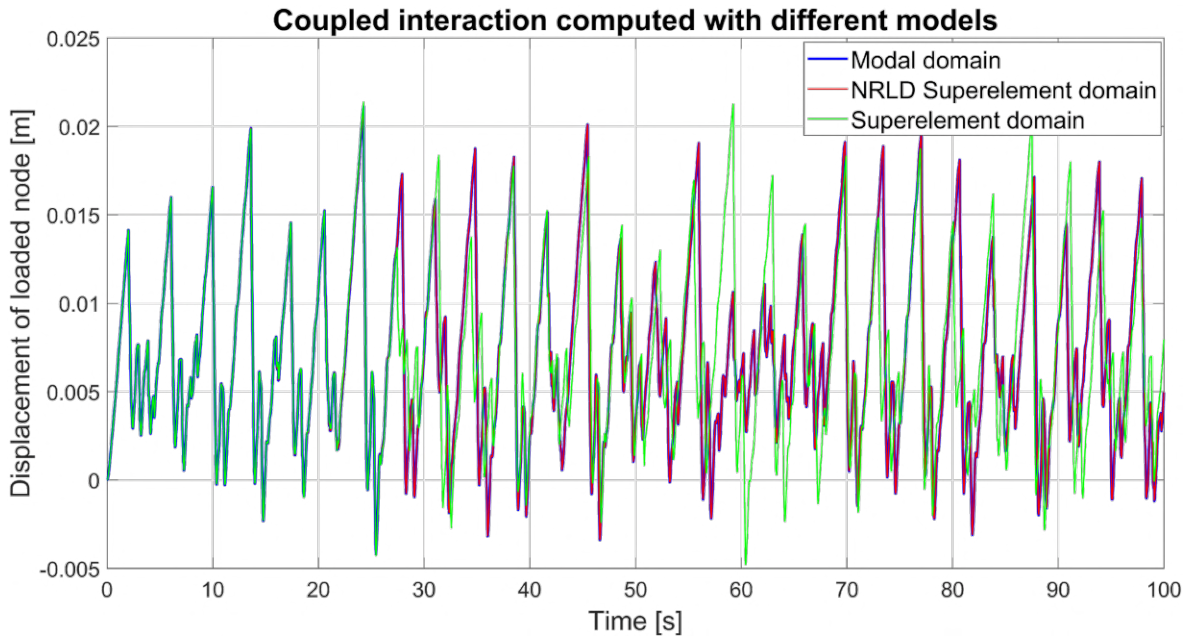


Figure 7-4: Comparison between modal, NRLD superelement and regular superelement solution for $v_{ice} = 0.01$ [m/s]

7-2-2 Numerical errors

Consider Fig.7-5, where interaction is modelled for an ice velocity of 0.01 [m/s], using both modelling domains, i.e. modal domain and NRLD superelement domain. Again, the modal domain solution including modes up to 1500 [Hz] is used as reference solution. In this example less vibrational modes, namely 150 instead of 200, are included in the reduction matrix of the NRLD superelement, which leads to correct results up to $t = 16$ [s], but starts diverging after that. To check whether this is a fundamental error or a numerical error, an 'Initial conditions check' was performed. In this example, the data from the modal domain solution at $t = 33$ [s] was extracted and implemented as initial conditions in the NRLD superelement model. The NRLD superelement was re-run with these initial conditions, providing the output indicated in green. What can be seen is that the solution now approaches the reference solution much better than before, indicating that the deviation is due to an accumulating numerical error and not a fundamental error. The error can be described as an accuracy error, not a stability error.

The same behaviour is found when comparing two modal domain solutions, each with a different number of modes included. Solutions start to diverge after some time, but implementing the solution data at a certain point in time from the model that is truncated less as initial conditions in the model that is truncated more will lead to the same results. The effect due to a different order of truncation of the modally reduced systems and the effect of including

a different number of vibration modes in the reduction matrix is thus comparable. Since the accumulation of numerical errors is present both in the modal domain approach as well as in the NRLD superelement approach, it is found that this error is not specific regarding the superelement method.

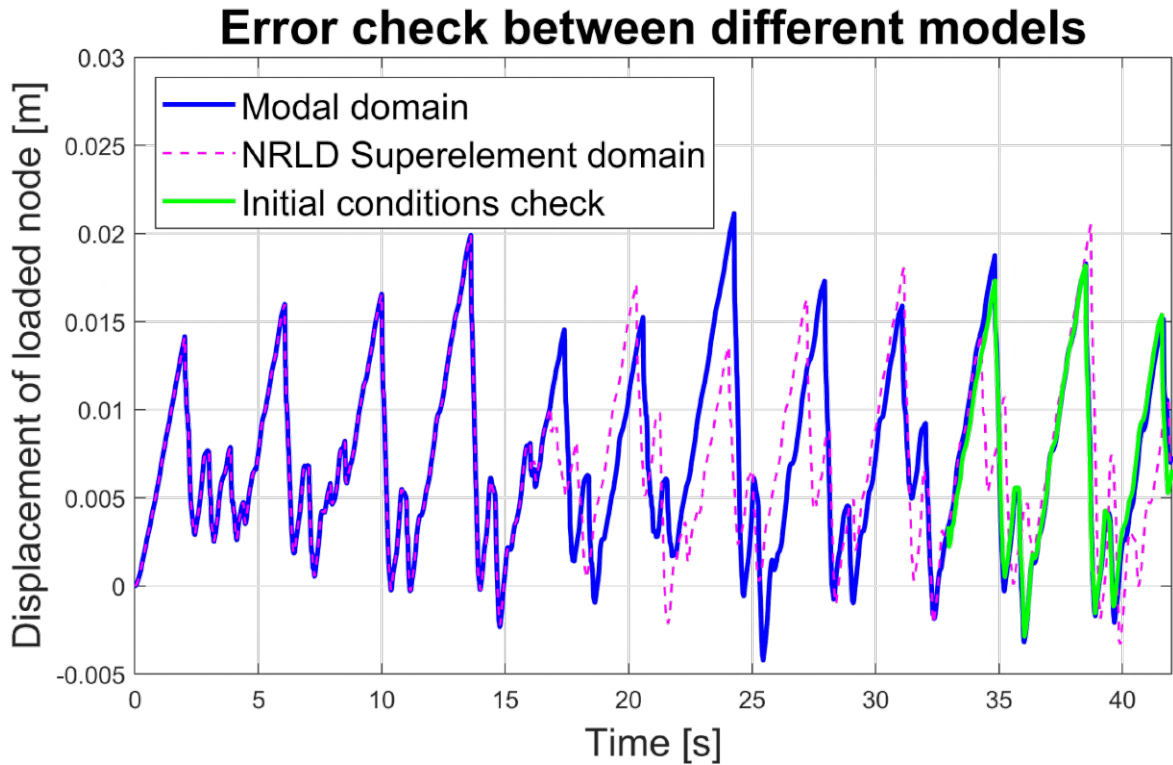
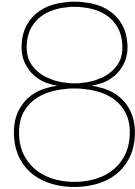


Figure 7-5: Comparison between modal domain and superelement domain solution

To conclude and to answer the second research question of this thesis: it is possible to model coupled dynamic ice-structure interaction using a dynamic substructuring modelling technique. However, challenges related to the accumulation of numerical accuracy errors arise with truncation of more higher frequency modes. Solving this numerical error is not considered in the scope of this thesis. One hypothesis is that the slight difference in structural response caused by truncating or including less vibrational modes results in the ice elements breaking at a slightly different timing. The result of the different timing is that the force induced to the structure slightly differs. The effect of this amplifies over time, resulting in the diverging displacement profiles.



Conclusions and recommendations

In this thesis several models were constructed in order to answer two different research questions. This chapter will provide the conclusions to these questions as well as recommendations for future research.

8-1 Conclusions

8-1-1 Part I

Part I of this thesis addressed the first research question defined as "Can the use of the Type 1 design be justified or is a Type 2 jacket also suitable in sub-arctic areas?" To answer that question, several models were constructed, each yielding a part of the answer.

First, a model was constructed that quantifies what types of ice failure are occurring simultaneously at a Type 2 jacket substructure, as function of the ice approach angle relative to the structure and as function of an introduced threshold angle. The model quantified the elements that would be loaded by ice failing in crushing or in bending, as those were the only failure types considered in this research. Since both failure types induce a different type of load to the structure, it is important to quantify the interaction in order to calculate the total load on the structure. The influence of the threshold angle has been assessed, as the angle can be assumed differently according to multiple design standards and previous research. As a result, it was found that assuming of a threshold angle of 70 [deg], ice bending failure would be equally significantly present as ice crushing failure. Therefore, both failure types had to be accounted for in the research.

Accordingly, ice models have been constructed for both ice bending and ice crushing failure. To model ice bending failure, a slab of an ice sheet was represented by a beam, described by Euler-Bernoulli beam theory. The equation of motion describing the beam was extended with terms representing the buoyancy, axial compression force, convective velocity and proportional damping. Using the finite difference method, this equation of motion was rewritten into state-space form and solved through the ODE45 solver in MATLAB. The solution provided the displacement of the ice beam over time upon interacting with a sloping structure. By computing the tensile stress in the beam, it could be determined when the ice beam would break and what the length would be of the broken off piece. Rewriting the boundary conditions yielded the horizontal force induced to the structure, which could be calculated for multiple ice velocities and thicknesses. It was found that the maximum horizontal forces induced correspond well to the values that could be deduced using the design code (IEC 61400-3-1, 2019b) and that the maximum induced force does not depend on ice velocity. Only the breaking time reduces for higher ice velocities. The information regarding the breaking time and length was used to assess whether dynamic amplification could develop upon loading a jacket substructure by ice failing in bending. As a result, it was found that dynamic amplification could in theory occur with the assumptions made in the model, however likely not in practice as will be further discussed in Section 8-2.

To model ice crushing failure, the phenomenological ice model as described by Hendrikse and Nord (2019) was implemented and coupled to the structural models representing both jacket types. This allowed to compute the global ice load induced to the loaded parts of the structure and to analyse which IIV regimes would develop globally and locally. It was found that local IIV regimes can be recognised, including local FLI, but sustained local FLI could not be observed, as the global motion of the jacket prevents sustained local FLI to build up. However simultaneously, the global motion facilitates the build up of unsustained local FLI. Several case studies were performed both on jackets with altered structural properties to enhance the susceptibility to IIV and on a structural model representing only the bracing in the jacket, to see if sustained FLI could build up. As a result, no sustained FLI was observed in these case studies either.

The load induced by ice bending failure was found to be much lower than by ice crushing failure. To assess the maximum base shear that could develop in the jacket, the contributions of loads by bending ice and crushing ice were added. The situation yielding the highest peak base shear load was found with help of the quantification model. Next, it was assessed that the base shear due to ice loading is of the same order of magnitude in wave loading, concluding that in terms of base shear, ice is not severe for a Type 2 jacket. Note that this holds for the Type 2 jacket considered in this thesis. The base shear for a Type 2 jacket having other dimensions should be reassessed.

Next, the ULS brace load was assessed and using a simplified approach the maximum induced bending moment in the brace could be calculated. This bending moment was then used to verify whether it would be safe enough according to the bending check provided in the ISO code (ISO 19902, 2007). It was found that the utilisation is below unity for all ice velocities,

however close to unity for low ice velocities in the IC regime. Therefore, the ULS brace load should be assessed with care when considering other jacket designs.

To conclude on the first research question, a Type 2 jacket is suitable to be used in sub-arctic areas but the ULS brace load should be carefully assessed as the utilisation is close to unity.

8-1-2 Part II

Part II of this thesis addressed the second research question defined as "Can coupled dynamic ice-structure interaction be modelled by a dynamic substructuring modelling technique?"

To answer that question, first a study was performed to understand the concept and the limitations of the Craig-Bampton method. In this way, it could be assessed what is important to take into account and which difficulties would arise trying to implement the method in coupled ice-structure interaction. With this knowledge a superelement model representing the jacket could be set up and the coupling of this jacket superelement to a tower-RNA assembly was realised. This integrated model allowed for performing dynamic simulations.

However, it was found that the dynamics of the internal loaded DoFs could not be captured well, something that is crucial in coupled ice-structure interaction. This problem was solved by including the loaded DoFs in the subset of retained boundary nodes instead of in the subset of reduced nodes, named the NRLD approach. This NRLD approach is convenient considering ice loading because few DoFs are loaded, maintaining the effectiveness of the reduction. As a result, the NRLD approach yielded more accurate results compared to the superelement assembly obtained earlier.

Furthermore, it was found that the primal assembly method should be used, because of two reasons. One is because the computational time was found to be two times faster compared to simulations performed with the a dual assembled system. Second is that the dual assembly procedure yields singular mass and damping matrices, which can not be implemented in the ODE45 solver solving the ice equations. This would prevent simultaneous solving of ice and structure displacements. The primal assembly method yields a system that can be implemented in this solver, allowing for simultaneous solving of ice and structure equations.

Next, the solutions of the superelement model have been compared with modal domain solutions. It was found that the method is able to solve coupled ice-structure problems, however accumulating numerical accuracy errors develop over time. Besides, accumulating numerical errors were found both in modal domain solutions and in superelement domain solutions, leading to inaccurate, but not unstable results. Since this numerical error does exist in modal domain solutions too, the effectiveness of the superelement domain method is substantiate.

To conclude on the second research question, it is possible to model coupled ice-structure interaction using a dynamic substructuring modelling technique and a framework to do so is provided. The implementation of the dynamic substructuring modelling technique was successfully done and coupled ice-structure interaction can be modelled with it. However, the accumulating numerical errors should be resolved.

8-2 Recommendations

The models presented in Part I can be improved and expanded and the errors found in Part II can be resolved. In this section, suggestions are posed for further research.

8-2-1 Part I

To start, in this research the contributions of ice bending failure and ice crushing failure to the structural response have been considered separately, according to the superposition principle. In reality, both ice failure types will occur at a jacket simultaneously. The response induced by ice bending failure will then influence the response due ice crushing failure. It could then for instance be investigated whether global IIV due to ice crushing failure will be disturbed by the influence of ice bending failure. The quantification model presented in Chapter 3 could in future research be used to determine to what extent bending and crushing are related, in order to couple both ice failure types in a single model.

Next, the ice bending model could be further improved. Now, the broken off part is removed numerically, whereas in reality this piece of ice would continue to interact with the structure. For example, these parts could be piling up or cause jamming between the jacket braces. This is not considered in this thesis, but could have a reducing effect on the dynamic amplification induced by ice bending failure. Furthermore, the bending model could be improved by assuming plate theory instead of beam theory. Then the influence of radial cracks and circumferential cracks can be included in the model, better representing the failure behaviour of ice on sloping surfaces. It is expected that including these failure modes will result in shorter breaking lengths, better corresponding to the breaking lengths found in literature. Besides, only a downward ice bending model was constructed. In this thesis the loads induced by upward bending ice were found by applying a factor to the computed downward bending ice load, according to IEC61400 (2019b). In future research, an upward ice bending model should be constructed as well, to better compare the differences between downward and upward ice bending. Moreover, unlike the ice crushing model, the ice bending model constructed is not coupled to the displacement of the structure and the structure is assumed to be rigid while loaded. In reality, the structure will deflect upon interaction, influencing the failure behaviour of the ice because the boundary conditions change. The obtained breaking times and lengths could therefore be calculated more realistically.

Also, apart from only ice bending and ice crushing failure, other failure modes should be added to the model, i.e. splitting ice between jacket elements and buckling at vertically sided structures. The contribution and influence of these failure modes and the effect of jamming to the total load on the structure should be assessed.

Regarding the structural model, the OC4 reference jacket was used as input for the structural model, but considering the rapid development and increasing size of offshore wind turbines, this is a relatively small structure. Future research should focus on larger structures, leading to increased loads on the members but reducing the effect of jamming for example. Another remark regarding the structural model, is that the RNA is modelled as a lumped mass, disregarding the blade dynamics which are important to include, as they can interfere with the load frequencies. Besides that, aerodynamic damping is not considered, which does influence the structural vibrations. However, this mainly influences the global response of the structure and not the local brace response, which was the main objective of research in this thesis. In future research, the RNA should be modelled as a complete assembly and aerodynamic damping should be included in the model. Another remark regarding the structure is that only one structural damping value is assumed. In future research the influence of structural damping on the results should be assessed. Final remark regarding the structure, is that soil-structure interaction is not taken into account in this research. The jacket is instead fixed to the ground at seabed level, increasing the stiffness of the structure and disregarding the soil damping. In this thesis the mass of the TP could be tuned, influencing the natural frequency of the structure. In future research, the soil dynamics should be included, leading to more accurate results. Again, this mainly influences the global response of the structure and not the local brace response, which was the main objective of research in this thesis.

With the models constructed in this thesis it is possible to obtain the structural responses at each node in the jacket due to forces induced by bending ice and crushing ice. It is however more difficult to obtain the stresses in the structural members because the model is not refined enough on local level. Future research could update the structural model with more refined methods, for example using FEM software like ANSYS. This would make it possible to compute the stresses induced in the braces and nodes by dynamic and static ice loading. A thorough fatigue assessment can then be performed to assess the contribution to fatigue by the unsustained local FLI. Besides that, a more refined ULS brace bending assessment can be performed making use of the computed stresses in the braces.

Finally, the overturning moment was not assessed in this thesis, but could be severe regarding ice loading. This is because in contrast to wave loading, all the load is applied at the top of the jacket, resulting in large overturning moment. So, although the maximum base shear was found to be comparable between ice and wave loading, this is not the case for the overturning moment, as should be investigated in further research.

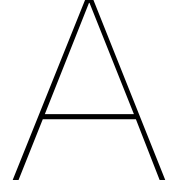
8-2-2 Part II

The dynamic substructuring technique was successfully implemented to model coupled ice-structure interaction. However, accumulating numerical errors exist and should be fixed in future work. One cause of the diverging results between differently modally truncated models could be that the slight difference in structural response caused by the different truncation results in the ice elements breaking at a slightly different timing. As a result, the force induced to the structure slightly differs, of which the effect amplifies over time, resulting in the diverging displacement profiles. The same observation can be made regarding superelement models, which are differently 'truncated' by including a different number of vibrational modes in the reduction matrix. Further research is required to investigate this hypothesis.

When this accuracy problem is solved, a study could be performed on optimizing the reduction method. It should be further investigated what the most optimal reduction method is in terms of which nodes to exclude from the subset of reduced DoFs and thus retain as boundary DoFs (NRLD approach). In this research only two DoFs were retained as boundary DoFs, as these were the only DoFs that were loaded in the simulation. In reality, all nodes at the waterline could be loaded by ice and an NRLD superelement should be constructed accordingly.

Additionally, the amount of included vibration modes in the reduction matrix should be optimised. Including less vibrational modes will result in less computational time, but it should be ensured that the result is still accurate and that the highest frequency of interest can still be captured by the reduced model, also known as spectral convergence. On top of that, the amount of vibrational modes should be optimised through spatial convergence. Then not only the correct frequencies can be captured by the superelement model, but also the spatial distribution of the ice loading is represented correctly. It is expected that the spatial distribution of the ice loading is of less importance compared to wave loading, because the load is applied at one level only, but this should be verified in future research.

At last, in the superelement assembly model the RNA should be represented by a turbine consisting of blades too, instead of by a lumped mass. Then the blade dynamics are also included in the model. The coupling of the tower and RNA can be done in the same way as was done coupling the jacket superelement and the tower-RNA assembly in this thesis, but then having three substructures instead of two.



Derivations

Convective term derivation

Let u be the displacement of the beam in vertical direction and x the displacement of the beam in horizontal direction. The total vertical convective displacement of the beam is then expressed as:

$$u_{conv} = u + u(\Delta x) = u + \Delta x \frac{\delta u}{\delta x} \quad (\text{A.1})$$

The vertical convective velocity then becomes:

$$v_{conv} = \frac{du}{dt} = \frac{\delta}{\delta t} u_{conv} = \frac{\delta u}{\delta t} + \frac{\delta u}{\delta t} (\Delta x) = \frac{\delta u}{\delta t} + \frac{\Delta x}{\Delta t} \frac{\delta u}{\delta x} = \frac{\delta u}{\delta t} + v_x(t) \frac{\delta u}{\delta x} \quad (\text{A.2})$$

Where $v_x(t)$ is the horizontal velocity. The acceleration is then:

$$\frac{d^2 u}{dt^2} = \frac{d}{dt} \left(\frac{du}{dt} \right) = \frac{d}{dt} \left(\frac{\delta u}{\delta t} \right) + \frac{d}{dt} \left(v_x(t) \frac{\delta u}{\delta x} \right) \quad (\text{A.3})$$

Where:

$$\frac{d}{dt} \left(\frac{\delta u}{\delta t} \right) = \frac{\delta}{\delta t} \left(\frac{\delta u}{\delta t} \right) + \frac{\delta x}{\delta t} \frac{\delta}{\delta x} \left(\frac{\delta u}{\delta t} \right) = \frac{\delta^2 u}{\delta t^2} + v_x(t) \frac{\delta^2 u}{\delta x \delta t} \quad (\text{A.4})$$

And:

$$\begin{aligned}
\frac{d}{dt} \left(v_x(t) \frac{\delta u}{\delta x} \right) &= \frac{\delta}{\delta t} \left(v_x(t) \frac{\delta u}{\delta x} \right) + \frac{\delta x}{\delta t} \frac{\delta}{\delta x} \left(v_x(t) \frac{\delta u}{\delta x} \right) \\
\frac{\delta}{\delta t} \left(v_x(t) \frac{\delta u}{\delta x} \right) &= \frac{\delta u}{\delta x} \frac{\delta}{\delta t} (v_x(t)) + v_x(t) \frac{\delta}{\delta t} \left(\frac{\delta u}{\delta x} \right) = \frac{\delta u}{\delta x} a_x(t) + v_x(t) \frac{\delta^2 u}{\delta x \delta t} \\
\frac{\delta x}{\delta t} \frac{\delta}{\delta x} \left(v_x(t) \frac{\delta u}{\delta x} \right) &= v_x(t) \left(v_x(t) \frac{\delta}{\delta x} \frac{\delta u}{\delta x} \right) = v_x(t)^2 \frac{\delta^2 u}{\delta x^2}
\end{aligned} \tag{A.5}$$

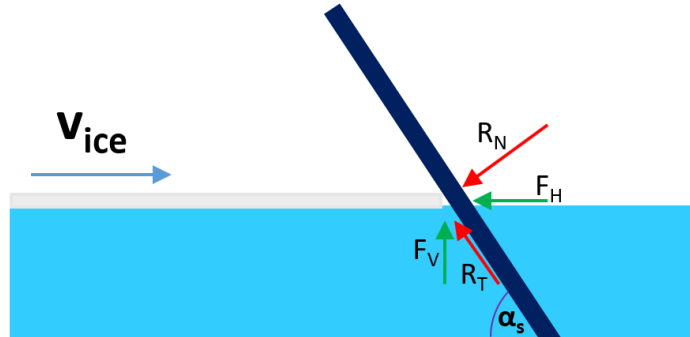
Ultimately, this leads to the convective acceleration as:

$$\begin{aligned}
\frac{d^2 u}{dt^2} &= \frac{\delta^2 u}{\delta t^2} + v_x(t) \frac{\delta^2 u}{\delta x \delta t} + \frac{\delta u}{\delta x} a_x(t) + v_x(t) \frac{\delta^2 u}{\delta x \delta t} + v_x(t)^2 \frac{\delta^2 u}{\delta x^2} \\
&= \frac{\delta^2 u}{\delta t^2} + 2v_x(t) \frac{\delta^2 u}{\delta x \delta t} + \frac{\delta u}{\delta x} a_x(t) + v_x(t)^2 \frac{\delta^2 u}{\delta x^2}
\end{aligned} \tag{A.6}$$

In this research, the horizontal velocity of the ice is assumed constant. This means that the acceleration is zero and that the horizontal velocity is independent of time:

$$\frac{d^2 u}{dt^2} = \frac{\delta^2 u}{\delta t^2} + 2v_x \frac{\delta^2 u}{\delta x \delta t} + v_x^2 \frac{\delta^2 u}{\delta x^2} \tag{A.7}$$

Derivation of ζ



When it is assumed that the sheet of ice glides continuously along the structure slope (no stick-slip), the relation between the normal force F_H and transversal force F_V can be expressed as:

$$\begin{aligned} F_V &= R_T \sin \alpha_s - R_N \cos \alpha_s \\ F_H &= R_T \cos \alpha_s + R_N \sin \alpha_s \\ R_T &= \mu \cdot R_N \end{aligned} \quad (\text{A.8})$$

Leading to:

$$\zeta = \frac{F_H}{F_V} = \frac{\sin \alpha_s + \mu \cos \alpha_s}{-\cos \alpha_s + \mu \sin \alpha_s} \quad (\text{A.9})$$

In which:

α_s	Structure angle	[rad]
μ	Ice-structure friction coefficient	[-]
F_V	Transversal force	[N]
F_H	Normal force	[N]
R_T	Tangential reaction force	[N]
R_N	Normal reaction force	[N]

Damping term derivation

The damping term is set proportional to the first derivative in time of the axial compression term in the equation of motion of the beam:

$$F_{damping} = c \frac{d}{dt} \left(N \frac{\delta^2 u}{\delta x^2} \right) \quad (\text{A.10})$$

The first derivative in time (convective velocity) was defined as:

$$\frac{du}{dt} = \frac{\delta u}{\delta t} + v_x \frac{\delta u}{\delta x} \quad (\text{A.11})$$

The damping term can then be further derived as:

$$\begin{aligned} F_{damping} &= c \frac{d}{dt} \left(N \frac{\delta^2 u}{\delta x^2} \right) = c \frac{\delta}{\delta t} \left(N \frac{\delta^2 w}{\delta x^2} \right) + c v_x \frac{\delta}{\delta x} \left(N \frac{\delta^2 w}{\delta x^2} \right) \\ &= c N \frac{\delta^3 w}{\delta t \delta x^2} + c v_x N \frac{\delta^3 w}{\delta x^3} \\ &= c N \left(\frac{\delta^3 w}{\delta t \delta x^2} + v_x \frac{\delta^3 w}{\delta x^3} \right) \end{aligned} \quad (\text{A.12})$$

Here c [s] is the material damping coefficient of the ice. The minus sign in the equation of motion is because the damping has to dissipate energy from the system.

B

Finite difference approximation

Finite difference method

The finite difference method is a technique for solving differential equations by approximating (higher order) derivatives by finite differences. In this way, the system is converted into a set of linear equations that can be solved by matrix algebra techniques. The system is divided into n elements, each indicated by an index i . The (central) finite difference equations used are:

$$\begin{aligned}\frac{\delta u_i}{\delta x} &= \frac{1}{2\Delta x}(u_{i+1} - u_{i-1}) \\ \frac{\delta^2 u_i}{\delta x^2} &= \frac{1}{\Delta x^2}(u_{i+1} - 2u_i + u_{i-1}) \\ \frac{\delta^3 u_i}{\delta x^3} &= \frac{1}{2\Delta x^3}(u_{i+2} - 2u_{i+1} + 2u_{i-1} - u_{i-2}) \\ \frac{\delta^4 u_i}{\delta x^4} &= \frac{1}{\Delta x^4}(u_{i+2} - 4u_{i+1} + 6u_i - 4u_{i-1} + u_{i-2})\end{aligned}\tag{B.1}$$

For $i = 1 \dots n$.

Discretisation of the equation of motion

The total equation of motion representing a slab of ice as an Euler-Bernoulli beam as derived in section 2-1 is:

$$\rho A \left(\underbrace{\frac{\delta^2 u_z}{\delta t^2}}_{\text{mass}} + \underbrace{2v_x \frac{\delta^2 u_z}{\delta x \delta t} + v_x^2 \frac{\delta^2 u_z}{\delta x^2}}_{\text{convective}} \right) + \underbrace{EI \frac{\delta^4 u_z}{\delta x^4}}_{\text{beam stiffness}} + \underbrace{ku_z}_{\text{buoyancy}} + \underbrace{N \frac{\delta^2 u_z}{\delta x^2}}_{\text{axial compression}} - \underbrace{cN \left(\frac{\delta^3 u_z}{\delta x^2 \delta t} + v_x \frac{\delta^3 u_z}{\delta x^3} \right)}_{\text{damping}} = 0 \quad (\text{B.2})$$

The subscript z indicating that the deformation is in the vertical direction will be omitted in further equations. Working out parentheses in Eq.B.2 yields:

$$\rho A \frac{\delta^2 u}{\delta t^2} + \rho A 2v_x \frac{\delta^2 u}{\delta x \delta t} + \rho A v_x^2 \frac{\delta^2 u}{\delta x^2} + EI \frac{\delta^4 u}{\delta x^4} + ku + N \frac{\delta^2 u}{\delta x^2} - cN \frac{\delta^3 u}{\delta x^2 \delta t} - cN v_x \frac{\delta^3 u}{\delta x^3} = 0 \quad (\text{B.3})$$

Isolating the acceleration yields:

$$\frac{\delta^2 u}{\delta t^2} = -\frac{EI}{\rho A} \frac{\delta^4 u}{\delta x^4} - \frac{N}{\rho A} \frac{\delta^2 u}{\delta x^2} - \frac{k}{\rho A} u + \frac{cN v_x}{\rho A} \frac{\delta^3 u}{\delta x^3} - v_x^2 \frac{\delta^2 u}{\delta x^2} + \frac{cN}{\rho A} \frac{\delta^3 u}{\delta x^2 \delta t} - 2v_x \frac{\delta^2 u}{\delta x \delta t} \quad (\text{B.4})$$

For each node i in the beam the acceleration can be calculated through the finite difference approximation. This yields:

$$\begin{aligned} \frac{\delta^2 u_i}{\delta t^2} = & -\frac{EI}{\rho A \Delta x^4} (u_{i+2} - 4u_{i+1} + 6u_i - 4u_{i-1} + u_{i-2}) - \frac{N}{\rho A \Delta x^2} (u_{i+1} - 2u_i + u_{i-1}) \\ & - \frac{k}{\rho A} (u_i) + \frac{cN v_x}{2\rho A \Delta x^3} (u_{i+2} - 2u_{i+1} + 2u_{i-1} - u_{i-2}) - \frac{v_x^2}{\Delta x^2} (u_{i+1} - 2u_i + u_{i-1}) \\ & + \frac{cN}{\rho A \Delta x^2} (u_{n+i+1} - 2u_{n+i} + u_{n+i-1}) - \frac{v_x}{\Delta x} (u_{n+i+1} - u_{n+i-1}) \end{aligned} \quad (\text{B.5})$$

This second order differential equation can be represented by a system of first order differential equations as:

$$\begin{aligned}\frac{\delta u_i}{\delta t} &= u_{n+i} \\ \frac{\delta u_{n+i}}{\delta t} &= \frac{\delta^2 u_i}{\delta t^2} = \text{Eq. B.5}\end{aligned}\tag{B.6}$$

The axial compression is approximated using backward differences, since not enough information is available here to use central differences:

$$N = \frac{\frac{-EI\zeta}{\Delta x^3}(u_n - 3u_{n-1} + 3u_{n-2} - u_{n-3})}{1 + \frac{\zeta}{\Delta x}(u_n - u_{n-1}) - \frac{c\zeta}{\Delta x}(u_{2n} - u_{2n-1}) - \frac{cv_x\zeta}{\Delta x^2}(u_n - 2u_{n-1} + u_{n-2})}\tag{B.7}$$

Initial conditions

For each node i the initial conditions are:

$$\text{at } t = 0: \quad u_i = \dot{u}_i = u_{n+i} = 0\tag{B.8}$$

Boundary conditions

For several values of i , information is needed from nodes that are outside the domain. To obtain expressions for these nodes the boundary conditions are used. To compute $i = 1$, the deflection at $i = -1$ is required. The boundary condition at $i = 0$ can be used to find an expression for u_{-1} :

$$\begin{aligned}\text{for } i = 1 \quad \frac{\delta u_0}{\delta x} &= \frac{1}{\Delta x}(u_1 - u_{-1}) = 0 \\ &u_{-1} = u_1\end{aligned}\tag{B.9}$$

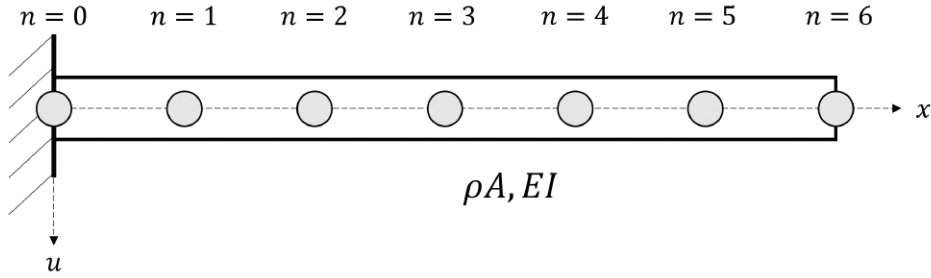
The deflection at node $i = 0$ does not have to be computed since it is a boundary condition itself. Now the left end of the beam is defined.

At the right end of the beam, $i = n$ does not have to be solved since this is also a boundary condition of the system. For $i = n - 1$, for some terms the deflection at $i = n + 1$ is needed.

Since this point lies outside the domain the moment boundary condition at the right end of the beam must be used to find an expression for u_{n+1} :

$$\begin{aligned}
 \text{for } i = n - 1 \quad -EI \frac{\delta^2 u_n}{\delta x^2} &= -\frac{hF_H}{2} \\
 \frac{\delta^2 u_n}{\delta x^2} &= \frac{1}{\Delta x^2} (u_{n+1} - 2u_n + u_{n-1}) = \frac{hF_H}{2EI} \\
 u_{n+1} &= \frac{hF_H \Delta x^2}{2EI} + 2u_n - u_{n-1}
 \end{aligned} \tag{B.10}$$

Matrix representation



To explain the matrix representation of the finite difference discretisation, consider the following simple beam equation:

$$\rho A \frac{\delta^2 u_i}{\delta x^2} + EI \frac{\delta^4 u_i}{\delta x^4} = 0 \tag{B.11}$$

Applying the finite difference method and representing the resulting second order differential equation as a system of first order differential equations yields:

$$\begin{aligned}
 \frac{\delta u_i}{\delta t} &= u_{n+i} \\
 \frac{\delta u_{n+i}}{\delta t} &= \frac{\delta^2 u_i}{\delta t^2} = -\frac{EI}{\rho A \Delta x^4} (u_{i+2} - 4u_{i+1} + 6u_i - 4u_{i-1} + u_{i-2})
 \end{aligned} \tag{B.12}$$

In the example illustrated in the figure above, there are seven nodes in the domain of the beam, of which the displacements are named $u_0 \dots u_6$. Without applying boundary conditions, the matrix form of the equation would be:

$$\begin{bmatrix} \ddot{u}_{-2} \\ \ddot{u}_{-1} \\ \ddot{u}_0 \\ \ddot{u}_1 \\ \ddot{u}_2 \\ \ddot{u}_3 \\ \ddot{u}_4 \\ \ddot{u}_5 \\ \ddot{u}_6 \\ \ddot{u}_7 \\ \ddot{u}_8 \end{bmatrix} = -\frac{EI}{\rho A \Delta x^4} \begin{bmatrix} 1 & -4 & 6 & -4 & 1 & 0 & 0 & 0 & 0 & 0 & 0 \\ 0 & 1 & -4 & 6 & -4 & 1 & 0 & 0 & 0 & 0 & 0 \\ 0 & 0 & 1 & -4 & 6 & -4 & 1 & 0 & 0 & 0 & 0 \\ 0 & 0 & 0 & 1 & -4 & 6 & -4 & 1 & 0 & 0 & 0 \\ 0 & 0 & 0 & 0 & 1 & -4 & 6 & -4 & 1 & 0 & 0 \\ 0 & 0 & 0 & 0 & 0 & 1 & -4 & 6 & -4 & 1 & 0 \\ 0 & 0 & 0 & 0 & 0 & 0 & 1 & -4 & 6 & -4 & 1 \end{bmatrix} \begin{bmatrix} u_{-2} \\ u_{-1} \\ u_0 \\ u_1 \\ u_2 \\ u_3 \\ u_4 \\ u_5 \\ u_6 \\ u_7 \\ u_8 \end{bmatrix} \quad (\text{B.13})$$

The displacement u_0 is a boundary condition of the system, therefore it does not have to be solved and u_{-2} is not needed anymore. To solve u_1 , u_{-1} is needed. Here the left boundary condition derived in 'Boundary conditions' can be applied, where it was found that $u_{-1} = u_1$. Including this boundary condition results in the following matrix equation:

$$\begin{bmatrix} \ddot{u}_1 \\ \ddot{u}_2 \\ \ddot{u}_3 \\ \ddot{u}_4 \\ \ddot{u}_5 \\ \ddot{u}_6 \\ \ddot{u}_7 \\ \ddot{u}_8 \end{bmatrix} = -\frac{EI}{\rho A \Delta x^4} \begin{bmatrix} 7 & -4 & 1 & 0 & 0 & 0 & 0 & 0 \\ -4 & 6 & -4 & 1 & 0 & 0 & 0 & 0 \\ 1 & -4 & 6 & -4 & 1 & 0 & 0 & 0 \\ 0 & 1 & -4 & 6 & -4 & 1 & 0 & 0 \\ 0 & 0 & 1 & -4 & 6 & -4 & 1 & 0 \\ 0 & 0 & 0 & 1 & -4 & 6 & -4 & 1 \end{bmatrix} \begin{bmatrix} u_1 \\ u_2 \\ u_3 \\ u_4 \\ u_5 \\ u_6 \\ u_7 \\ u_8 \end{bmatrix} \quad (\text{B.14})$$

The displacement u_6 is a boundary condition of the system, therefore it does not have to be solved and u_8 is not needed anymore. To solve u_5 , information about displacement u_7 is required. Here the right moment boundary condition derived in 'Boundary conditions' can be applied, where it was found that $u_{n+1} = \frac{hF_H \Delta x^2}{2EI} + 2u_n - u_{n-1}$. Implementing this result yields the matrix equation:

$$\begin{bmatrix} \ddot{u}_1 \\ \ddot{u}_2 \\ \ddot{u}_3 \\ \ddot{u}_4 \\ \ddot{u}_5 \\ \ddot{u}_6 \end{bmatrix} = -\frac{EI}{\rho A \Delta x^4} \begin{bmatrix} 7 & -4 & 1 & 0 & 0 & 0 \\ -4 & 6 & -4 & 1 & 0 & 0 \\ 1 & -4 & 6 & -4 & 1 & 0 \\ 0 & 1 & -4 & 6 & -4 & 1 \\ 0 & 0 & 1 & -4 & 5 & -2 \\ 0 & 0 & 0 & 0 & 0 & 0 \end{bmatrix} \begin{bmatrix} u_1 \\ u_2 \\ u_3 \\ u_4 \\ u_5 \\ u_6 \end{bmatrix} - \frac{hF_H \Delta x^2}{2EI} \begin{bmatrix} 0 \\ 0 \\ 0 \\ 0 \\ 1 \\ 0 \end{bmatrix} \quad (\text{B.15})$$

The displacement u_6 is dependent of time. It is therefore convenient to leave it inside the matrix because then the value can be updated inside the ODE45 loop in MATLAB.

The matrix representation of the system from Eq.B.12 is then:

$$\begin{bmatrix} \dot{u}_1 \\ \dot{u}_2 \\ \dot{u}_3 \\ \dot{u}_4 \\ \dot{u}_5 \\ \dot{u}_6 \\ \ddot{u}_1 \\ \ddot{u}_2 \\ \ddot{u}_3 \\ \ddot{u}_4 \\ \ddot{u}_5 \\ \ddot{u}_6 \end{bmatrix} = \begin{bmatrix} 0 & 0 & 0 & 0 & 0 & 0 & 1 & 0 & 0 & 0 & 0 & 0 \\ 0 & 0 & 0 & 0 & 0 & 0 & 0 & 1 & 0 & 0 & 0 & 0 \\ 0 & 0 & 0 & 0 & 0 & 0 & 0 & 0 & 1 & 0 & 0 & 0 \\ 0 & 0 & 0 & 0 & 0 & 0 & 0 & 0 & 0 & 1 & 0 & 0 \\ 0 & 0 & 0 & 0 & 0 & 0 & 0 & 0 & 0 & 0 & 1 & 0 \\ 0 & 0 & 0 & 0 & 0 & 0 & 0 & 0 & 0 & 0 & 0 & 1 \\ 7K & -4K & 1K & 0 & 0 & 0 & 0 & 0 & 0 & 0 & 0 & 0 \\ -4K & 6K & -4K & 1K & 0 & 0 & 0 & 0 & 0 & 0 & 0 & 0 \\ 1K & -4K & 6K & -4K & 1K & 0 & 0 & 0 & 0 & 0 & 0 & 0 \\ 0 & 1K & -4K & 6K & -4K & 1K & 0 & 0 & 0 & 0 & 0 & 0 \\ 0 & 0 & 1K & -4K & 5K & -2K & 0 & 0 & 0 & 0 & 0 & 0 \\ 0 & 0 & 0 & 0 & 0 & 0 & 0 & 0 & 0 & 0 & 0 & 0 \end{bmatrix} \begin{bmatrix} u_1 \\ u_2 \\ u_3 \\ u_4 \\ u_5 \\ u_6 \\ u_7 \\ u_8 \\ u_9 \\ u_{10} \\ u_{11} \\ u_{12} \end{bmatrix} - \frac{hF_H\Delta x^2}{2EI} \begin{bmatrix} 0 \\ 0 \\ 0 \\ 0 \\ 1 \\ 0 \\ 0 \\ 0 \\ 0 \\ 0 \\ 0 \\ 0 \end{bmatrix} \quad (\text{B.16})$$

Where $K = -\frac{EI}{\rho A \Delta x^4}$.

The same procedure can be done for the remaining terms in the full equation of motion of the beam, resulting in an extensive matrix representation that can be solved by MATLAB.

Complete matrix as implemented in MATLAB

When the remaining terms are included in the discretisation, the complete equation of motion can be expressed in a matrix equation as in Eq.B.17. Note that this is the full matrix for $n = 6$ elements. In this research, a beam of length $L = 1000$ [m] is considered with 1000 free nodes.

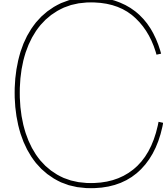
$$\begin{bmatrix} \ddot{u}_1 \\ \ddot{u}_2 \\ \ddot{u}_3 \\ \ddot{u}_4 \\ \ddot{u}_5 \\ \ddot{u}_6 \\ \ddot{u}_1 \\ \ddot{u}_2 \\ \ddot{u}_3 \\ \ddot{u}_4 \\ \ddot{u}_5 \\ \ddot{u}_6 \end{bmatrix} = \begin{bmatrix} 0 & 0 & 0 & 0 & 0 & 0 & 1 & 0 & 0 & 0 & 0 & 0 \\ 0 & 0 & 0 & 0 & 0 & 0 & 0 & 1 & 0 & 0 & 0 & 0 \\ 0 & 0 & 0 & 0 & 0 & 0 & 0 & 0 & 1 & 0 & 0 & 0 \\ 0 & 0 & 0 & 0 & 0 & 0 & 0 & 0 & 0 & 1 & 0 & 0 \\ 0 & 0 & 0 & 0 & 0 & 0 & 0 & 0 & 0 & 0 & 1 & 0 \\ 0 & 0 & 0 & 0 & 0 & 0 & 0 & 0 & 0 & 0 & 0 & 1 \\ K_{11} & K_{12} & K_{13} & 0 & 0 & 0 & C_{11} & C_{12} & 0 & 0 & 0 & 0 \\ K_{21} & K_{22} & K_{23} & K_{24} & 0 & 0 & C_{21} & C_{22} & C_{23} & 0 & 0 & 0 \\ K_{31} & K_{32} & K_{33} & K_{34} & K_{35} & 0 & 0 & C_{32} & C_{33} & C_{34} & 0 & 0 \\ 0 & K_{42} & K_{43} & K_{44} & K_{45} & K_{46} & 0 & 0 & C_{43} & C_{44} & C_{45} & 0 \\ 0 & 0 & K_{53} & K_{54} & K_{55} & K_{56} & 0 & 0 & 0 & C_{54} & C_{55} & C_{56} \\ 0 & 0 & 0 & 0 & 0 & 0 & 0 & 0 & 0 & 0 & 0 & 0 \end{bmatrix} \begin{bmatrix} u_1 \\ u_2 \\ u_3 \\ u_4 \\ u_5 \\ u_6 \\ u_7 \\ u_8 \\ u_9 \\ u_{10} \\ u_{11} \\ u_{12} \end{bmatrix} + \begin{bmatrix} 0 \\ 0 \\ 0 \\ 0 \\ F_5 \\ 0 \\ 0 \\ 0 \\ 0 \\ 0 \\ 0 \\ 0 \end{bmatrix} \quad (\text{B.17})$$

Where:

$$\begin{aligned}
 K_{11} &= 7K1 + K3 - 2K5 - 2K2N - K4N & C_{11} &= -2C1N \\
 K_{21} &= K5 - 4K1 + K2N + 2K4N & C_{21} &= C2 + C1N \\
 K_{31} &= K1 - K4N & C_{12} &= C1N - C2 \\
 K_{12} &= K5 - 4K1 + K2N - 2K4N & C_{22} &= -2C1N \\
 K_{22} &= 6K1 + K3 - 2K5 - 2K2N & C_{32} &= C2 + C1N \\
 K_{32} &= K5 - 4K1 + K2N + 2K4N & C_{23} &= C1N - C2 \\
 K_{42} &= K1 - K4N & C_{33} &= -2C1N \\
 K_{13} &= K1 + K4N & C_{43} &= C2 + C1N \\
 K_{23} &= K5 - 4K1 + K2N - 2K4N & C_{34} &= C1N - C2 \\
 K_{33} &= 6K1 + K3 - 2K5 - 2K2N & C_{44} &= -2C1N \\
 K_{43} &= K5 - 4K1 + K2N + 2K4N & C_{54} &= C2 + C1N \\
 K_{53} &= K1 - K4N & C_{45} &= C1N - C2 \\
 K_{24} &= K1 + K4N & C_{55} &= -2C1N \\
 K_{34} &= K5 - 4K1 + K2N - 2K4N & C_{56} &= C1N - C2 \\
 K_{44} &= 6K1 + K3 - 2K5 - 2K2N & F_5 &= -\frac{N}{2\rho\Delta x^2} + \frac{N^2 cv_x}{4EI\Delta x} \\
 K_{54} &= K5 - 4K1 + K2N + 2K4N \\
 K_{35} &= K1 + K4N \\
 K_{45} &= K5 - 4K1 + K2N - 2K4N \\
 K_{55} &= 5K1 + K3 - 2K5 - 2K2N - K4N \\
 K_{46} &= K1 + K4N \\
 K_{56} &= K5 - 2K1 + K2N
 \end{aligned}$$

Where:

$$\begin{aligned}
 K1 &= -\frac{EI}{\rho A \Delta x^4} & K5 &= -\frac{v_x^2}{\Delta x^2} \\
 K2 &= -\frac{N}{\rho A \Delta x^2} & C1 &= \frac{Nc}{\rho A \Delta x^2} \\
 K3 &= -\frac{\rho v_x g}{\rho A} & C2 &= -\frac{v_x}{\Delta x} \\
 K4 &= \frac{Ncv_x}{2\rho A \Delta x^3}
 \end{aligned}$$



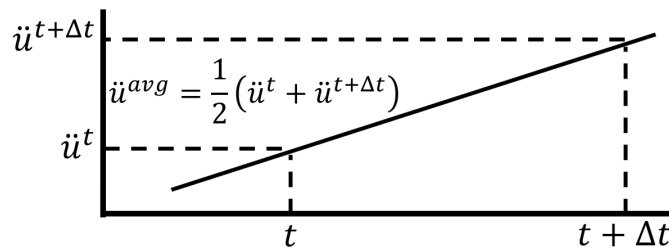
Newmark method

The Newmark method is one of the most widely used time integration algorithms for structural analysis. This is because the method is easy to use, second order accurate and unconditionally stable assuming average constant acceleration (Nickel, 1971). The concept of average constant acceleration and the procedure of the method is discussed hereafter. Consider the set of equations of motion that needs to be solved:

$$M\ddot{u} + C\dot{u} + Ku = f(t) \quad (C.1)$$

At time t , the values for u , \dot{u} and \ddot{u} are known, also referred to as initial conditions. The objective is to obtain the solution at a time $t + \Delta t$ in the future, where Δt is the time increment, resulting in the following system:

$$\begin{cases} M\ddot{u}^{t+\Delta t} + C\dot{u}^{t+\Delta t} + Ku^{t+\Delta t} = f^{t+\Delta t} \\ u(t) = u^t, \quad \dot{u}(t) = \dot{u}^t \end{cases} \quad (C.2)$$



When one assumes the acceleration to be changing linearly between t and $t + \Delta t$, as illustrated in the figure above, the average acceleration \ddot{u}^{avg} can be expressed as:

$$\ddot{u}^{avg} = \frac{1}{2} (\ddot{u}^t + \ddot{u}^{t+\Delta t}) \quad (C.3)$$

The velocity and displacement at $t + \Delta t$ can then be approximated by:

$$\begin{aligned} \dot{u}^{t+\Delta t} &= \dot{u}^t + \ddot{u}^{avg} \Delta t = \dot{u}^t + \frac{1}{2} \Delta t (\ddot{u}^t + \ddot{u}^{t+\Delta t}) \\ u^{t+\Delta t} &= u^t + \dot{u}^t \Delta t + \frac{1}{2} \ddot{u}^{avg} \Delta t^2 = u^t + \dot{u}^t \Delta t + \frac{1}{4} \Delta t^2 (\ddot{u}^t + \ddot{u}^{t+\Delta t}) \end{aligned} \quad (C.4)$$

Both expressions in Eq.C.4 can be split into parts depending on known time step values (t) and on unknown time step values ($t + \Delta t$). Accordingly, predictors and correctors can be constructed, where the predictors depend on the values at t and the correctors determine the solution at $t + \Delta t$.

Predictors:

$$\begin{cases} \tilde{u}^{t+\Delta t} = \dot{u}^t + \frac{1}{2} \Delta t \ddot{u}^t \\ \tilde{u}^{t+\Delta t} = u^t + \dot{u}^t \Delta t + \frac{1}{4} \Delta t^2 \ddot{u}^t \end{cases} \quad (C.5)$$

Correctors:

$$\begin{cases} \dot{u}^{t+\Delta t} = \tilde{u}^{t+\Delta t} + \frac{1}{2} \Delta t \ddot{u}^{t+\Delta t} \\ u^{t+\Delta t} = \tilde{u}^{t+\Delta t} + \frac{1}{4} \Delta t^2 \ddot{u}^{t+\Delta t} \end{cases} \quad (C.6)$$

Now $\ddot{u}^{t+\Delta t}$ is still unknown, but can be found by rewriting the system of equations of motion from Eq.C.2 as:

$$\begin{aligned} M \ddot{u}^{t+\Delta t} + C \dot{u}^{t+\Delta t} + K u^{t+\Delta t} &= f^{t+\Delta t} \\ M \ddot{u}^{t+\Delta t} + C \left(\tilde{u}^{t+\Delta t} + \frac{1}{2} \Delta t \ddot{u}^{t+\Delta t} \right) + K \left(\tilde{u}^{t+\Delta t} + \frac{1}{4} \Delta t^2 \ddot{u}^{t+\Delta t} \right) &= f^{t+\Delta t} \\ M \ddot{u}^{t+\Delta t} + C \tilde{u}^{t+\Delta t} + C \left(\frac{1}{2} \Delta t \ddot{u}^{t+\Delta t} \right) + K \tilde{u}^{t+\Delta t} + K \left(\frac{1}{4} \Delta t^2 \ddot{u}^{t+\Delta t} \right) &= f^{t+\Delta t} \\ \ddot{u}^{t+\Delta t} \left(M + C \frac{1}{2} \Delta t + K \frac{1}{4} \Delta t^2 \right) &= f^{t+\Delta t} - C \tilde{u}^{t+\Delta t} - K \tilde{u}^{t+\Delta t} \\ \ddot{u}^{t+\Delta t} &= \left(M + C \frac{1}{2} \Delta t + K \frac{1}{4} \Delta t^2 \right)^{-1} \left(f^{t+\Delta t} - C \tilde{u}^{t+\Delta t} - K \tilde{u}^{t+\Delta t} \right) \end{aligned} \quad (C.7)$$

Thus, the system described by Eq.C.2 can be solved through:

- Step 1 Calculate predictors using known conditions with Eq.C.5
- Step 2 Solve linear problem to obtain unknown acceleration according to Eq.C.7
- Step 3 Calculate correctors to obtain solution at next time step with Eq.C.6

These steps have to be repeated for the full length of the simulation.

Bibliography

- 4C Offshore. (2021). Global offshore renewable map. <https://www.4coffshore.com/offshorewind/>
- Airy, G. B. (1845). *Tides and waves (from the encyclopedia metropolitana vol. 5)*. B. Fellowes.
- Barker, A., Timco, G., Gravesen, H., & Vølund, P. (2005). Ice loading on danish wind turbines: Part 1: Dynamic model tests. *Cold Regions Science and Technology*, *41*(1), 1–23. <https://doi.org/https://doi.org/10.1016/j.coldregions.2004.05.002>
- Brown, T. G., & Määttänen, M. (2009). Comparison of kemi-i and confederation bridge cone ice load measurement results. *Cold Regions Science and Technology*, *55*(1), 3–13. <https://doi.org/https://doi.org/10.1016/j.coldregions.2008.04.005>
- Chuang, Z., Li, C., Liu, S., & Lu, Y. (2020). Dynamic response of jacket-support offshore wind turbine under ice crushing load. *Proceedings of the International Conference on Offshore Mechanics and Arctic Engineering - OMAE*, *9*, 1–9. <https://doi.org/10.1115/omae2020-19340>
- Cordis. (2021). Measurements on structures in ice (strice). <https://cordis.europa.eu/project/id/EVG1-CT-2000-00024>
- Craig, R. R., & Bampton, M. C. C. (1968). Coupling of substructures for dynamic analyses. *AIAA Journal*, *6*(7), 1313–1319. <https://doi.org/10.2514/3.4741>
- Croasdale, K. R., & Metge, M. (1991). Structure geometry and ice interaction. In S. Jones, J. Tillotson, R. F. McKenna, & I. J. Jordaan (Eds.), *Ice-structure interaction* (pp. 641–668). Springer Berlin Heidelberg.
- Danys, J., & Bercha, F. (1976). Investigations of ice forces on a conical offshore structure. *Ocean Engineering*, *3*(5), 299–310. [https://doi.org/10.1016/0029-8018\(76\)90005-6](https://doi.org/10.1016/0029-8018(76)90005-6)
- De Klerk, D., Rixen, D. J., & Voormeeren, S. N. (2008). General framework for dynamic substructuring: History, review, and classification of techniques. *AIAA Journal*, *46*(5), 1169–1181. <https://doi.org/10.2514/1.33274>
- DNV.GL U.S. Department of Energy. (2014). Ice load project final technical report. (October), 1–109. https://nwtc.nrel.gov/system/files/DDRP0133-IceLoadFinalReport2014_10_30.pdf

- European Commission. (2019). The European Green Deal. *European Commission*, 53(9), 24. <https://doi.org/10.1017/CBO9781107415324.004>
- European Council. (2019). European Council meeting – Conclusions, EUCO 29/19. 12/12/2019, 9, 1–4. <https://www.consilium.europa.eu/media/41768/12-euco-final-conclusions-en.pdf>
- Frankenstein, G., & Garner, R. (1967). Equations for determining the brine volume of sea ice from -0.5 to -22.9°C . *J. Glaciology*, 6(48), 943–944.
- Goldstein, R., Onishchenko, D., Denisov, V., & Shatinsky, D. (2005). Refined bending failure model for the level ice acting on an inclined obstacle. *Proceedings of the International Conference on Port and Ocean Engineering under Arctic Conditions, POAC*, 199–212.
- Gravesen, H., Kärnä, T., Carlbro, G., Glostrup, & Denmark. (2009). Ice loads for offshore wind turbines in southern baltic sea.
- Gravesen, H., Sørensen, S. L., Vølund, P., Barker, A., & Timco, G. (2005). Ice loading on danish wind turbines: Part 2. analyses of dynamic model test results. *Cold Regions Science and Technology*, 41(1), 25–47. <https://doi.org/https://doi.org/10.1016/j.coldregions.2004.05.009>
- Gruber, F. M., Gille, M., & Rixen, D. J. (2017). Time integration of dual craig-bampton reduced systems. *COMPADYN 2017 - Proceedings of the 6th International Conference on Computational Methods in Structural Dynamics and Earthquake Engineering*, 1, 1135–1154. <https://doi.org/10.7712/120117.5481.17213>
- Guyan, R. J. (1965). Reduction of stiffness and mass matrices. *AIAA Journal*, 3(2), 380–380. <https://doi.org/10.2514/3.2874>
- Hasegawa, K., Uto, S., Shimoda, H., Wako, D., & Matsuzawa, T. (2019). Non-smooth dem simulation for interaction of conical structure and managed ice floes using breakable ice element. *Proceedings of the International Conference on Port and Ocean Engineering under Arctic Conditions, POAC, 2019-June*.
- Hendrikse, H., Ziemer, G., & Owen, C. C. (2018). Experimental validation of a model for prediction of dynamic ice-structure interaction. *Cold Regions Science and Technology*, 151, 345–358. <https://doi.org/10.1016/j.coldregions.2018.04.003>
- Hendrikse, H. (2017). *Ice-induced vibrations of vertically sided offshore structures* (Doctoral dissertation). <https://doi.org/https://doi.org/10.4233/uuid:325ebcfb-f920-400c-8ef6-21b2305b6920>
- Hendrikse, H., & Koot, J. (2019). Consideration of ice drift in determining the contribution of ice-induced vibrations to structural fatigue. *2019-June*. <https://www.poac2019.nl>
- Hendrikse, H., & Metrikine, A. (2016). Ice-induced vibrations and ice buckling. *Cold Regions Science and Technology*, 131, 129–141. <https://doi.org/10.1016/j.coldregions.2016.09.009>

- Hendrikse, H., & Nord, T. S. (2019). Dynamic response of an offshore structure interacting with an ice floe failing in crushing. *Marine Structures*, 65, 271–290.
- Hibbeler, R. (2013). *Mechanics of materials*, ninth edition. Pearson Education.
- Huang, Y., Shi, Q., & Song, A. (2007). Model test study of the shielding effect of multi-pile structures on ice force. *Proceedings of the International Conference on Port and Ocean Engineering under Arctic Conditions, POAC*, 18, 190–202.
- IEC 61400-3-1. (2019a). *Wind energy generation systems – Part 3-1: Design requirements for fixed offshore wind turbines* (Standard). International Electrotechnical Commission. Geneva, CH.
- IEC 61400-3-1. (2019b). *Wind energy generation systems – Part 3-1: Design requirements for fixed offshore wind turbines* (Standard) [D.4.4.3]. International Electrotechnical Commission. Geneva, CH.
- ISO 19902. (2007). *Petroleum and natural gas industries – Fixed steel offshore structures* (Standard). International Organization for Standardization. Geneva, CH.
- ISO 19906. (2019). *Petroleum and natural gas industries – Arctic offshore structures* (Standard). International Organization for Standardization. Geneva, CH.
- Ji, X., & Oterkus, E. (2016). A dynamic ice-structure interaction model for ice-induced vibrations by using van der pol equation. *Ocean Engineering*, 128, 147–152. <https://doi.org/10.1016/j.oceaneng.2016.10.028>
- Jonkman, J., Butterfield, S., Musial, W., & Scott, G. (2009). *Definition of a 5-MW reference wind turbine for offshore system development* (Tech. report). National Renewable Energy Laboratory. Golden, Colorado, US. <http://www.osti.gov/bridge>
- Kärnä, T., & Jochmann, P. (2003). Field observations on ice failure modes. *Proc. 17th International Conference on Port and Ocean Engineering under Arctic Conditions (POAC'03)*, 2.
- Kato, K. (1990). Total ice force on multi-legged structures. *IAHR Symposium on Ice*, 974–983.
- Keijdener, C., Hendrikse, H., & Metrikine, A. (2019). An effective fluid model for the bending failure of level ice. *POAC 2019 - 25th International Conference on Port and Ocean Engineering under Arctic Conditions, 2019-June*. <https://www.poac2019.nl>
- Leppäranta, M., & Lewis, J. (2007). Observations of ice surface temperature and thickness in the baltic sea. *International Journal of Remote Sensing*, 28(17), 3963–3977. <https://doi.org/10.1080/01431160601075616>
- Leppäranta, M. (1981). An ice drift model for the baltic sea. *Tellus*, 33(6), 583–593. <https://doi.org/10.3402/tellusa.v33i6.10778>

- Li, Z., Dong, J.-W., Lu, Z.-Q., Chen, J.-F., & Li, G.-W. (2009). Physical experiments and simulation of sea ice force on pile structures in ports. *Gongcheng Lixue/Engineering Mechanics*, *26*, 212–217.
- Lindgren, E., Tuomi, L., & Huess, V. (2020). Baltic sea production centre (cmems), 1–28. <https://catalogue.marine.copernicus.eu/documents/QUID/CMEMS-BAL-QUID-003-015.pdf>
- Määttänen, M. P. (1991). Ice interaction with structures. In S. Jones, J. Tillotson, R. F. McKenna, & I. J. Jordaan (Eds.), *Ice-structure interaction* (pp. 563–579). Springer Berlin Heidelberg.
- Marsman, I. (2018). Ice-induced vibrations of wind turbines with a jacket support structure. <http://resolver.tudelft.nl/uuid:b2221fa3-32b8-4f0e-b663-ee906492e87e>
- Metrikine, A. V. (2006). Dynamics, Slender Structures and an Introduction to Continuum Mechanics, Faculty of Civil Engineering and Geosciences, Delft University of Technology.
- Metrikine, A. V. (2020). Structural dynamics, Lecture 8, Faculty of Civil Engineering and Geosciences, Delft University of Technology.
- Newmark, N. M. (1959). A method of computation for structural dynamics. *Journal of the Engineering Mechanics Division*, *85*(3), 67–94. <https://doi.org/10.1061/JMCEA3.0000098>
- Nickel, R. E. (1971). On the stability of approximation operators in problems of structural dynamics. *International Journal of Solids and Structures*, *7*(3), 301–319. [https://doi.org/10.1016/0020-7683\(71\)90028-X](https://doi.org/10.1016/0020-7683(71)90028-X)
- Ralston, T. D. (1980). Plastic limit analysis of sheet ice loads on conical structures. In P. Tryde (Ed.), *Physics and mechanics of ice* (pp. 289–308). Springer Berlin Heidelberg.
- Ralston, T. D. (1977). Ice force design considerations for conical offshore structures.
- Ranta, J., & Polojärvi, A. (2019). Limit mechanisms for ice loads on inclined structures: Local crushing. *Marine Structures*, *67*, 102633. <https://doi.org/https://doi.org/10.1016/j.marstruc.2019.102633>
- Reuters. (2021). Green energy investors target poland as it weans itself off coal. <https://www.reuters.com/article/us-poland-energy-offshore-idUSKBN2AA1I6>
- Sambu Potty, N., & Ahmad Sohaimi, A. F. (2013). Ultimate Strength Assessment for Fixed Steel Offshore Platform. *Malaysian Journal of Civil Engineering*, *25*(2), 128–153. <https://doi.org/10.11113/mjce.v25n2.298>
- Shi, Q., Huang, Y., Song, A., & Tong, J. (2002). Non-simultaneous failure of ice in front of multi-leg structures. *China Ocean Engineering*, *16*(4), 437–443.

- Sliggers, P. (2019). Bottom founded offshore structures, Lecture Environmental Loading, Faculty of Civil Engineering and Geosciences, Delft University of Technology.
- Sodhi, D., & Haehnel, R. (2003). Crushing ice forces on structures. *Journal of Cold Regions Engineering*, 17. [https://doi.org/10.1061/\(ASCE\)0887-381X\(2003\)17:4\(153\)](https://doi.org/10.1061/(ASCE)0887-381X(2003)17:4(153))
- Spijkers, J., Vrouwenfelder, A., & Klaver, E. (2005). Structural Dynamics CT 4140. *Lecture notes*, 1–204.
- Tang, Y., Shi, W., You, J., & Michailides, C. (2020). Effects of nonlinear wave loads on large monopile offshore wind turbines with and without ice-breaking cone configuration. *Journal of Marine Science and Technology*, 26. <https://doi.org/10.1007/s00773-020-00719-4>
- Timco, G., & Frederking, R. (1990). Compressive strength of sea ice sheets. *Cold Regions Science and Technology*, 17, 227–240.
- Timco, G., Irani, M., Tseng, J., Liu, L., & Zheng, C. (1992). Model tests of dynamic ice loading on the Chinese JZ-20-2 jacket platform. *Canadian Journal of Civil Engineering*.
- Timco, G., & O'Brien, S. (1994). Flexural strength equation for sea ice. *Cold Regions Science and Technology*, 22(3), 285–298. [https://doi.org/10.1016/0165-232X\(94\)90006-X](https://doi.org/10.1016/0165-232X(94)90006-X)
- Timco, G., & Weeks, W. (2010). A review of the engineering properties of sea ice. *Cold Regions Science and Technology*, 60(2), 107–129. <https://doi.org/https://doi.org/10.1016/j.coldregions.2009.10.003>
- United Nations. (2015). Paris agreement.
- Van der Valk, P. (2014a). Coupled Simulations of Wind Turbines and Offshore Support Structures: Strategies based on the Dynamic Substructuring Paradigm. https://www.researchgate.net/publication/275213625_Coupled_Simulations_of_Wind_Turbines_and_Offshore_Support_Structures_Strategies_based_on_the_Dynamic_Substructuring_Paradigm
- Van der Valk, P. (2014b). Coupled Simulations of Wind Turbines and Offshore Support Structures: Strategies based on the Dynamic Substructuring Paradigm, 99–116. https://www.researchgate.net/publication/275213625_Coupled_Simulations_of_Wind_Turbines_and_Offshore_Support_Structures_Strategies_based_on_the_Dynamic_Substructuring_Paradigm
- Voormeeren, S. N., Van Der Valk, P. L., & Rixen, D. J. (2011). Generalized methodology for assembly and reduction of component models for dynamic substructuring. *AIAA Journal*, 49(5), 1010–1020. <https://doi.org/10.2514/1.J050724>
- Voormeeren, S., van der Valk, P., Nortier, B., Molenaar, D.-P., & Rixen, D. (2014). Accurate and efficient modeling of complex offshore wind turbine support structures using augmented superelements. *Wind Energy*, 17(7), 1035–1054.

- Vorpahl, F., Popko, W., & Kaufer, D. (2013). *Description of a basic model of the 'UpWind reference jacket' for code comparison in the OC4 project under IEA Wind Annex 30* (Tech. report).
- Vugts, J. (2013). *Handbook of bottom founded offshore structures: Part 1. general features of offshore structures and theoretical background*. Eburon. <https://books.google.nl/books?id=5UXqDQAAQBAJ>
- Weertman, J. (1983). Creep deformation of ice. *Annual Review of Earth and Planetary Sciences*, 11(1), 215–240. <https://doi.org/10.1146/annurev.ea.11.050183.001243>
- Wille, S., Kuiper, G., & Metrikine, A. (2011). On the dynamic interaction between drifting level ice and moored downward conical structures: A critical assessment of the applicability of a beam model for the ice. <https://doi.org/10.1115/OMAE2011-50120>
- Willems, T. (2016). Coupled modeling of dynamic ice-structure interaction on offshore wind turbines, 1–168. <https://repository.tudelft.nl/islandora/object/uuid%5C%3Aaccfb7cd2-f8ca-4380-ad03-3b9dcc78f0b3>
- Willems, T., & Hendrikse, H. (2019). Coupled simulation of ice-structure interaction of offshore wind turbines in bhawc using vanilla. *Proceedings of the International Conference on Port and Ocean Engineering under Arctic Conditions, POAC, 2019-June*.
- Wind Europe. (2021a). Wind energy today. <https://windeurope.org/about-wind/wind-energy-today/>
- Wind Europe. (2021b). Wind energy today. <https://windeurope.org/newsroom/significant-developments-on-offshore-wind-in-the-baltic-sea/>
- WindEurope. (2021c). Offshore wind in Europe - Key trends and statistics 2020. *WindEurope*, 3(2), 14–17.
- Xu, N., Yue, Q., Bi, X., Tuomo, K., & Zhang, D. (2015). Experimental study of dynamic conical ice force. *Cold Regions Science and Technology*, 120, 21–29. <https://doi.org/https://doi.org/10.1016/j.coldregions.2015.08.010>
- Yue, Q., & Bi, X. (2000). Ice-induced jacket structure vibrations in bohai sea. *Journal of Cold Regions Engineering*, 14. [https://doi.org/10.1061/\(ASCE\)0887-381X\(2000\)14:2\(81\)](https://doi.org/10.1061/(ASCE)0887-381X(2000)14:2(81))
- Zhang, L., Li, Z., Wang, Y., Li, G., & Han, M. (2005). Model tests of ice forces on conical structures for a harbor design in bohai. *Proceedings of the International Conference on Port and Ocean Engineering under Arctic Conditions, POAC, 1*, 463–470.
- Żuk, P., & Żuk, P. (2021). Increasing energy prices as a stimulus for entrepreneurship in renewable energies: Ownership structure, company size and energy policy in companies in Poland. *Energies*, 14(18). <https://doi.org/10.3390/en14185885>

